2016

Internal Degrees of Freedom and Spin Transitions in Single Molecule Magnets

James Atkinson
University of Central Florida

INTERNAL DEGREES OF FREEDOM AND SPIN TRANSITIONS IN SINGLE MOLECULE MAGNETS

by

JAMES HUNTER ATKINSON
MS University of Central Florida, 2012
BA Hampshire College, 2006

A dissertation submitted in partial fulfillment of the requirements
for the degree of Doctor of Philosophy in Physics
in the Department of Physics
in the College of Sciences
at the University of Central Florida
Orlando, Florida

Spring Term
2016

Major Professor: Enrique del Barco

ABSTRACT

This thesis covers a range of work detailing the transitions between spin eigenstates in molecular magnet systems. Broadly speaking, these transitions can be divided into two kinds: Those that involve a the tunneling of spin through a potential barrier to a resonant state on the other side, a phenomenon known as quantum tunneling of magnetization, and those that occur through the absorption or emission of a photon. In this latter case, the energy of the photon must match the difference between two eigenstates with a difference in angular momentum of $\hbar$.

We will detail research performed on single molecule magnets, a class of systems that has established itself as an exemplar of higher-order spin interaction. Specifically, we will present the results of studies focused on two Manganese based systems, both of which represent good examples of single molecule magnet behavior. By performing magnetization measurements below the temperature threshold where these systems' polarizations become hysteretic, we find that the precise form of the observed resonant tunneling features (which includes evidence for strong interference of geometric phase a.k.a. Berry phase) can be related to the specifics of the intramolecular interaction. We have analyzed our results using the "giant spin" model (which approximates the system as a single spin) as well as with a "multi-spin" method which considers all interactions between the ions in the molecular core.

We will also discuss the results of measurements performed on a crystalline sample under stress (uniaxial pressure). The data has been analyzed in a framework in which a physical distortion is modelled as a modification of the molecular anisotropy, with different directions of applied stress represented as changes to different parameters governing the molecular energy landscape. This analysis includes simulation of the magnetic relaxation through a master equation approach to the spin-phonon interaction.

Finally, our discussion will outline efforts toward understanding the coherent behavior of spin systems. The "weak" and "strong" coupling between a photon and spin represent two regimes of an

interaction by which the information within a spin can be accessed and manipulated. We will discuss the challenges involved in exploring these regimes, both from a theoretical and experimental standpoint. The purpose of this experiment dovetails with those outlined above in attempting to form an intimate basis of knowledge describing the universal relationships to spin at the most fundamental level.

This thesis is dedicated to my wife, to my family, and to all the other teachers who helped me reach here.

ACKNOWLEDGMENTS

I would like to acknowledge the gracious support and encouragement of my advisor, Dr. Enrique del Barco, as well as my committee members Dr. Bo Chen, Dr. Fernando Luis, and Dr. Eduardo Mucciolo. I'd also like to thank all of my collaborators, in particular Dr. Jonathan Friedman of Amherst College and Dr. Stephen Hill at the NHMFL in Tallahassee.

I would also like to thank the UCF Physics department for their support, in particular Dr. Elena Flitsiyan, and the National Science Foundation for their support. I also owe a debt of gratitude to my current and former group members, including Dr. Firoze Haque, Dr. Asma Amjad, Dr. Simran Singh, Dr. Alvar Rodriguez, Marta Anguera, Priyanka Vaidya, Rebecca Cebulka, Tyler Townsend, Chris Coleman, and, most of all, Dr. Hajrah Quddusi. Finally, I'd like to thank my parents, without whom none of this would be possible, and my siblings David and Sara, who contributed in innumerable ways.

TABLE OF CONTENTS

LIST OF FIGURES

LIST OF TABLES

LIST OF ABBREVIATIONS

BPI	Berry phase interference
EPR	Electron paramagnetic resonance
GS	Giant-spin (Hamiltonian/model)
JC	Jayne-Cummings (Hamiltonian/model)
JT	Jahn-Teller (axis)
LZ	Landau-Zener
MS	Multi-spin (Hamiltonian/model)
QTM	Quantum tunneling of magnetization
SMM	Single molecule magnet

CHAPTER 1: INTRODUCTION

Two ceramic bar magnets are all you need to explore a realm that normally lies beyond the scope of human experience. The way that different orientations can lead to attractive or repulsive forces is fascinating but perhaps difficult to intuit. Until the scientific endeavors of the 19th century (by Oersted, Faraday, Maxwell, Ampere, etc.), the rare magnetic object (such as a "lodestone" or a magnetic compass) could only hint at the existence of mechanisms fundamentally different from what we need to interpret the greater part of the world around us. With the arrival of modern science, their understanding changed rapidly and the utility of electricity and magnetism was incorporated into the heart of the industrial revolution. By the middle of the 20th century, the theory of electromagnetic phenomenon had been unified and placed firmly within the framework of quantum mechanics in which the source of macroscopic magnetism was traced to either electric currents or to the intrinsic angular momentum of fundamental particles, the property known as *spin*.

The discoveries of the relationship between moving *electric* charge and *magnetic* force and of the existence of angular momentum in the absence of tangible physical rotation are two of the most startling discoveries in the history of science. From there, one only need consider their combination within a charged particle to understand the atomic building blocks of permanent magnets. More broadly, we find that many things which appear non-magnetic are actually composed of magnetic materials or are fundamentally susceptible to magnetic fields. The lesson here is that magnetic systems are pervasive and essential, if seemingly abstract.

In this thesis, we will explore the behavior of spins through the study of Single Molecule Magnets (SMMs). These are molecular systems that typically exhibit large spins (often times > 10$\hbar$) and intrinsic anisotropy, leading to slow relaxation of spin at low temperatures. They also often display the phenomenon known as quantum tunneling of magnetization (QTM), a non-classical process by which the molecular spin can tunnel through the anisotropy energy barrier. We study these systems in order to learn

about the intra-molecular interactions, including couplings between ions in the magnetic core and the bonds they form with non-magnetic neighbors, which can teach us about the behavior of spin in different energy landscapes.

The remainder of this chapter will include a brief background of the fundamentals theoretical elements useful in analysis of SMMs. This background will begin with the case of the spin ½ electron, serving as an introduction to the quantum mechanical framework necessary to describe the interaction of a spin with a magnetic field and individual photons. The subsequent section will further detail SMM systems, including some of the theoretical underpinnings behind the explanation of QTM.

1.1 Spin ½

In the theory of quantum mechanics, the state of a system is described by the coefficients of eigenstates as determined from the equations of motion, while observable properties manifest as eigenvalues/eigenstates of a Hermitian operator acting on the state wavefunction. Essentially, this implies that we can only extract information about a system as some amplitude (the eigenvalue) of some state (an eigenstate of the observable operator), while the system itself is described with another set of eigenvalues/eigenstates of another operator (such as a Hamiltonian). Thus, classical properties are rooted in operators which extract (incomplete) information from the system state (the wavefunction).

1.1.1 The Classical Magnetic Dipole Potential

Take angular momentum for example: The famous Stern-Gerlach experiment demonstrated quantization of spin angular momentum through the effect of a magnetic field on a moving ion, sorting a randomly oriented stream into two populations of strictly parallel/antiparallel magnetic moments. We can perform the transit from the classical to quantum regimes by beginning with the classical expression for the potential U_B of a magnetic moment $\boldsymbol{\mu}$ in a magnetic field $\boldsymbol{B}$:

$$U_B = -\boldsymbol{\mu} \cdot \boldsymbol{B}. \tag{1.1}$$

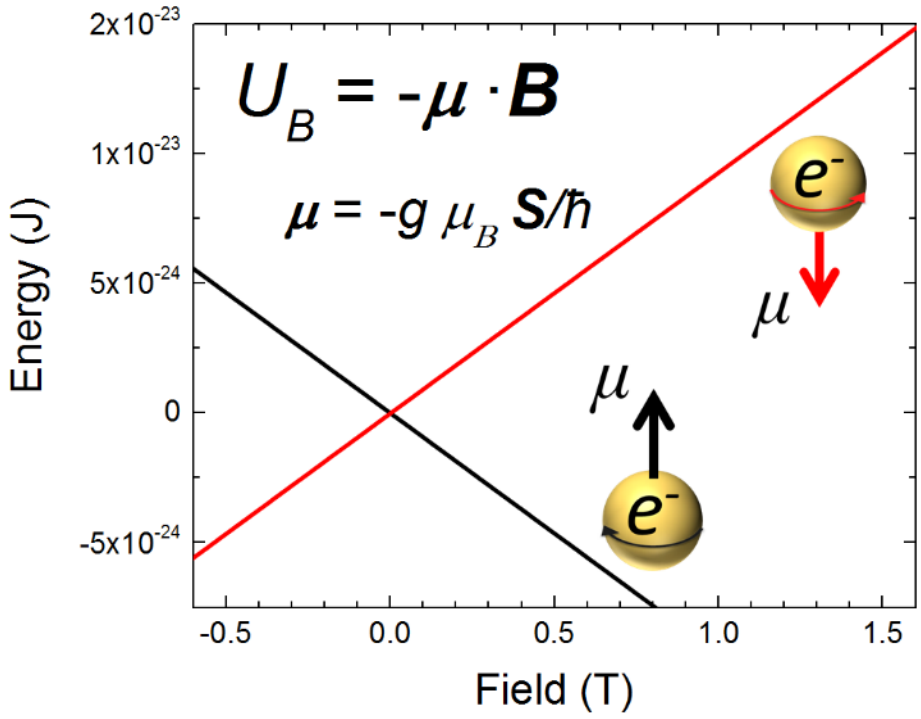

Figure 1.1 - Plot of the energies of the parallel/antiparallel orientations of an electron spin in a magnetic field. The yellow spheres with arrows represent electrons and their magnetic moments. Note that these arrows reflect a "left hand" rule due to the negative charge of the electron, with the curved arrows representing a hypothetical classical physical rotation which produces the equivalent direction of spin.

The semi-quantum expression relating the magnetic moment to spin is given by

$$\boldsymbol{\mu} = -g\mu_B \boldsymbol{S}/\hbar \tag{1.2}$$

where $g \approx 2$ (for a free electron spin) is the dimensionless g-factor and μ_B is the Bohr magneton. Since the moment of a free electron will always prefer to point along the direction of an applied field, we can substitute the dot product with the scalar product $S_z B$. Figure 1.1 shows a plot of the energies of the two orientations of an electron in an applied field as defined by equation (1.1) with the yellow spheres representing the electrons as a kind of classically equivalent spinning-ball. The lines represent the parallel/antiparallel orientations of the moment with respect to the applied field, states that maximize/minimize the energy.

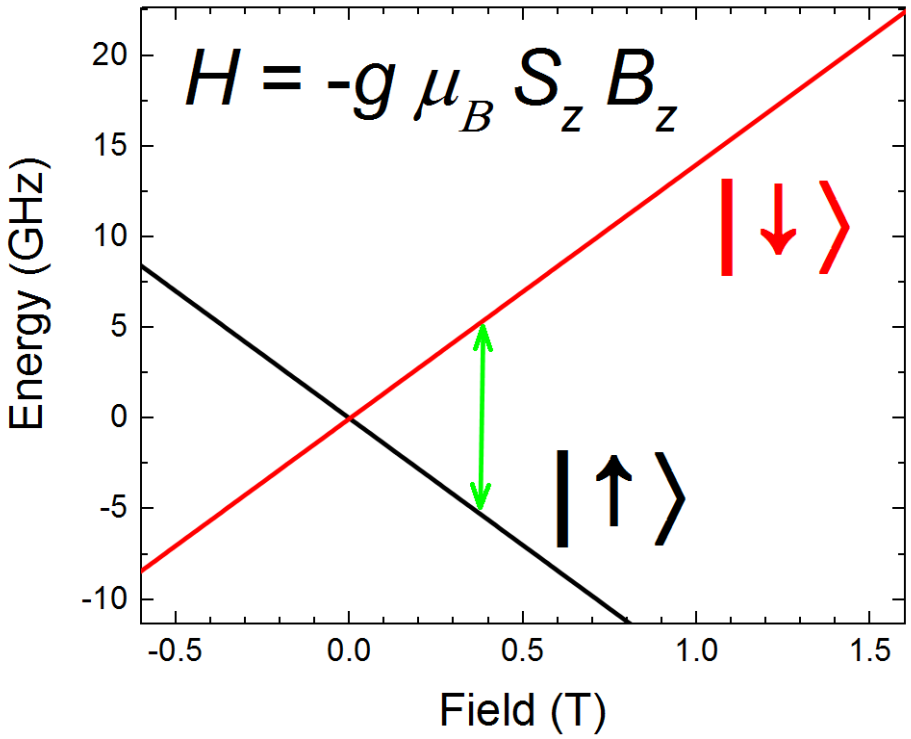

Figure 1.2 – Energy level diagram of the eigenstates of equation 1.4. The green arrow represents an energy separation of 10 GHz between the two states.

1.1.2 The Zeeman Interaction

Our first step towards the quantum regime begins by admitting the quantization of spin. Presumably, *B* is large (on the scale of 1 T) and can be approximated as a continuous variable, but the spin of an electron is a universally minute quantity that falls squarely within the discrete quantum regime. This is the level where the Stern-Gerlach experiment revealed the discretization in units of Planck's constant $\hbar$, a feature incorporated within the operator representing the observable S_Z (as the "projection" of the spin into the quantization axis, defined in this case by the direction of application of *B*):

$$S_z \equiv \frac{\hbar}{2}\begin{bmatrix}1 & 0\\ 0 & -1\end{bmatrix}. \tag{1.3}$$

The eigenvectors of this matrix are [1, 0] and [0, 1], with eigenvalues +1 and -1, respectively. Quantum mechanics tells us that we can only ever find the electron in an eigenstate of the observable, so we are left to conclude that every measurement of the electron's spin along a direction *Z* will indicate a spin of either

$+\hbar/2$ or $-\hbar/2$, regardless of whether an applied field is pointing along that direction or not. Changing the field will only affect the average (the expectation value) of all of the measurements. We can further replace the classical potential U_B with a Hamiltonian consisting of the Zeeman coupling

$$H = -g\mu_B S_z B_z \tag{1.4}$$

where B_z is the component of the field that lies along the direction of the particle's spin vector $\boldsymbol{S}$ (this may seem a trivial distinction, since the orientation of an electron's moment in a field will always point along that direction, but we introduce it here to lay the groundwork for systems with arbitrary intrinsic fields). Note that a minus sign has effectively been incorporated into S_z (and an $\hbar$ has disappeared) as compared to equations (1.1) and (1.2) so that the ground state occurs when S_z and B_z have the same sign. We can label our eigenstates with the kets $|\uparrow\rangle$ and $|\downarrow\rangle$, representing "spin up" and "spin down", respectively. Figure 1.2 shows a plot of the eigenvalues of the two states defined by equation (1.4) in units of gigahertz.

1.1.3 The Transition Matrix Element

With formalized eigenstates we can lay the groundwork for transitions between different spin levels. The general form for the intensity of an associated transition is given by Hamiltonian matrix element

$$M = \langle\uparrow|H|\downarrow\rangle\,. \tag{1.5}$$

As written, equation (1.5) contains no off-diagonal elements which might mix the system's eigenstates. However, if we can include some dependence upon the spin's projection into the transverse XY plane, we would find a non-zero transition probability through the x, y spin ½ operators

$$S_x \equiv \frac{\hbar}{2}\begin{bmatrix}0 & 1\\ 1 & 0\end{bmatrix} \tag{1.6}$$

$$S_y \equiv \frac{\hbar}{2i}\begin{bmatrix}0 & -1\\ 1 & 0\end{bmatrix} \tag{1.7}$$

which are related to the Pauli spin operators $\boldsymbol{\sigma}_x$ $\boldsymbol{\sigma}_y$ $\boldsymbol{\sigma}_z$ by $S_i = \hbar\, \boldsymbol{\sigma}_i/2$. This is the fundamental principle behind electron paramagnetic resonance (EPR) spectroscopy, in which a transition occurs through the off-diagonal element in a Hamiltonian induced by the field of a cavity excitation, i.e. the coupling between the spin and a photon. Generally, we can define the transition rate through Fermi's golden rule equation

$$\Gamma = \frac{2\pi}{\hbar}|M|^2\delta[E_p - E_\Delta] \tag{1.8}$$

where E_p is the energy of the photon, E_Δ is the energy difference between the two levels in the transition, and δ is the delta function. This equation implies the transition probability is zero everywhere except where the photon energy precisely matches the transition energy. In practice, many factors will lead to a broadening of observed spectral lines [1,2], such that the delta function can effectively be replaced with a "linewidth" function such as a Lorentzian or Gaussian. The other restriction for an EPR transition is that the change in the system's spin must match that of the absorbed/emitted photon, i.e. that $\Delta S = \pm 1$, such that total spin is conserved.

As we will see in the next section, systems with larger spin than ½ require additional machinery to understand. In general, the relevant spin matrices for arbitrarily large spins are given by [3]

$$\langle m_a|S_z|m_b\rangle = \delta[m_a - m_b]m_b \tag{1.9}$$

$$\langle m_a|S_x|m_b\rangle = \frac{1}{2}(\delta[m_a - m_b + 1] + \delta[m_a - m_b - 1])\sqrt{S(S+1) - m_a m_b} \tag{1.10}$$

$$\langle m_a|S_y|m_b\rangle = \frac{i}{2}(\delta[m_a - m_b + 1] - \delta[m_a - m_b - 1])\sqrt{S(S+1) - m_a m_b} \tag{1.11}$$

In addition to the complexities of larger spin, the following discussion will introduce intrinsic anisotropy, as well as a new mode of transition which that phenomenon creates.

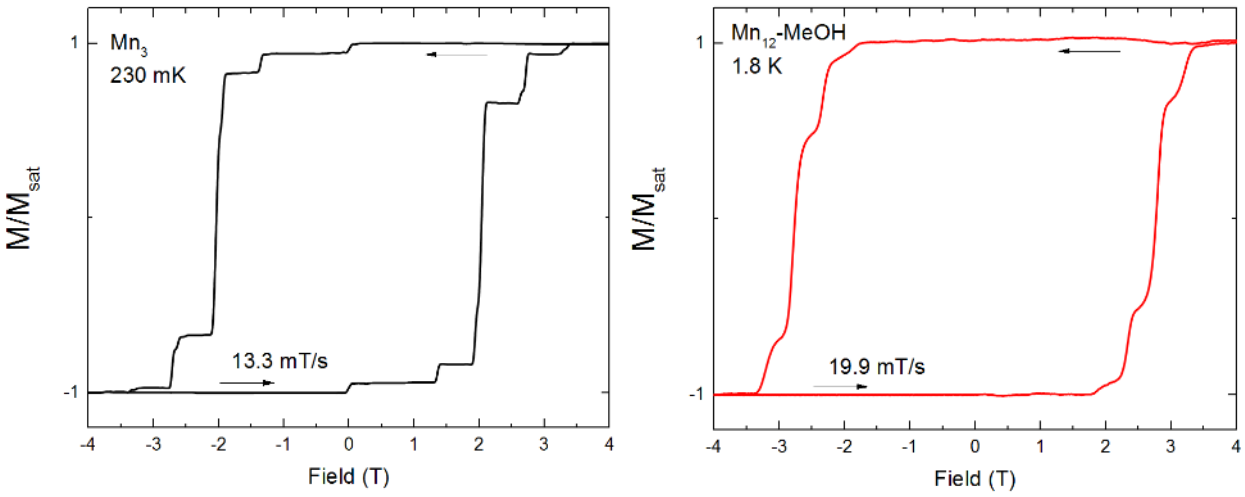

Figure 1.3 – Magnetization data from the two samples studied later in this work, Mn_3 (left, blocking temperature ~2.5 K) and Mn_{12}-MeOH (right, blocking temperature ~3.5 K), plotted as "hysteresis loops" and exhibiting the step-like feature associated with quantum tunneling of magnetization.

1.2 The Single Molecule Magnet

As far as spin systems go, bare electrons are not much of a mystery. A spin ½ system only has two eigenstates and cannot have any potential barrier between them that might inhibit decay from an excited state. Single molecule magnets (SMMs) stand in contrast in both of these respects. As a single molecular unit, they often contain a net spin many times that of a single electron, and due to internal fields and couplings they possess intrinsic anisotropy which forms an energy barrier to the reversal of spin orientation. First characterized and detailed in the early 1990s [4-7], many examples have been synthesized which show magnetic hysteresis at low temperatures and that exhibit the distinctive phenomenon of quantum tunneling of magnetization (QTM), a non-classical relaxation process. Figure 1.3 shows magnetization data acquired from two samples which are discussed at length later in this thesis. Both are plotted as "hysteresis loops" which demonstrate the systems' slow relaxation at the temperatures listed and the step-like features associated with QTM, a sharp contrast to behavior expected for a classical anisotropic system.

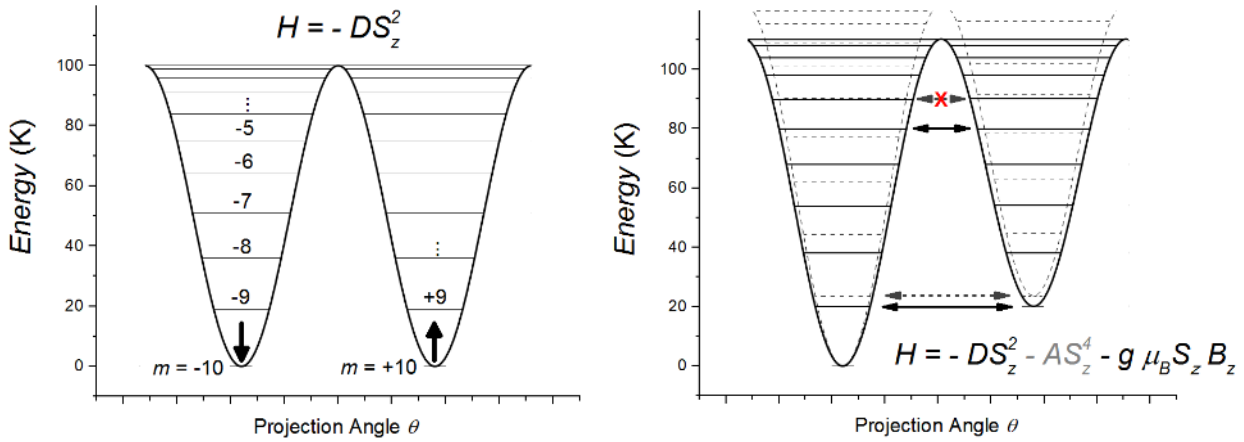

Figure 1.4 – Double well potentials in the absence (left) and presence (right) of a magnetic field B_Z. The right hand plot also contrasts a system with only second order axial anisotropy (solid line) with another which includes a fourth order term (dashed line). Note that by including a fourth order term, excitations for a given k no longer reach resonance simultaneously.

1.2.1 The Double Well Potential

A simple way to represent many aspects of SMM behavior is through a "double well" potential. This formulation produces bistability at low temperature and defines an "easy axis" along which the spin finds a global energy minimum. Writing it out as a Hamiltonian gives

$$H = -D\,S_z^2 - g\mu_B S_z B_z \tag{1.12}$$

where the first term characterizes the uniaxial anisotropy (with D taken to be a positive constant) and the second term describes the Zeeman coupling. Classically, the first term can be equated with a squared-sine potential by substituting $S\cos(\theta)$ for S_z. Figure 1.4 shows a plot of this classical approximation as well as the energies of the eigenstates of the system in zero and non-zero field, with arrows representing QTM transitions between resonant states. Such resonances occur at zero field (where all levels are resonant with the equivalent level of opposite sign) and when an applied field raises/lowers the potentials and equalizes different pairs. The standard convention for labelling a resonance between two levels m, m' is given by $k = -m - m'$.

In the system outlined by Eq. 1.12, resonances occur at regular intervals of $D / g \mu_B$ for all states at a given step *k*. Introducing a fourth order term AS_z^4 acts to shift the resonant fields between higher and lower lying states at the same *k*. The fourth order Hamiltonian is given by

$$H = -D S_z^2 - A S_z^4 - g\mu_B S_z B_z. \tag{1.13}$$

Solving this equation for the resonant field $B(m,m')$ produces the formula

$$B(m,m') = -\frac{m+m'}{g \mu_B}(D + A(m^2 + m'^2)) \tag{1.14}$$

which implies that transitions through higher lying states take place at lower fields when *A* is positive and *D* is negative and dominant.

1.2.2 Transverse Dependence and Quantum Tunneling of Magnetization

Thus far the components in our model have been limited to axial terms, all of which commute with the Hamiltonian. By the Heisenberg picture, this implies that any eigenstate should be stable; as long as our Hamiltonian is free of non-commuting terms, there is no mechanism by which a spin can relax from one well to the other. Indeed, our purely axial Hamiltonian is entirely diagonal, with no elements to link different eigenstates. In order to enable such transitions, we need some actor to break the symmetry of the Hamiltonian in the transverse plane. This can be accomplished in a number of ways, with perhaps the most straightforward being the inclusion of applied field elements B_{xy}.

Through the development of the SMM field of research, it has become apparent that an aspect which sets SMMs apart is their intrinsic transverse anisotropy. A simple example of a Hamiltonian with transverse anisotropy is one which includes the rhombic term E (S_x^2 - S_y^2). Such a system produces an energy landscape in which characteristic “hard” and “medium” axes define additional planes of symmetry with the easy axis (see figure 1.5).

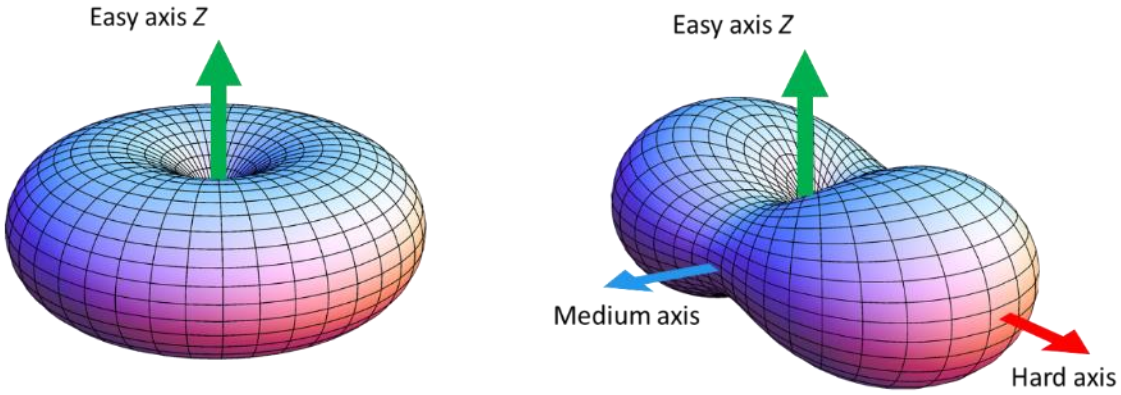

Figure 1.5 – Three dimensional anisotropy barriers calculated for purely axial (left) and rhombic (right) Hamiltonians. Note that the rhombic barrier contains two additional characteristic axes which define the "medium" and "hard" orientations in the transverse plane.

If we recalculate our transition matrix element M, we find non-zero amplitudes when the eigenstates under consideration differ in S by a multiple of two. The reason for this becomes apparent when we rewrite our transverse terms in the S_z basis:

$$S_x = (S_+ + S_-)/2 \tag{1.15}$$

$$S_y = -i(S_+ - S_-)/2 \tag{1.16}$$

where S_+ and S_- are the spin raising and lowering operators, respectively. From this we see that transverse anisotropy, such as the rhombic term $E(S_+^2 + S_-^2)/2$, acts in the same way that a photon might in inducing a transition except that it mixes levels between multiples of $\Delta S = \pm 2$ instead of by only $\Delta S = \pm 1$.

We can see the effect of transverse anisotropy by analysis of the "tunnel splitting" Δ_k which characterizes the "anticrossing" between two eigenstates. Figure 1.6 shows a plot of the energy levels calculated for a $S = 10$ system under the influence of an axial field. In this simulation, the system contains a tetragonal (fourfold symmetry described by $C(S_+^4 + S_-^4)/2$) element in addition to a dominant uniaxial term. The so-called "spin selection" rule for this system determines that eigenstate mixing is prohibited between levels that do not differ in spin by an integer multiple of the symmetry.

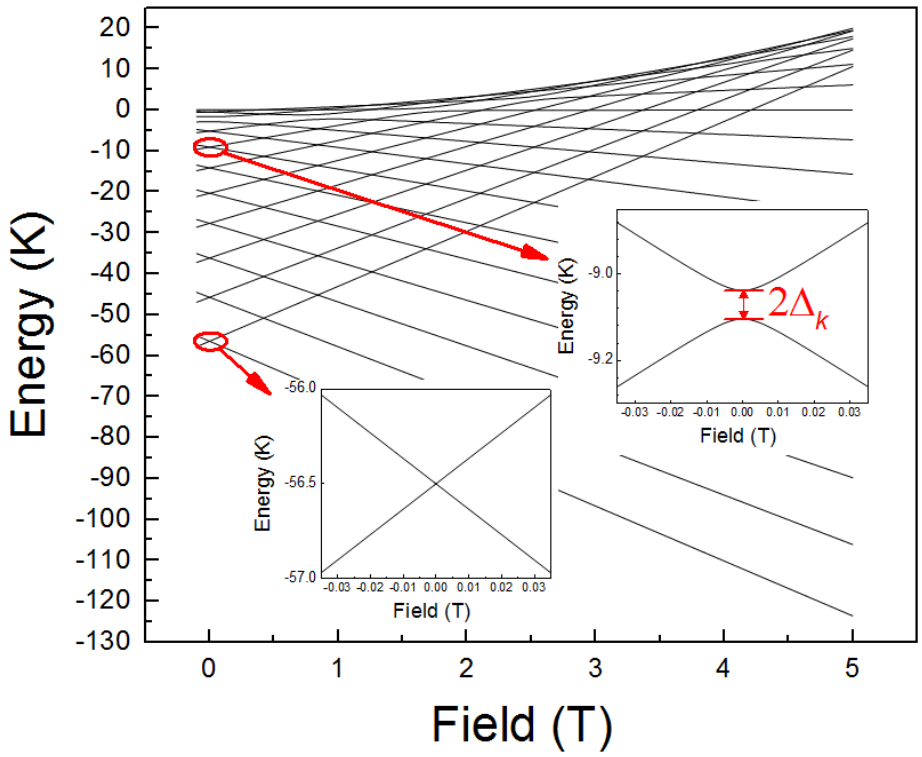

Figure 1.6 – Zeeman diagram of the energy levels and the splittings of a $S = 10$ system with dominant uniaxial anisotropy (D) and significant tetragonal transverse anisotropy. The inset shows the effects of this transverse anisotropy, which mixes levels separated by multiples of the transverse symmetry, as indicated by the insets showing different resonances.

It is also generally true that when it comes to the allowed transitions, states become less mixed as the number of operations necessary to link them increases (i.e. in a fourfold system, two states differing by $\Delta S = 4$ are more heavily mixed as a result of the anisotropy than transitions where $\Delta S = 8$ or 12, for which the fourth-order term operator would have to be applied 2 and 3 times, respectively). When the system is exactly on resonance and two levels would otherwise be degenerate, the states hybridize into symmetric/antisymmetric superpositions split by an energy difference described by tunnel splitting Δ_k. Far from the resonance, the states are close to their unmixed counterparts. One can imagine a spin approaching a resonance (see figure 1.7) in one state and tracing the path past the anticrossing, bending into a new trajectory and ending up in the state it thought it was passing over.

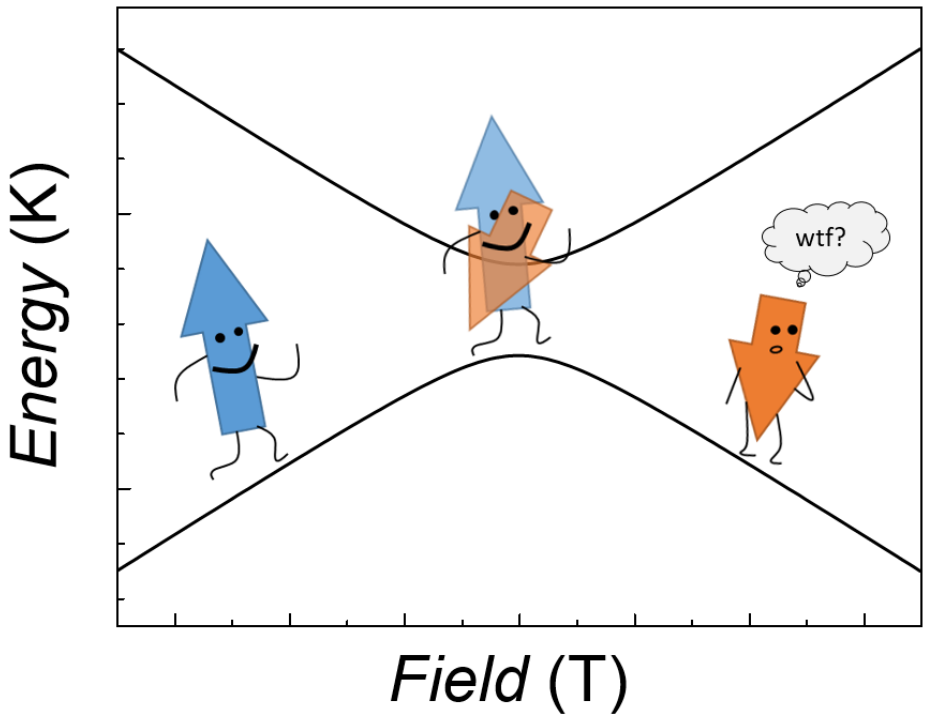

Figure 1.7 – Cartoon in which a spin begins in one state, mixes at an anticrossing, and is left to wonder what happened.

We can relate the tunnel splitting Δ_k to the probability that a spin will complete a transition by the Landau-Zener equation [8]

$$P_k = 1 - \exp[-\frac{\pi\Delta_k^2}{2\upsilon_0\delta}] \tag{1.17}$$

where $\upsilon_0 = g\,\mu_B\,(m - m')$ and δ is the field sweep rate. This equation provides the final link in the chain that begins with a Hamiltonian characterizing the molecular symmetry and ends with magnetic relaxation. This argument forms the bedrock of the analysis performed in Chapter 2, in which the specifics of a Mn_3 based SMM's symmetry and chemistry are related to the patterns observed in QTM from a sample of that compound.

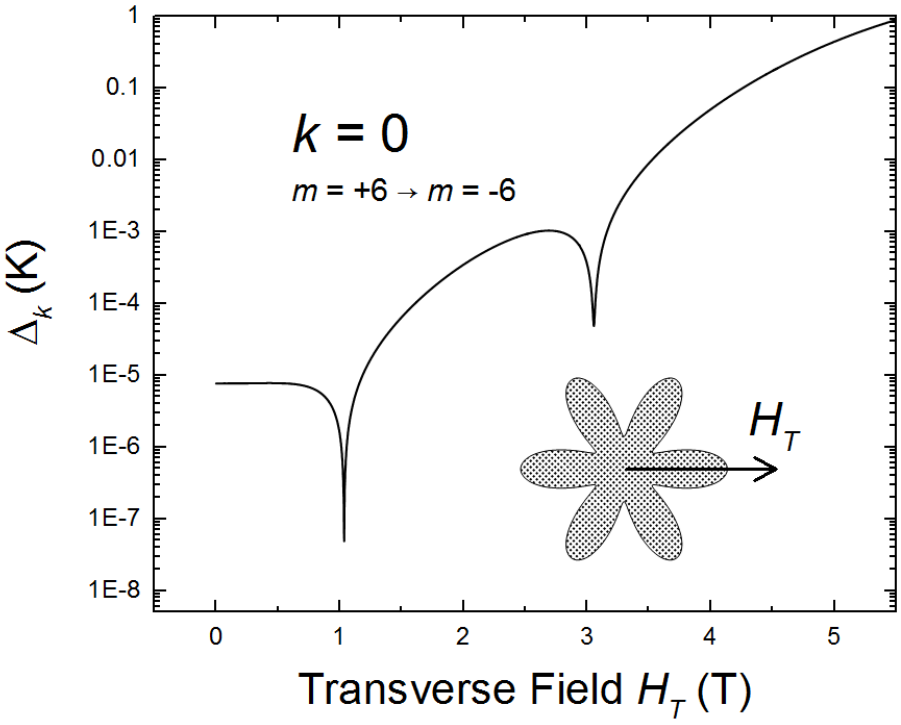

Figure 1.8 – Plot of calculated tunnel splitting showing the effect of Berry phase interference in a S = 6 Mn3 system with sixfold symmetry. This inset illustrates how the field was applied relative to the system's anisotropy barrier.

1.2.3 Berry Phase Interference

At this point we have detailed the relationship between QTM and the intrinsic anisotropy, but have neglected finer discussion of the role played by transverse field elements. As it turns out, the interaction between a transverse field vector and the intrinsic anisotropy is ripe for detailing molecular symmetry, as it can lead to strong modulation of QTM amplitudes and resonance conditions (resonant fields) as a function of the angle of application relative to the molecular frame. In fact, such modulations can lead to dramatic insights into the nature of QTM itself. As was first theorized by Garg et al. [8] and experimentally confirmed by Wernsdorfer et al. [10], an applied magnetic field can lead to a quenching of the tunneling rate, a phenomenon known as Berry phase interference (BPI). The physical interpretation of this phenomenon is that dominant tunneling trajectories of similar amplitudes destructively interfere [11,12] as a result of geometric phases acquired in a path through angular space.

The effects of BPI are evident within the Hamiltonian, bearing directly on the observed tunnel splittings. It has been shown that instances of strong BPI quenching ("BPI minima") have a relationship with the molecular symmetry, with distortions of the energy landscape by a field applied along a symmetry axis creating periodic modulation of the tunnel splitting [10,13]. Fig 1.8 shows the calculated tunnel splitting for a ground state QTM transition as a function of a transverse field applied along one of the hard axes of the Mn_3 system detailed in Chapter 2.

Chapter 2 also details the importance that QTM and BPI can play in the characterization of SMMs, with a full treatment of the angular modulation and modelling of the system's anisotropy. Chapter 3 will discuss an experiment in which uniaxial physical pressure is applied to a Mn_{12} SMM, creating noticeable changes in QTM resonance magnitudes and resonant field positions. We attempt to model these changes by altering the anisotropy parameters in calculations of the relaxation rate. Chapter 4 will take a look at the Spin-Photon interaction under different coupling strength regimes, with brief analysis of the Jayne-Cummings spin-photon model and the sources of decoherence in SMMs, as well as the discussion of several experiments and their goal of exploring different spin/photon couplings.

References

[1] K. Park, M. A. Novotny, N. S. Dalal, S. Hill, and P. A. Rikvold, Phys. Rev. B 66, 144409 (2002)

[2] J. R. Friedman, Chapter in Exploring the Quantum/Classical Frontier: Recent Advances in Macroscopic and Mesoscopic Quantum Phenomena, J. R. Friedman and S. Han, eds. Nova Science, Huntington, NY, (2003)

[3] EasySpin web page "Spin operators and matrices", retrieved from http://easyspin.org/documentation/spinoperators.html Mar 3 2016

[4] Sessoli R, D. Gatteschi, A. Caneschi, and M. A. Novak, Nature (London) 365, 141 (1993).

[5] J. R. Friedman, M. P. Sarachik, J. Tejada, and R. Ziolo, Phys. Rev. Lett. 76, 3830 (1996).

[6] L. Thomas, F. Lionti, R. Ballou, D. Gatteschi, R. Sessoli,and B. Barbara, Nature (London) 383, 145 (1996).

[7] T. Lis, Acta Cryst. (1980). B36, 2042-2046

[8] C. Zener, Proc. R. Soc. A 137, 696 (1932).

[9] A. Garg, Europhys. Lett. 22, 205 (1993).

[10] W. Wernsdorfer and R. Sessoli, Science 284, 133 (1999). [10] A. Name, B. Name, and C. Name, Journal Volume, Pages (Year)

[11] D. Loss, D. P. DiVincenzo, and G. Grinstein, Phys. Rev.Lett. 69, 3232 (1992).

[12] J. von Delft and C. L. Henley, Phys. Rev. Lett. 69, 3236 (1992).

[13] H. M. Quddusi, J. Liu, S. Singh, K. J. Heroux, E. del Barco,S. Hill, and D. N. Hendrickson, Phys. Rev. Lett. 106, 227201 (2011).

CHAPTER 2: BERRY PHASE MODULATION IN A TRIGONAL SYMMETRY MN_3 MOLECULE

The competing demands for minimizing the consumption of computational resources and optimizing model precision come to a head when attempting to diagonalize a large Hamiltonian, such as that of a system with large spin ($|S| \gtrsim 10\ h/2\pi$). The number of operations necessary to complete the eigenvalue algorithm grows with matrix order [1], with the diagonalization of a 125 x 125 matrix requiring about a second of devoted CPU time for a typical desktop computer [2]. This places heavy constraints on the kinds of simulations that can be performed in a reasonable timeframe, especially when considering eigenstates as a function of some incremental parameter, such as magnetic field.

For molecules composed of many ions, a choice must be made as to the level of resolution in modelling their eigenstates and anisotropies. Treating the system as a single rigid spin (the "giant spin" or GS approximation) limits the size of the matrix to at most $2S+1$ but ignores contributions from internal composite states. By including terms for each interaction between constituent ions, the "multi-spin" (MS) treatment allows for the inclusion of intramolecular effects at the cost of a larger Hilbert space.

In work outlined in this chapter, we sought to perform parallel analyses using both the GS and MS methods on a molecular spin system while aiming to understand the implications of each model and to scrutinize their differences. Additionally, we attempted to thoroughly characterize a compound through measurements of QTM resonances and in the process accurately determines its internal structure. Our results show that the observed QTM behavior is highly dependent upon the overall molecular symmetry, or perhaps more accurately, on the interactions between the local ion anisotropies. The next section outlines the sample we chose for study, followed by a description of the experimental methods used to acquire data, then a summary of results, analysis and discussion, and finally concluding remarks.

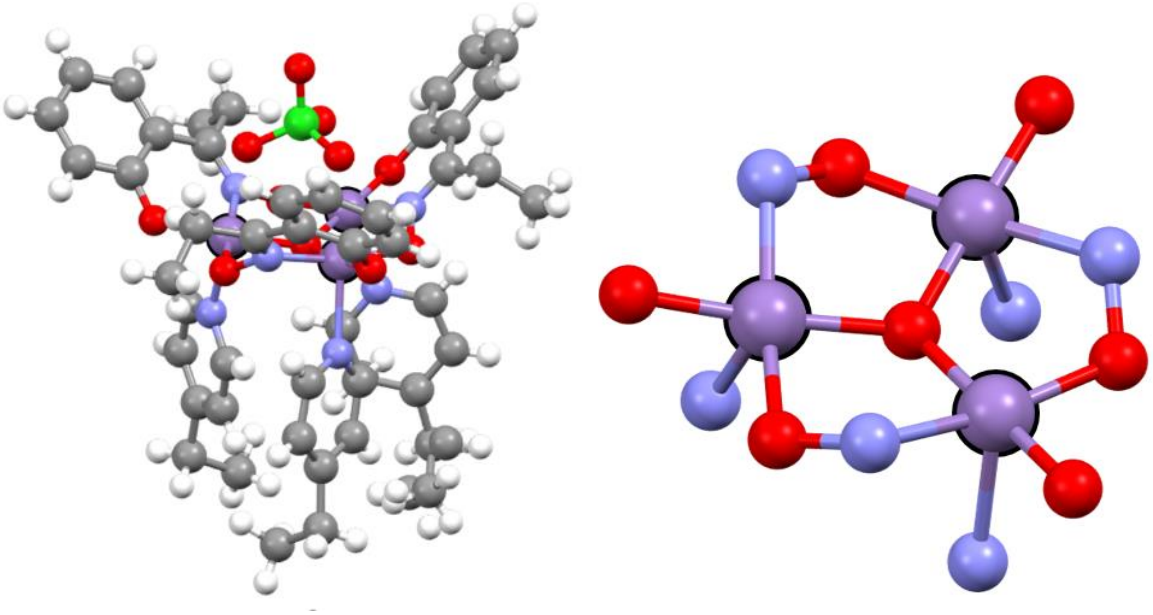

Figure 2.1 - Schematic of the entire Mn3(Et−sao)3(Et−py)3ClO4 molecule (left) and a zoom on its core (right) containing the three exchange coupled s = 2 Mn3+ ions (outlined pale violet spheres). The light blue spheres represent nitrogen sites, the red represent oxygen, the green are chlorine, and the grey and white spheres represent carbon and hydrogen sites, respectively, in the ligands.

2.1 The Mn_3 Molecule

In order to examine the internal degrees of freedom described by a MS Hamiltonian, we needed a system with a low enough number of ions and total spin so that analysis would be computationally feasible. The compound $Mn_3(Et{-}sao)_3(Et{-}py)_3ClO_4$, (henceforth just "$Mn_3$") is a SMM with total spin S = 6 originating from three ferromagnetically coupled s = 2 Mn^{3+} atoms. Figure 2.1 illustrates its chemical structure and details of the core containing the Mn^{3+} ions and interceding N and O sites. With a relatively low total net spin that is split between three ions, both the GS and MS methods are tractable for computation with an incremented applied field parameter (i.e. for hundreds or thousands of diagonalizations of the Hamiltonian).

Previous characterization [3] of the compound indicated that the system has an effective anisotropy barrier $U_{eff} \approx 48$ K, large enough to support slow relaxation of magnetization at temperatures

~1 K, with super-exchange coupling giving an effective isotropic J between the Mn ions of ≈ 5.9 K. The prior characterization also revealed that the packing structure of crystalline samples of this compound contain two species of the molecule which are inverted and rotated by 60 degrees with respect to each other but that are otherwise identical in structure. As it turns out, this is a particularly fortunate configuration, as the anisotropy of the compound proved to be symmetric to such an inversion/rotation and hence both species behave identically in response to any applied field.

In addition to its potential for analysis through both GS and MS Hamiltonians, our interest in this compound was spurred by the trigonal symmetry of the chemical arrangement. As will be discussed in detail below, the relationship between the molecular symmetry and modulation of the QTM behavior is mediated through the anisotropy in the energy landscape described by the spin Hamiltonian. The goal of our measurements was to analyze the QTM behavior for evidence of such a modulation with the expectation that it should present a threefold dependence on angle in the transverse plane. By measuring the intensity of the tunneling resonances as a function of an applied field component H_T in the transverse plane, we were indeed able to record such modulations, with strong evidence for spin selection rules and Berry Phase interference, phenomena which are well understood in terms of transverse anisotropy operators [4-6].

2.2 Instrumentation & Methods

The experiment we wanted to perform had two important requirements: 1) That we could achieve stable temperatures below ~ 4 K, and 2) that we could apply fixed and swept fields along arbitrary directions. To accomplish this, we employed an Oxford Instruments Heliox He_3 cryostat capable of reaching below 250 mK and which could set the sample and measurement devices *in situ* within the field center of an American Magnetics three-axis superconducting vector magnet. This vector magnet could reach field magnitudes up to 7.5 T along one axis (the magnet's "Z" axis) and up to 1.2 T in the plane perpendicular, with sweep rates typically on the order of 0.1 T/minute.

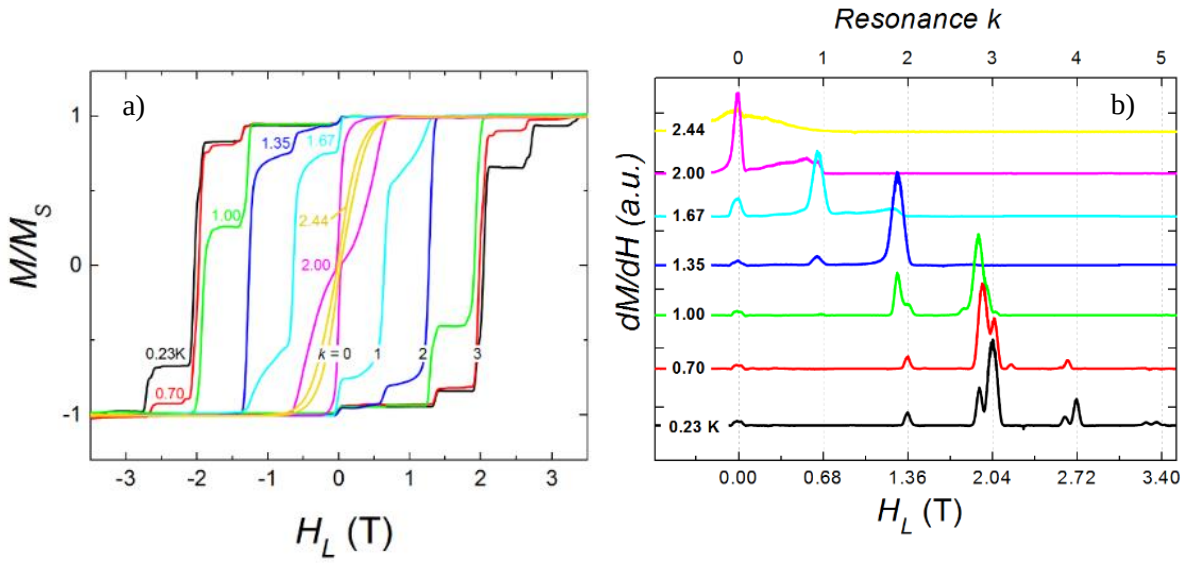

Figure 2.2 – a) Temperature dependence of hysteresis magnetization data acquired from our crystalline Mn3 sample. The approximate resonance positions are labelled according to the convention k = m′ - m. Note that some resonances are evidently split among several transitions (i.e. tunneling through ground or excited states) and/or have indistinct contributions from multiple transitions. The field sweep rate was 0.8 T/minute. b) Derivative dM/dH of the hysteresis showing clear peaks about each resonance position. Note the absence of the k = 1 resonance below ~ 1 K. The data from different temperatures has been offset for clarity.

A Hall bar magnetometer fabricated “in house” was used in conjunction with standard lock-in amplification techniques to record the signal of a sample oriented with its “easy” magnetization axis pointed approximately parallel to the magnet Z axis, with one axis of the plane of the Hall bar’s active area along that same axis (to minimize signal originating from the Z axis field). This particular Hall bar device contained multiple active areas within the same chipset, enabling us to subtract readings from an active area far from the sample in order to remove common background signals. Instrumentation amplifiers were used to balance the signals before being fed into a SRS Sr830 Lock-In. Data was recorded digitally onto a computer running LabVIEW software via a GPIB connection. The magnetization data was recorded in the format common for SMMs, as “hysteresis loops” generated by an applied field swept along the sample’s easy magnetization axis from one saturation to the opposite and then back again. For our sample, this generated the data shown in figure 2.2, which was acquired below the “blocking temperature” at which hysteretic relaxation of the net magnetization becomes evident (here, ≈ 2.5 K).

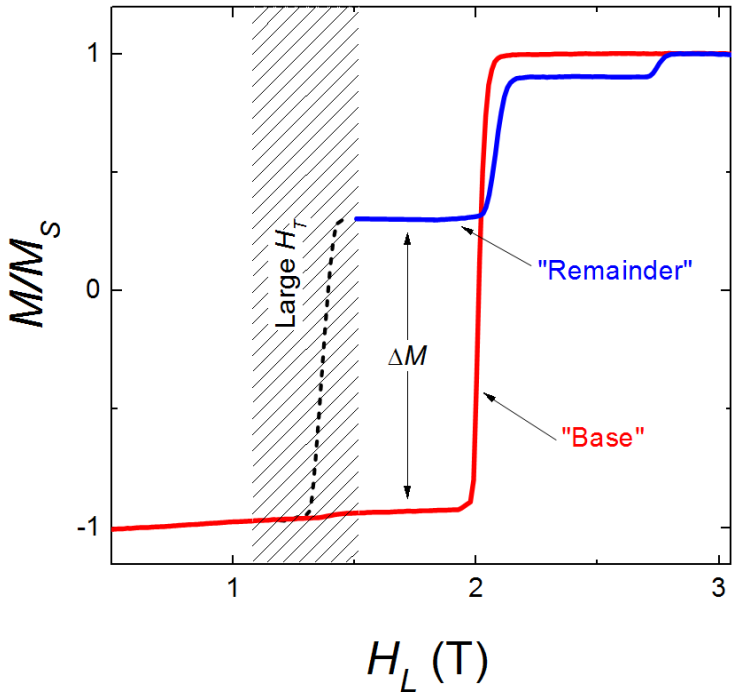

Figure 2.3 – Diagram outlining the "remainder" method by which data from resonances occurring in the presence of large transverse fields could be extracted even if such fields would skew the calibration of the Hall bar magnetometer. The striped region represents conditions where accurate measurements of the sample's magnetization would be impossible due to the quantum Hall effect caused by the necessary transverse field.

The data shows clear step-like features indicative of QTM, with the steps becoming sharper with decreasing temperature.

Perhaps the most critical aspect of this experiment was the measurement of the resonance magnitudes as a function of the fixed transverse field. Successful measurements required precisely maintaining the calibration of our magnetometer while running the applied field through a set of longitudinal (parallel to the easy axis, H_L) field sweeps performed with different fixed components in the transverse plane (H_T). This, however, presents a problem for our Hall bar – in the presence of a large field oriented normal to the active area, the sensitivity of the device becomes dependent upon the Quantum Hall effect, a phenomenon in which the charge in the two-dimensional electron gas potential generated by the AlGaAs/GaAs becomes quantized [7,8], causing oscillations in what would otherwise be a stable signal.

To surmount this challenge, we developed several indirect measurement protocols that used data from undistorted measurements (where $H_T = 0$) while still gathering information from the desired resonance as a function of non-zero transverse field. Figure 2.3 illustrates the principle behind our technique, which we call the "remainder" method. At the lowest temperatures we observed stable (flat) stretches of magnetization data on either side of the QTM steps, enabling us to deduce the amplitude of a step from off-resonance magnetization data acquired immediately before/after the resonance of interest which was swept through while a transverse field was applied and held constant. The sequence of the process went as follows: We first recorded a full sweep worth of magnetization data in the absence of any transverse component, creating a "base" set of reference data. Then we began another sweep under identical conditions which was halted just before the resonance of interest at a point which we determined to have insignificant relaxation. While holding the longitudinal field H_L steady, we swept H_T to the target vector and then swept H_L through the resonance condition to another off-resonant field. The transverse field could then be removed and then the longitudinal swept forward until saturation, creating the "remainder" data set. With these components we could compare the magnetization before and after the resonance with the transverse field on or off, and determine the amount of relaxation that occurred indirectly by the difference. This procedure allowed us to construct a data set of the resonances' magnitudes (described in terms of their probability P, defined as the normalized change in magnetization that occurred during the step) as extracted from hysteresis data collected under different applications of fixed transverse fields.

In addition to the resonance magnitudes' dependence upon transverse field, we were interested in the effect of the molecule's intrinsic anisotropy on the resonance condition. A previous study including work by our group [9] indicated the system's threefold symmetry is expected to produce a "compensating field" effect by which the position of a given resonance (in longitudinal field) would shift as a function of the angle/magnitude of a transverse field. We were particularly interested in the $k = 0$ resonance, which is always expected to occur at zero field. Preliminary estimates were that for 1 T of transverse field we

might expect to see a shift of less than 0.01 T in longitudinal field, an amount much smaller than the resonance width. The need for such a large transverse field also meant that crossing the resonance at even the maximum achievable field sweep rates would lead to a saturated resonance (i.e. fast relaxation to thermal equilibrium), obscuring the "actual" resonance lineshape. And of course we would again encounter issues with Quantum Hall effect degradation of our magnetometer.

Our workaround in this case was similar to the indirect "remainder" method outlined above but designed to sample the leading edge of the resonance. We first swept out to saturation, and then back to a point $H_{L,i}$ close to but far enough from the $k = 0$ resonance that we could expect no relaxation. The longitudinal field and transverse field were then simultaneously and rapidly swept to their target values $H_{L,z}$ and $H_{T,xy}$, and then quickly swept back to $H_{L,i}$ and $H_T = 0$. We could then sweep back towards the initial saturation state and measure the magnitude of any observed resonances, recording this as an account of the net relaxation that occurred during the sweeps to nearby the $k = 0$ resonance (i.e. if there was no relaxation when sweeping close to $k = 0$ then the sample would still be in its initial saturated state and we would expect to see no QTM). By performing this measurement for a range of target longitudinal fields $H_{L,z}$ we were able to derive a conversion factor $dM/dH_{L,z}$ describing the relationship between the change in magnetization (due to the $k = 0$ resonance) and how close we came to the resonance. Finally, we could choose a target $H_{L,z}$ of optimal sensitivity and repeat the measurement for different orientations of the transverse field $H_{T,xy}$. From this we could extract the shifts in the resonance position from any change in relaxation, hypothesizing that the relaxation measured should increase if the resonance had shifted closer to the starting point and decrease if it moved away. Appendix A contains further details and specifics of both this and the "remainder" method.

Armed with these two protocols and the equipment to perform them, we set out to produce a comprehensive set of data detailing the interaction between a transverse field and the quantum tunneling of magnetization as informed by intrinsic molecular anisotropy. We will summarize our results in the next

section and detail how we were able to conclusively relate the symmetries present in a number of properties derived from the QTM to the specifics of the molecular anisotropy.

2.3 Experimental Results

As shown in figure 2.2 a, our sample generated clear magnetic hysteresis and QTM features below ~ 2.5 K, with well separated and sharp steps resolved to the point that transitions out of the ground and excited states were discernible at the lowest temperatures. At a sweep rate of 0.8 T/m, resonances up to $k = 5$ are observable. Figure 2.2 b shows the derivative of the magnetization data, with several of the resonances showing stabile amplitudes (such as the $k = 0$ and 2) as a function of temperature, indicating tunneling from the ground state. The absence of a feature associated with the $k = 1$ at the lowest temperatures is consistent with the spin selection rule [10,11] which forbids tunneling for transitions representing a change in spin number $\Delta m = m - m'$ that is incommensurate with the symmetry. In the case of ground state tunneling at this particular resonance, $m = -6 \rightarrow +5$ and so $\Delta m = 11$. The $k = 2$ resonance ($\Delta m = 10$) is also suppressed at below 1 K (although still visible), while the $k = 3$ ($\Delta m = 9$) appears large.

Initial measurements were performed to locate the sample's easy axis, with axial field sweeps applied across a range of angular orientations, a standard technique which exploits the expectation that a sweep along the easy axis is likely to minimize the field at which the QTM steps occur. Previous characterization indicated that the easy axis was likely to be along the crystalline *c* axis, and the sample was oriented with this in mind. We were able to locate the easy axis within a few degrees of the magnet's Z axis.After locating the easy axis, we could perform measurements of the various resonances' dependencies upon fixed applied field components in the plane perpendicular.

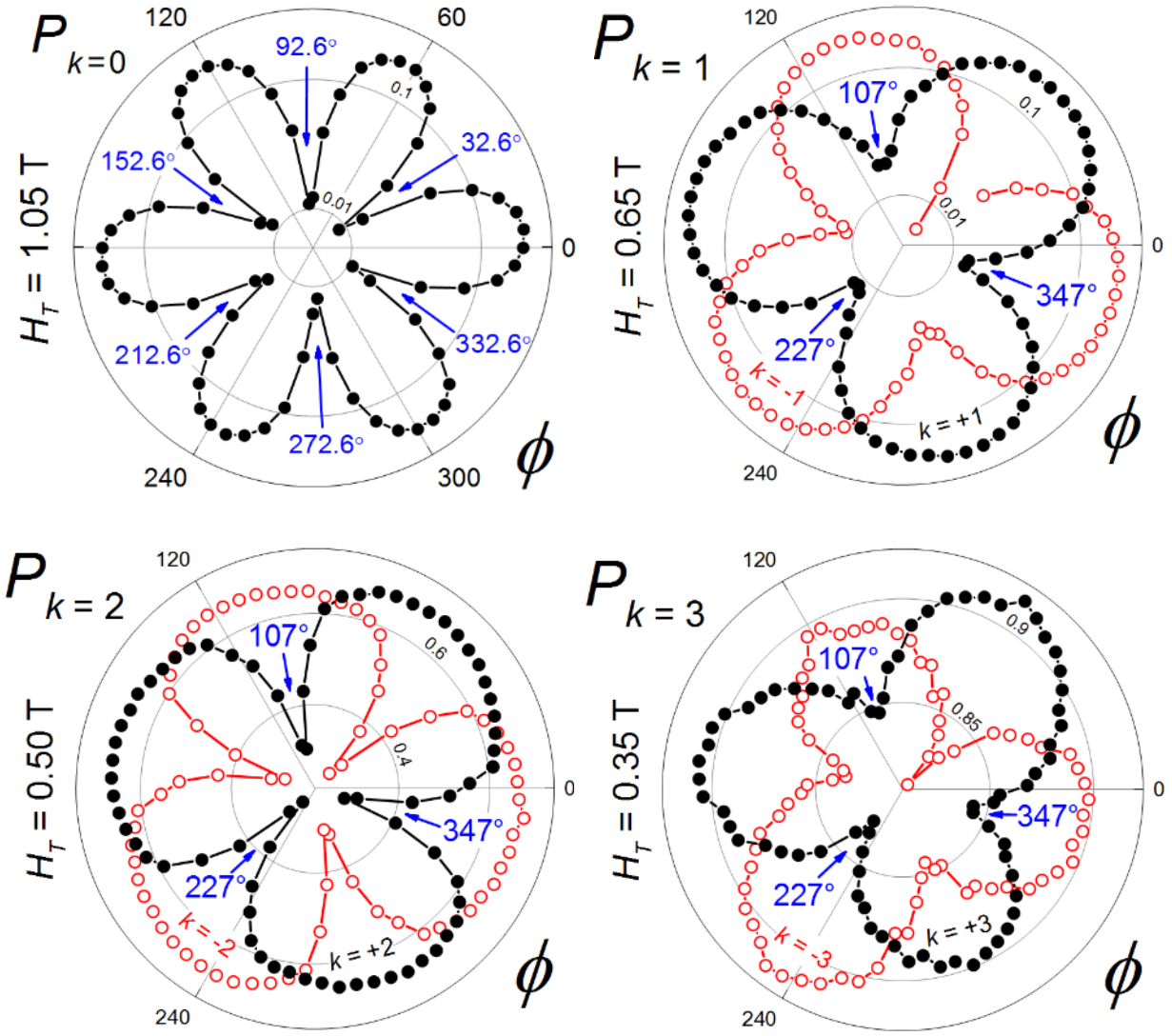

Figure 2.4 – a) Sixfold modulation of the k = 0 tunneling probability as a function of the angle of a 1.05 T transverse field. The sharp minima which occur at the labelled angles are indicative of strong Berry Phase interference which quenches the tunneling rate. b)-d) Threefold modulations of the k = 1-3 QTM resonances as a function of 0.65, 0.50, and 0.35 T transverse fields, respectively.

Based on calculations using the parameters from previous characterization, we estimated that the conditions for significant Berry Phase interference were within the scope of our vector magnet's field output and that we could still expect to see noticeable modulation of the resonance magnitudes far from these BPI minima.

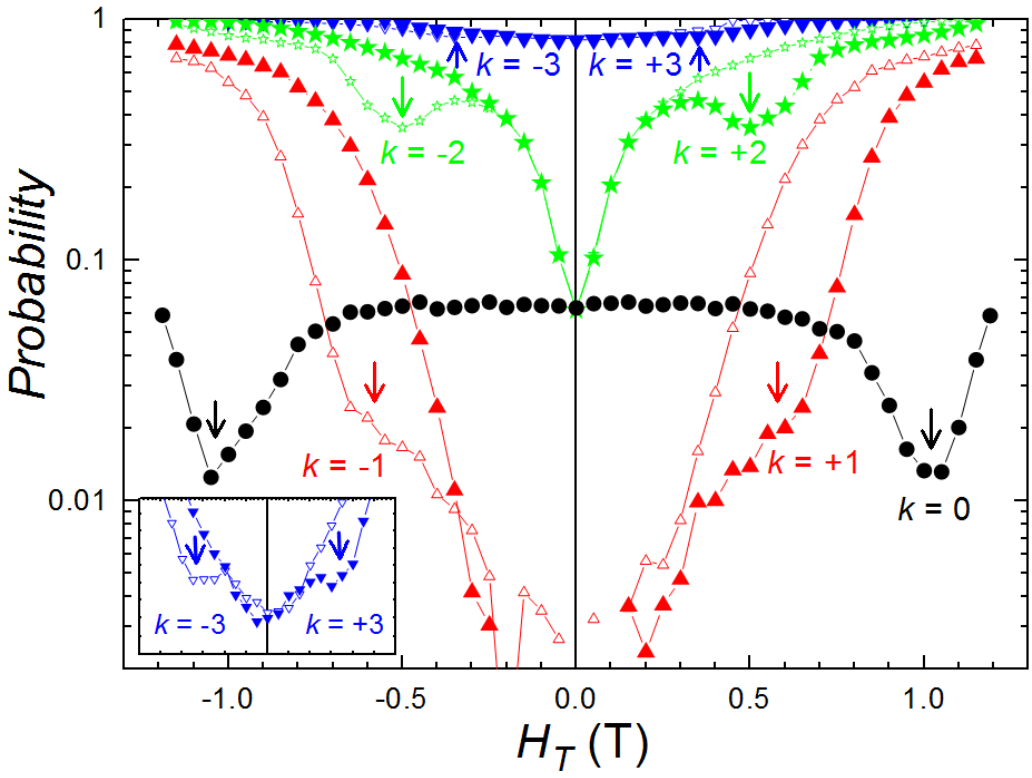

Figure 2.5 – Modulation of the resonance probabilities as a function of transverse field magnitude, with the field swept along the sample's hard/medium axes. The conditions where we observed significant BPI effects are indicated with the arrows and occur at 1.05, 0.57, 0.50, and 0.35 T, respectively. For the resonances which occur with the application of a longitudinal field (k = 1-3), data acquired under both polarizations of H_L are shown, with solid data points representing a positive H_L and hollow data points representing the negative. The overlay of this $\pm H_L$ data illustrates the time reversal symmetry present within the QTM process. The inset shows detail of the k = 3 resonance data in the neighborhood of the BPI conditions.

Such modulation (crossing through BPI minima or not) would allow us to discern the orientation of the molecular frame. The minima lie along directions which largely minimize the tunneling rate, known as the "medium" axes, and are halfway between angles which maximize it, the "hard" axes. Figure 2.4 shows the results of the H_T rotation measurements in polar plots where the radial coordinate represents the probability P of the k = 0, 1, 2, 3 resonances. In this data, the magnitude of H_T was tuned such that the system would land close to the BPI minima for certain angles, indicated in the plots by the blue arrows.

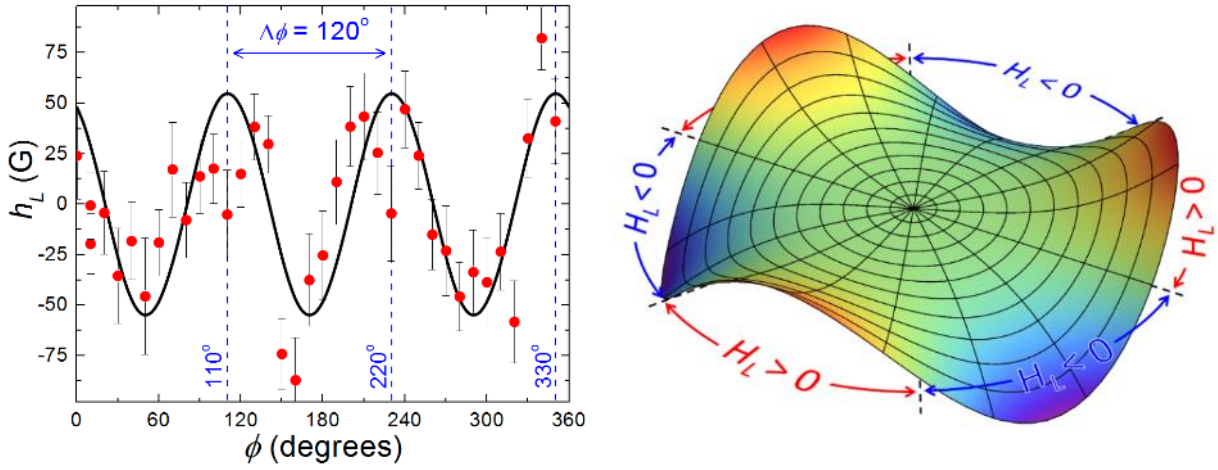

Figure 2.6 – (Left) Data from measurement (red dots) of the compensating field at the k = 0 resonance as induced by a 1.2 T transverse field. The solid line is an estimate of the compensating field generated from a MS Hamiltonian incorporating parameters derived from other data. Note that the directions of the maxima/minima are coincident with the hard/medium axes of the k = 1-3 resonances and not the k = 0. (right) Simulation of the threefold corrugated hard anisotropy plane where the radial dimension represents the magnitude of the transverse field. The alternating regions of positive and negative "compensating field" each span 60°.

For the resonances $k = 1 – 3$, the data show a threefold angular modulation. The observed angular positions of the minima and maxima are inverted for equivalent resonances but with the opposite longitudinal field (i.e. $k = +1$ or -1), with the data from positive and negative field resonances labelled by black and red in the plots, respectively. The $k = 0$ resonance shows a six-fold modulation. Note that angles along which the extrema in probability occur for the $k = 1 – 3$ resonances are coincident, whereas the extrema for the $k = 0$ resonance are found along different directions.

Figure 2.5 shows the results of measurements of the QTM probabilities as a function of the transverse field magnitude. Here, orientation of the transverse field vector was held fixed along one of the directions at which BPI minima occur (the medium axes). Generally speaking, tunneling rates increase with larger transverse field, but this data shows clear evidence of BPI effects where the tunneling rates are minimum and far from zero. Note that for each resonance other than $k = 0$, the minima do not occur again at a simple reversal of the transverse field – the longitudinal field must be reversed as well in order to produce the equivalent features at opposite transverse field. This is a consequence of time reversal

symmetry [12] which dictates that a complete inversion of the applied field is necessary to reproduce the same conditions.

Our final result is outlined in figure 2.6 which shows the modulation of the $k = 0$ resonance condition in terms of longitudinal field h_L as a function of the orientation of a 1.2 T transverse field. This data (red dots) was acquired at an elevated temperature of 1.57 K where tunneling occurs predominantly through the third excited state ($m = -3 \rightarrow +3$, or vice versa) as this transition was expected to show a more pronounced effect than with tunneling out of the ground state. The solid curve is a MS Hamiltonian calculation using the anisotropy parameters derived from other fits to other data (detailed further in the discussion below). Note that the threefold modulation of this property does not follow the angular orientations of the $k = 0$ ground state hard/medium axes (the orientations of the extrema in figure 2.4a), but instead that of the other observed resonances [13]. Although the error bars on the data are large, the majority are within a SD of the expected values and the overall appearance is in good agreement.

These measurements encompass many aspects of QTM behavior, with several characterizations of the dependence upon transverse field and temperature dependence that speaks to the nature of the dominant transitions. The subsequent section discusses the analysis of these phenomena in a spin Hamiltonian framework, both in a GS approximation employing Stevens operators and in a MS model of the local ion anisotropies and their interactions.

2.4 Analysis & Discussion

In light of the wide array of data at our disposal, we hoped to precisely determine a model of the molecule's energy landscape. Within this section, we first discuss our efforts in employing a MS Hamiltonian capable of resolving the system down to the level of the individual ion, shedding light on both the strength of mutual interaction and the orientation of their anisotropies in the molecular frame. This analysis ultimately revealed the sensitivity of different aspects of the BPI phenomenon to independent angular coordinates. The subsequent analysis with a GS Hamiltonian shows that by including

Stevens operators (and the freedom to rotate their frames relative to one another) up to sufficient order, good agreement can be found with both the experimental data and MS model for transitions in which the total spin is maximum, i.e. in which $|S| = 6$ is left unchanged.

In order to interpret our resonance magnitude data, we used the Landau-Zener (LZ) formula

$$P_k = 1 - \exp[-\frac{\pi\Delta_k^2}{2\upsilon_0\delta}] \tag{2.1}$$

where $\upsilon_0 = g\,\mu_B\,(m - m')$ and δ is the field sweep rate. This equation relates the "tunnel splitting" Δ_k which characterizes the mixing of two levels by the size of their anticrossing to the probability extracted from a single pass through some resonance *k*. This approximation has optimal applicability in situations where the probability is small ($P \ll 1$) and tunneling can be assumed to take place through a single transition $m \rightarrow m'$. This formula provides us with means to compare the modulation of our resonances with the tunnel splittings as calculated via the spin Hamiltonian models outlined below.

For our MS model (equation (2.2)), we begin at the level of the constituent $s = 2$ ion and assume that it possesses a rhombic anisotropy which, unlike the simpler purely uniaxial anisotropy, requires the full set of Euler angles for unique identification. From this start we are imbuing the system with a dependence upon both the tilt α of the local ion easy axis away from the molecular symmetry *c* axis and the orientation γ of the equivalent rhombic hard/medium axes. In order to preserve an overall threefold symmetry of the complete system, we construct a three ion model out of three identical rhombic anisotropies rotated 120° with respect to each other such that $\beta_1 = 0$, $\beta_2 = 120°$, and $\beta_3 = 240°$. This model can be described by the Hamiltonian equation which contains all the necessary ZFS components and interactions:

$$\widehat{H}_{\mathrm{MS}} = \sum_i \boldsymbol{s}_i \cdot \boldsymbol{R}_i^T \cdot \boldsymbol{d}_i \cdot \boldsymbol{R}_i \cdot \boldsymbol{s}_i + \sum_i \mu_B \boldsymbol{s}_i \cdot \boldsymbol{g} \cdot \boldsymbol{B} + \sum_{i>j} \boldsymbol{s}_i \cdot \boldsymbol{J}_{i,j} \cdot \boldsymbol{s}_j. \tag{2.2}$$

The first term to the right of the equal sign represents the anisotropy of the individual ions where $\boldsymbol{s}_i$ is the i^{th} ion's spin operator, $\boldsymbol{R}_i$ is a rotation vector characterized by the three Euler angles, and $\boldsymbol{d}_i$ is the ion's rhombic anisotropy tensor given by a diagonal 3 X 3 matrix with values e_i, $-e_i$ (representing the transverse anisotropy) and d_i (the uniaxial anisotropy). The second term characterizes the ions' coupling with an external field $\boldsymbol{B}$ and the last term expresses the superexchange coupling between each pair of ions through the tensor $\boldsymbol{J}_{i,j}$. In our implementation, we assume identical values for the local ion anisotropy constants ($e_i = e$, $d_i = d$) and the exchange interactions ($\boldsymbol{J}_{i,j}$ = isotropic J), and that $\boldsymbol{g}$ is isotropic.

The strength of the local ion anisotropies' d component is implied by the separation between different states with the same total spin S, while the inter-ion coupling J is well defined by the positions of total spin excitations. The transverse component e in the local ion anisotropy plays a similar role to transverse terms in a GS Hamiltonian and informs the modulation of the total tunneling rates (i.e. the angular/magnitude dependencies). Through diagonalization of our MS equation, we find values of $g = 2$, $d = 3.6$ K, $e = -0.62$ K, and $J = 3.1$ K.

At this point, the only free parameters are the two Euler angles α and γ. In order to constrain these angles, we turn to simulations of the BPI minima positions through diagonalization of the MS Hamiltonian which allows us to calculate the splitting for a given resonance as a function of transverse field. Tracking the coordinates of the minima as a function of the two local ion anisotropy tilts, we determined that the magnitudes at which the minima occur are dependent upon the tilt of the local anisotropies away from the molecular symmetry axis. Figure 2.7 shows the calculated positions of the minima in transverse field as a function of α. As can be seen clearly in this plot, a value of $\alpha = 6°$ produces excellent agreement between the calculations and the experimental data.

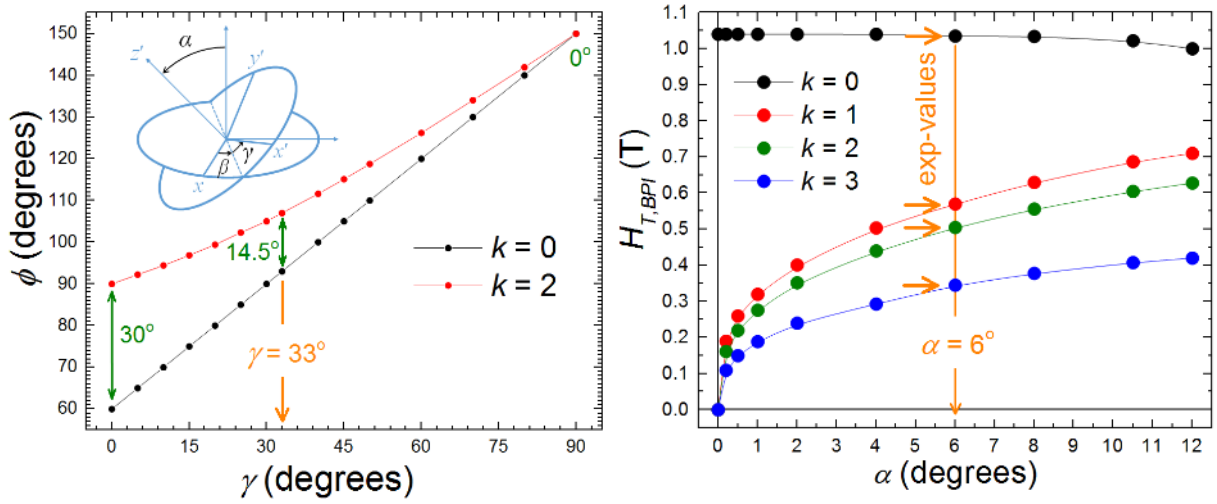

Figure 2.7 – (left) Relative orientations of the hard/medium axes of the k = 0 and 2 resonances as a function of the local ion anisotropy angle γ. The inset details the convention used for the Euler angles. (right) Magnitudes of the transverse field vector at which Berry Phase minima appear for the k = 0-4 resonances as a function of the local ion anisotropy angle α. The fields at which the minima are experimentally observed are indicated by the orange arrows.

The simulations also showed that the relative orientations of the $k = 0$ and the $k = 1 – 3$ hard/medium axes are strongly dependent upon the third angle rotation. Figure 2.7 also shows the calculated angles along which the BPI minima lie for the $k = 0$ and $k = 2$ resonances. Rotating γ from 0 to 90° tunes the difference in angle from 30° to 0°, with a value of $\gamma = 33°$ matching the experimentally observed angular separation. With estimates for these angles, the Hamiltonian equation (2.2) is completely defined and simulations of the tunnel splitting for a given resonance as a function of transverse field (see figures 2.9 and 2.10) closely match the experimental data.

In order to further understand the topography of the energy landscape, it is useful to employ a GS Hamiltonian which can represent the aggregate contributions of the three interacting ions and paint a singular picture with Stevens operators. The data we have discussed so far (in particular, the angular modulations shown in figure 2.4) provide a hint as to which operators might fit best.

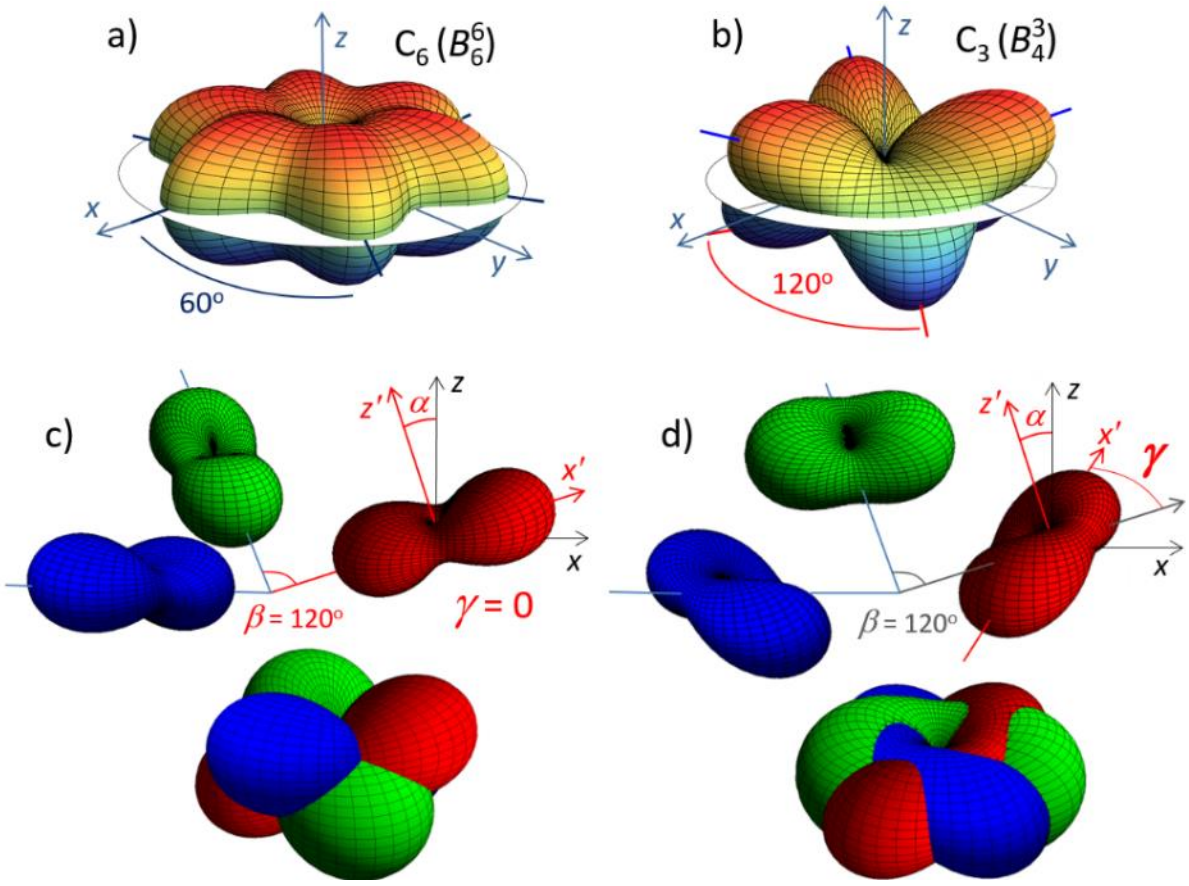

Figure 2.8 – a) & b) Spherical surface plots of the anisotropy barriers represented by the $\mathbf{O}_4^3$ and $\mathbf{O}_6^6$ operators. The white circular planes are cuts through the transverse axes. c) & d) Show 3-D surface plots representing the relative arrangement and combination of the rhombic local ion anisotropies with and without tilts of the angle γ.

The $\boldsymbol{O}_6^6$ and $\boldsymbol{O}_4^3$ operators shown in figure 2.8 reflect the same symmetries seen in the experimental data, with the $\boldsymbol{O}_6^6$ matching the modulation of the $k = 0$ resonance and the $\boldsymbol{O}_4^3$ producing alternating threefold symmetries in cuts through the top or bottom half (see figure 2.12). With this in mind, the GS Hamiltonian can be written

$$\widehat{H}_{GSA} = D\boldsymbol{S}_z^2 + B\boldsymbol{S}_z^4 + B_4^3\boldsymbol{O}_4^3 + B_6^6\boldsymbol{O}_6^6 + \mu_B\boldsymbol{B}\cdot\boldsymbol{g}\cdot\boldsymbol{S} \qquad (2.3)$$

where D and B are the second and fourth order anisotropy coefficients, respectively, which define the easy axis orientation through the spin projection operator $\boldsymbol{S}_z$, B_4^3 characterizes the strength of the anisotropy expressed by the operator $\boldsymbol{O}_4^3 \equiv \frac{1}{2}[S_z\,,\, S_+^3 + S_-^3]$, and B_6^6 is the corresponding parameter for the

hexagonal term $\boldsymbol{O}_6^6 \equiv \frac{1}{2}[S_+^6 + S_-^6]$. The final term is the Zeeman coupling, which we employed with an isotropic $g = 2$. The presence of a B_4^3 term is interesting for its inclusion of a longitudinal term within the associated operator $\boldsymbol{O}_4^3$. This couples the "easy axis" Z field to the transverse field (as represented in the spin raising/lowering operators), creating the "compensating field" effect as we observed in figure 2.6.

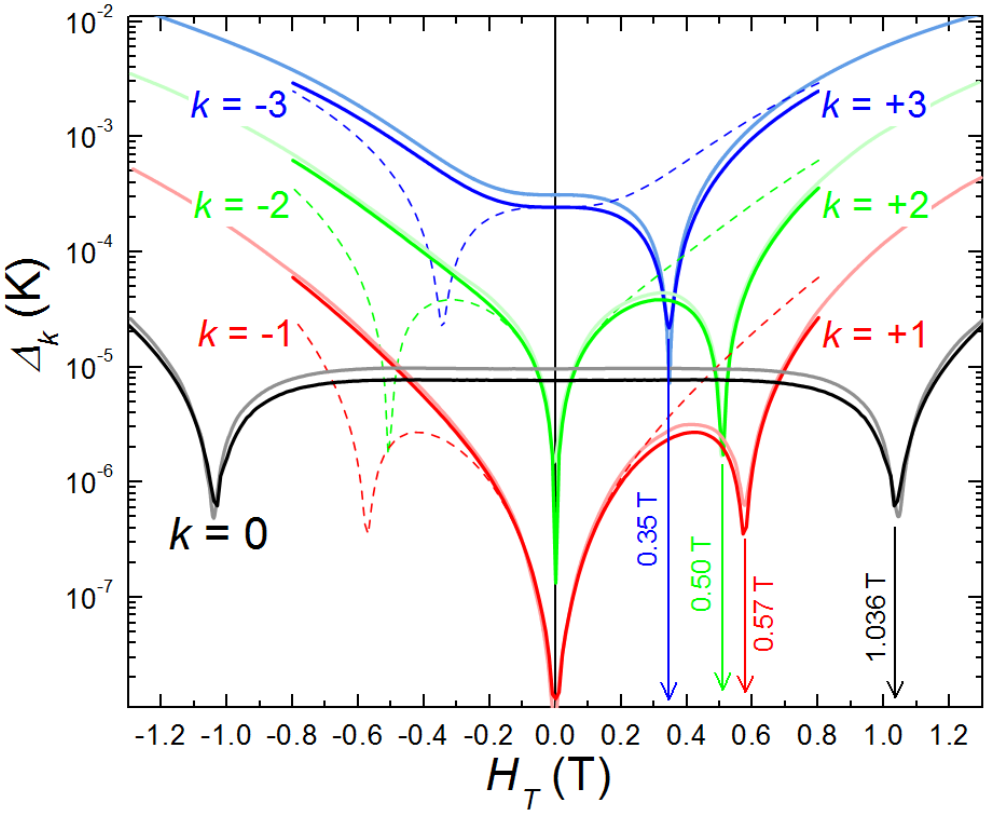

Figure 2.9 – Simulated tunnel splitting as generated from the MS model (dark/dashed lines) and GS approximation (transparent lines). Note that these models both predict the asymmetry in the k = 1-3 splittings. The relative sharpness of the k = 2 resonance (as compared to, say, the k = 1) helps explain why this resonance is observed in experimental data despite indications that it should be quenched in the absence of any transverse field (the splitting falls far below that of the k = 0 resonance as H_T goes to zero).

Comparing the GS to the MS local ion anisotropies reveals the important role that the local tilt angles α and γ play in the correspondence between the Hamiltonian terms in each model. A simple system in which the local ion anisotropies are not tilted away from the molecular symmetry axis (but with $\beta_1 = 0$, $\beta_2 = 120°$, $\beta_3 = 240°$) produces a shape equivalent to a GS B66 symmetry (see figure 2.8). Including the α tilt breaks the sixfold symmetry, creating the kind of alternating threefold symmetry represented by a B_4^3

term. Further including the γ rotation results in a system which has an appearance resembling some synthesis of the pure B_6^6 and B_4^3 components.

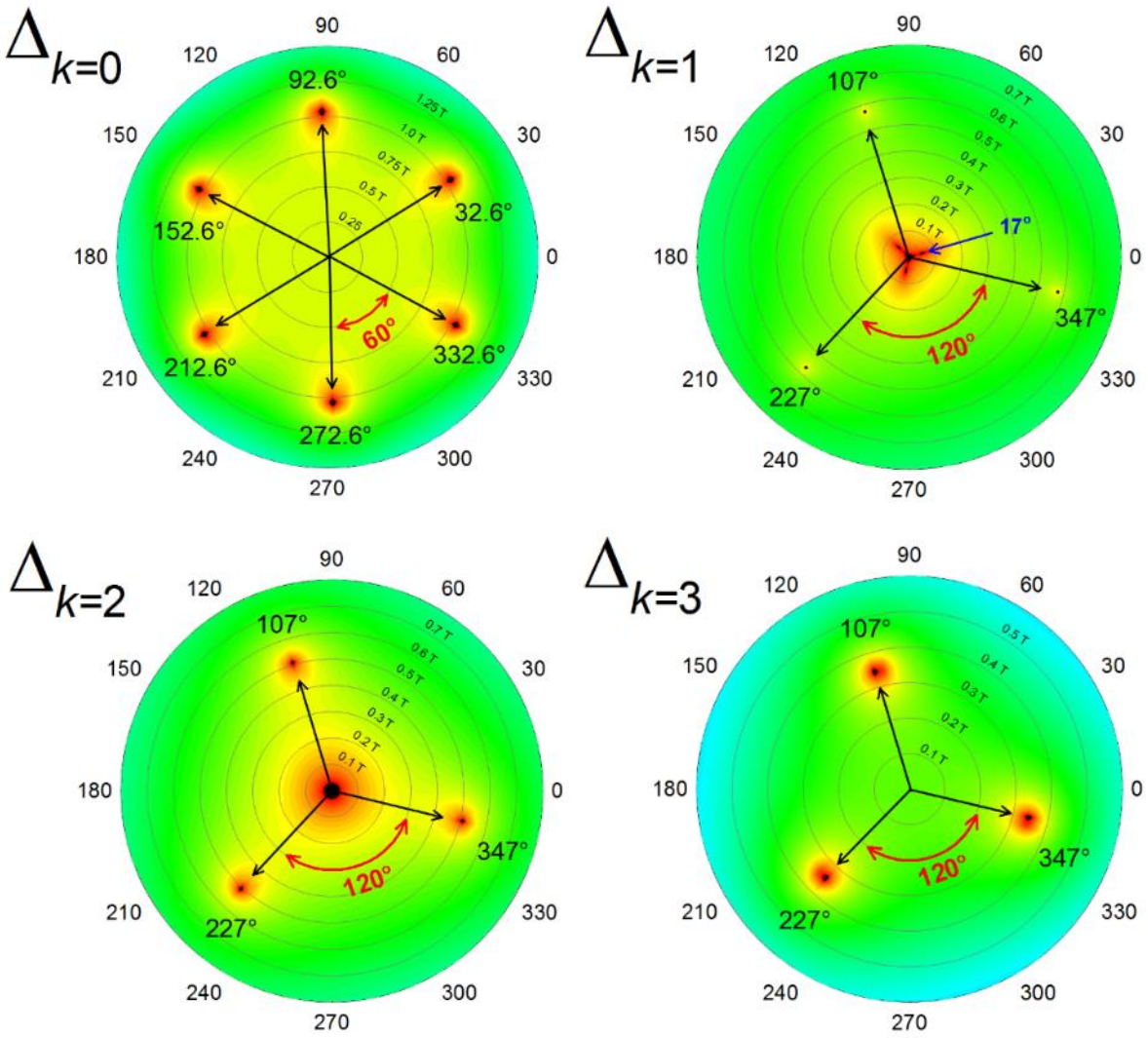

Figure 2.10 – Contour polar plots of calculated splittings generated from the MS model. The dark spots representing regions with predomination tunnel quenching due to BPI effects.

Simulations employing a GS model reproduce transverse field angle and magnitude dependence that closely match those of the MS model. However, it was necessary to artificially rotate the frame of the $\boldsymbol{O}_4^3$ operator by 15° (relative to the $\boldsymbol{O}_6^6$) in order to find the best agreement. Such a rotation is consistent with the relative orientations of the threefold and six-fold features observed in the experimental data and the MS model. This illustrates the correspondence between the k = 0 and the B_6^6 term and the k = 1-3 and

the B_4^3. Indeed, the pattern of the $k = 0$ resonance's magnitude modulation for a $H_T = 1.05$ T transverse field is largely unchanged in the presence or absence of the B_4^3 term, whereas the pattern of the compensating field (which is threefold and follows the orientations of the B_4^3 term) vanishes entirely when that term is removed. This implies that the B_6^6 component is dominant in the $k = 0$ resonance, at least in this neighborhood of transverse field. For the resonances which occur in the presence of a significant longitudinal component S_z, it is the B_4^3 that term dictates the modulation of the splittings.

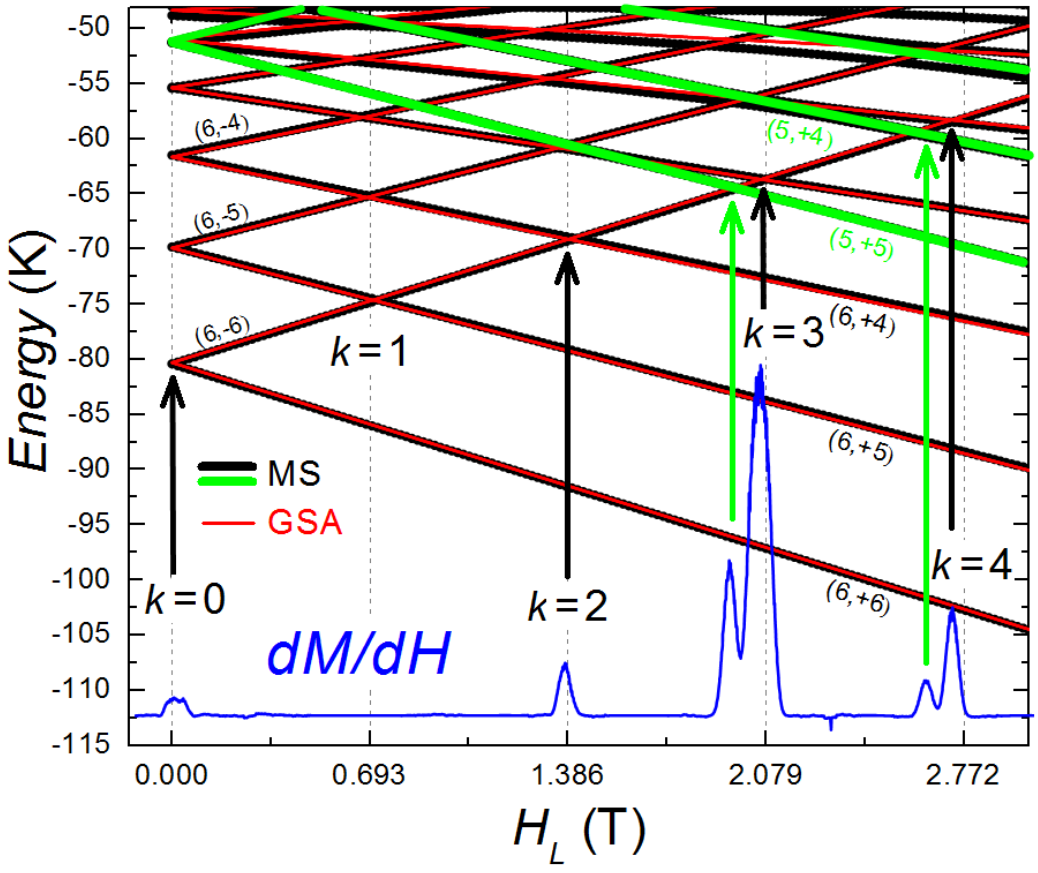

Figure 2.11 – Plot of the Zeeman split energy levels as a function of longitudinal field. The black lines represent eigenstates calculated by the MS model with a total spin $S = 6$, whereas the green lines represent eigenstates that the model attributes to total spin excitations (S = 5). The red overlay is generated from the GS Hamiltonian, which fails to reproduce the total spin excitation states. The blue line is the derivative dM/dH extracted from measurements and shows peaks which match the positions of transitions with both $|S| = 5$ and 6.

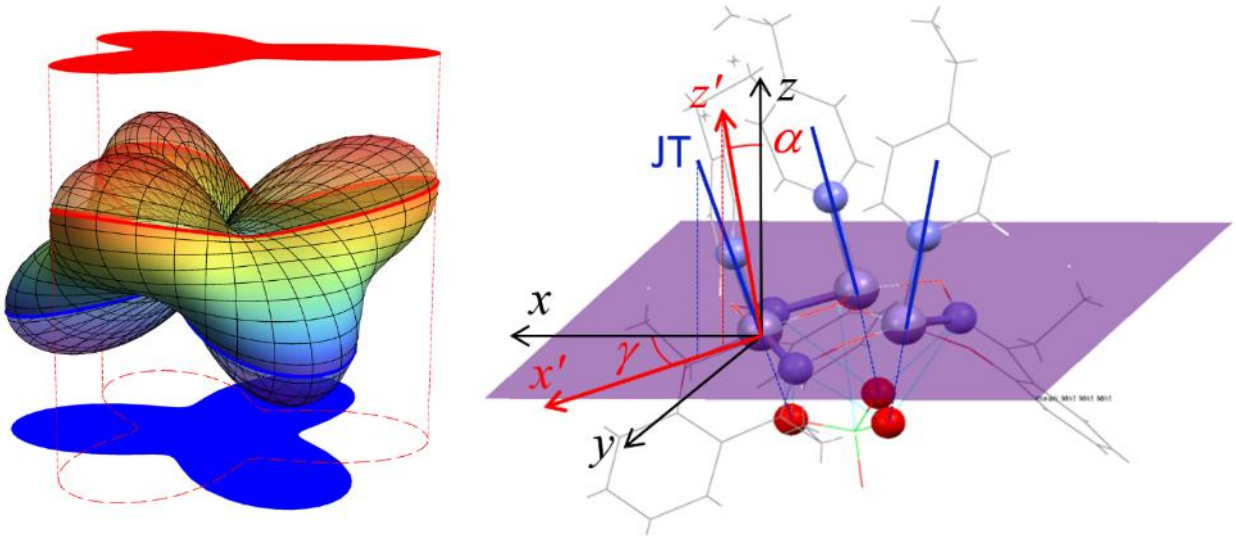

Figure 2.12 – (left) Plot of the anisotropy barrier generated by the $\mathbf{O}_4^3$ operator, with cuts along the border of the opaque/transparent regions at opposite inclinations reflecting how the threefold pattern of modulation is inverted with respect to the sign of the longitudinal field. (right) Diagram of the core of the Mn_3 molecule with the axes of O-Mn-N bond (which is the presumed JT axis) highlighted by the blue lines. The orientation of the estimated local ion anisotropy is along the red z′ axis.

The precision afforded by the MS fitting allows for direct comparison between the ions' rhombic anisotropies and other characteristics of the individual ions' chemical arrangement (see figure 2.12). For this compound, the Jahn-Teller (JT) axis of the Mn3+ ions are expected to lie approximately along the direction of the O-Mn-N bonds. The orientation of local ion easy axis *z* is roughly 12° degrees away from this direction, a significant deviation.

Finally, we are able to draw important conclusions about the relative intensities of the observed steps. As mentioned previously, the "forbidden" $k = 1$ resonance is absent at the lowest temperatures while the also "forbidden" $k = 2$ is small but present. We can understand this by looking at the results of the H_T dependence simulations in figure 2.9. The calculated splittings for the $k = 0$ and 3 resonances, which are both integer multiples of the molecular symmetry, are flat about zero transverse field. In contrast, the $k = 1$ and 2 resonances show a sharp dip about zero transverse field, consistent with the spin selection rule. The shape of the $k = 1$ resonance's splitting is however much broader, not rising above the level of the $k = 0$ splitting until ≈ 0.5 T, while the $k = 2$ splitting increases dramatically with even 0.1 T

producing a splitting much larger than the $k = 0$. This implies that even a small transverse field is enough to bring this transition to prominence, while leaving the other hidden. It is also worth reiterating the presence of peaks which closely match the position of total transitions involving spin excitations ($|S| = 5$, see figure 2.11), drawing a stark line around the limits of the GS model.

2.5 Conclusions

The data outlined in this chapter is the result of the great quality of both the experimental equipment and the sample we were fortunate to study. The overlap between the conditions for clean QTM steps, BPI effects, and the capabilities of the magnet and cryostat enabled a broad range of fascinating measurements. By performing analysis with both MS and GS models to a comprehensive set of data, we have been able to extract information at the interatomic level, resolving a difference between the Jahn Teller and local anisotropy axes. We've also been able to further demonstrate the importance of precision in the characterization of the anisotropy when attempting to accurately model the QTM behavior. The need for dislocation of the $\boldsymbol{O}_4^3$ and $\boldsymbol{O}_6^6$ operators in the GS Hamiltonian also illustrates the necessary degrees of freedom for applicability of that model. The strong agreement between the simulated splittings and observed resonance probabilities also provides answers to questions regarding the applicability of spin selection rules, pointing to the presence of internal dipole fields and as a driver of QTM behavior in some of the forbidden resonances observed here.

While both the GS and MS models reproduce many of the same features with accuracy, the former system requires two sets of anisotropy operators to span the full set of measurements, whereas the perhaps more naturally forms a landscape distinct from either form out of the conjunction of three simpler shapes.

The understanding this work has been able to achieve points to the continued promise of such molecular spin systems for new applications. By providing two models with tradeoffs between their

respective levels of detail and computational demands, this Mn_3 compound stands as a system ideal for study when a range of prominent and exact QTM features are called for.

References

[1] Press, William H.; Teukolsky, Saul A.; Vetterling, William T.; Flannery, Brian P. (1992). Numerical Recipes in C (2nd ed.). Cambridge University Press. ISBN 0-521-43108-5.

[2] as performmed in Mathematica using a Timing[] command, running on a "quad-core" CPU @ 3.10 GHz, the author's computer

[3] R. Inglis, S. M. Taylor, L. F. Jones, G. S. Papaefstathiou, S. P. Perlepes, S. Datta, S. Hill, W. Wernsdorfer, and E. K. Brechin, Dalton Trans. 42, 9157 (2009).

[4] E. del Barco, A. D. Kent, E. M. Rumberger, D. N. Hendrickson, and G. Christou, Phys. Rev. Lett. 91, 047203 (2003).

[5] S. T. Adams, E. da Silva Neto, S. Datta, J. Ware, C. Lampropoulos, G. Christou, Y. Myaesoedov, E. Zeldov, and J. Friedman, Phys. Rev. Lett. 110, 087205 (2013).

[6] C. M. Ramsey, E. del Barco, S. Hill, S. J. Shah, C. C. Beedle, and D. N. Hendrickson, Nat. Phys. 4, 277 (2008).

[7] K. Klitzing, G. Dorda, and M. Pepper, Phys. Rev. Lett. 45 (6): 494–497 (1980).

[8] R. B. Laughlin, Phys. Rev. B 23, 5632 (1981)

[9] J. Liu, E. del Barco, and S. Hill, Phys. Rev. B 85, 012406 (2012).

[10] J. J. Henderson, C. Koo, P. Feng, E. del Barco, S. Hill, I. Tupitsyn, P. Stamp, and D. Hendrickson, Phys. Rev. Lett. 103, 017202 (2009).

[11] J. Liu, E. del Barco, and S. Hill, Molecular Magnets: Physics and Applications, edited by J. Bartolome, F. Luis, and J. F. Fernandez (Springer, New York, 2013).

[12] H. M. Quddusi, J. Liu, S. Singh, K. J. Heroux, E. del Barco, S. Hill, and D. N. Hendrickson, Phys. Rev. Lett. 106, 227201 (2011).

[13] Although angular modulations of this particular transition were not measured, calculations indicate that it should follow a similar pattern as the measured ground state transition

CHAPTER 3: THE EFFECT OF UNIAXIAL PRESSURE ON THE QUANTUM TUNNELING OF MAGNETIZATION IN A Mn_{12} SINGLE MOLECULE MAGNET

In the previous chapter, we demonstrated the relationship between molecular symmetry and QTM behavior. We also shone light on how that overall symmetry can be traced to internal degrees of freedom within a SMM. While the capability to finely tune molecular properties of SMMs at the point of chemical synthesis has grown substantially in recent decades, cases where a property of the compound can be varied continuously are limited. In the research outlined in this chapter, we attempted to induce distortions of the molecular anisotropy via uniaxial pressure. We applied this pressure along two directions – along the sample's easy axis and in the transverse plane, configurations referred to as "parallel" and "perpendicular", respectively. As of a function of pressure, the step magnitudes were observed to grow in both arrangements of pressure, while pressure applied along the sample's easy axis resulted in shifts of the resonant field towards zero and pressure applied perpendicular had the opposite effect. After extracting estimates for the pressure dependence of the magnitudes/resonant fields with linear fits, we attempted to model these changes in relaxation by varying anisotropy parameters within a Spin Hamiltonian and simulating the QTM behavior.

The topics covered in this chapter begin with details of the compound under study, $[Mn_{12}O_{12}(O_2CCH_3)_{16}(CH_3OH)_4] \cdot CH_3OH$ (called "Mn_{12}-MeOH" for short), then continue through discussions of the experimental equipment and techniques, the data acquired, the methods of analysis, interpretation, and concluding remarks.

3.1 The Mn_{12}-MeOH Molecule

The sample under study here has the chemical formula $[Mn_{12}O_{12}(O_2CCH_3)_{16}(CH_3OH)_4]CH_3OH$, henceforth called "$Mn_{12}$-MeOH", and is a high symmetry analog [1,2] of one of the first SMMs to be discovered, $Mn_{12}O_{12}(CH_3COO)_{16}(H_2O)_4$, a.k.a. "$Mn_{12}$-Ac". Both of these systems show a S = 10 ground

state, a large energy barrier to spin reversal U_{eff} of about 70 K, and exhibit magnetic hysteresis at field sweep rates on the order of 1 mT/s below about 3.5 K. In crystalline samples like those examined here, the large step-like features associated with QTM are visible every ~0.45 T or so, with the first appearing at 0 T as the field is swept from one sample polarization to the other, at the lowest temperatures. Through method of synthesis which eliminates solvent disorder, Mn_{12}-MeOH presents a system of higher symmetry than Mn_{12}-Ac, with resonant features free of the broadening induced by solvent disorder.

3.2 Experimental Equipment and Techniques

Numerous hydrostatic studies have been conducted in the effort to characterize stress induced effects in the magnetic behavior of a SMM [3-7], with pressure applied through compression of a fluid medium which applies stress arbitrarily to the sample. Our experiment was designed to deliver pressure along a particular axis of the sample. The samples studied here were small, narrow crystals with a length no greater than a millimeter.

In order to aide placement and reduce the risk of crystal fracture, a method outlined by Campos Brooks et al. [8] was employed in which the samples were first set in epoxy (Stycast 1266) and then formed (machined) after curing in a mold. The process went as follows: After removal from the mother liquor and a short drying, the crystalline samples were placed into wet, degassed epoxy within a Teflon mold and then oriented by the application of a large field held fixed for several hours until the completion of the curing process. This epoxy piece containing the sample was then machined into a small cuboid "pellet", with short dimension not much longer than the length of the crystal itself, such that one of the flat faces of the sample was close to one of the flat faces of the pellet. The cured epoxy pellet containing the embedded crystal was placed within a "bracket" designed to hold a Hall Bar magnetometer and G10 "fingers" designed to deliver pressure to two opposing faces of the crystal.

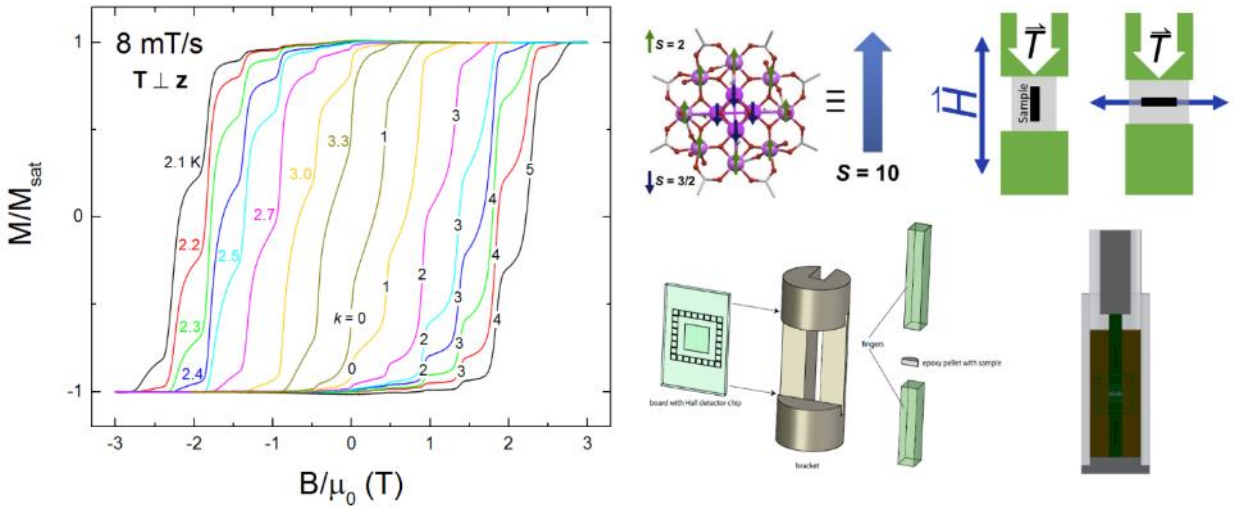

Figure 3.1 - (a) Temperature dependence of magnetization data plotted as hysteresis "loops", acquired under ambient conditions at a longitudinal field sweep rate of 8 mT/s, labelled by their resonance number k = m – m' and temperature (in K). (b) Schematic of the molecular core of Mn12-MeOH, from [16], with the dark blue/green arrows illustrating relative spin orientations of the individual ions and a large blue arrow representing a collective "giant spin". (c) Diagram showing the relative orientations of the sample and magnetic within the pressure apparatus. The sample's "easy" magnetization axis is taken to be along the long dimension or the black box. (d) Detailed schematic of the high-pressure cell within the low temperature portion of the apparatus showing the arrangement of the hall-bar sensor and the elements that deliver pressure to the sample, taken from [17]. Note that shape of the epoxy "pellet" used in this experiment is close to a parallelepiped.

The sample was aligned with the active area of the Hall sensor to achieve the best coupling possible. The bracket containing the embedded sample and sensor was then inserted in a stainless steel cell at the bottom of an apparatus designed to deliver pressure to the sample from a pneumatic piston outside of the cryostat.

The apparatus was constructed out of non-magnetic stainless steel and aluminum. The low temperature portion was comprised of a cell which could be set at the bottom of a cryostat, placing it within the field center of a superconducting coil magnet (of a Quantum Design PPMS). The cell was connected to a thin wall stainless steel tube which ran the length of the sample space to the room temperature portion. The top of the tube was connected to the casing of a pneumatic piston which could deliver pressure to a steel rod. The length of the rod ran back down through the thin walled tube where it was connected to a narrow hollow steel tube (to minimize thermal coupling to the low temperature

portion) capped with an aluminum plug extending into the cell. When the components were in place, this plug delivered the pressure to the components in the bracket. The pressure within the pneumatic piston was controlled by a compressed gas (N_2) regulator. Teflon o-rings were placed between the central rod and thin wall tube to reduce thermal convection. The apparatus was essentially identical to that used in a previous experiment [9]. See figure 3.1 for diagrams of outlining the high pressure portion of the apparatus.

Two Quantum Design PPMS systems were used to achieve temperature control and apply a magnetic field, each with similar instrumentation but different orientation of the magnetic field axis. In the first system, the field axis was aligned with the bore of the sample space. In the second, the field axis was perpendicular to the sample space bore. We define the stress axis **T** as the direction normal to the opposing parallel surfaces of the sample to which pressure was applied. In the first system, the sample was aligned such that its "easy axis" (collinear with the long axis of the crystal) is parallel to the magnetic field, which is also parallel to T. This is the "parallel pressure" configuration. In the second system, the "easy axis" and magnetic field are again collinear, but T is oriented orthogonally to both. This is the "perpendicular pressure" configuration. In the perpendicular configuration, the pressure was applied along one of the flat faces of the crystal presumed to be in the hard plane, a direction which is associated with the "hard" anisotropy axis of this sample.

Once the sample and bracket were in place, the apparatus was inserted into the PPMS cryostat and cooled. LabVIEW and Quantum Design software were used to control the application of the field and record data in digital format. Hall resistance from our sensors was measured using a lock-in amplifier supplying current to and reading voltage from orthogonal contacts. The applied field was swept at rates of 1.1 mT/s and 19.9 mT/s in the parallel pressure configuration and 8 mT/s in the perpendicular. Measurements were performed across a range of temperatures from 2.1 to 3.3 K as read from a calibrated thermometer placed on the back of the Hall Bar in the parallel case and according to the PPMS system

thermometer at the sample space position in the perpendicular. Figure 3.1 shows hysteresis loops acquired while in the perpendicular system for each temperature at ambient pressure. The sequence of data acquisition began with adjustment of the pressure and then collection at several temperatures before moving on to the next pressure. For the parallel experiment, the chronological sequence of pressures began with ambient ("zero" pressure in the piston) and then continued 0.55, 1.1, 1.64, 0.27, 0.82, 1.37, and 1.92 kBar. For the perpendicular experiment, the order was 0.41, 0.82, 1.23, 1.64, 2.05, and finally 0 kBar. The upper limit of the pressures was informed by the expected tensile strength of the epoxy at low temperatures. The same pellet/crystal was measured in both experiments.

3.3 Results

The measured hysteresis curves show clear QTM steps which can be labelled by the conventional resonance numbering system, indicated in figure 3.1. Relaxation associated with the resonance condition from a single energy eigenstate (i.e. tunneling through a single resonant pair of levels) are not discernible due to the broadening present at these temperatures. At 2 K, the equilibrium Boltzmann populations of the ground state and first excited state at ≈ 0.45 T (the k = 1 resonance) are estimated to be about 99.4 % and 0.4%, respectively, for this sample. Generally, tunneling rates increase dramatically for eigenstates closer to the top of the potential barrier U_{eff} [10], and as such the magnitudes of the resonances increase with temperature as higher energy eigenstates are populated. This implies that, at these temperatures, we should expect significant relaxation via tunneling through at least some of the excited states.

As a function of pressure, the hysteresis data outlined here shows resonant features that tend to increase in magnitude with greater application of pressure (see figure 3.2). Interestingly, divergent trends are seen in the resonant field about which the QTM occurs between different applications of pressure, with shifts away from zero field in the parallel configuration and towards lower fields in the perpendicular. The sequences of pressures employed in both the parallel and perpendicular configurations imply no significant permanent deformation of the sample given that the data acquired

after a previous higher pressure appears to obey the general trend (see the inset in the right plot of figure 3.2).

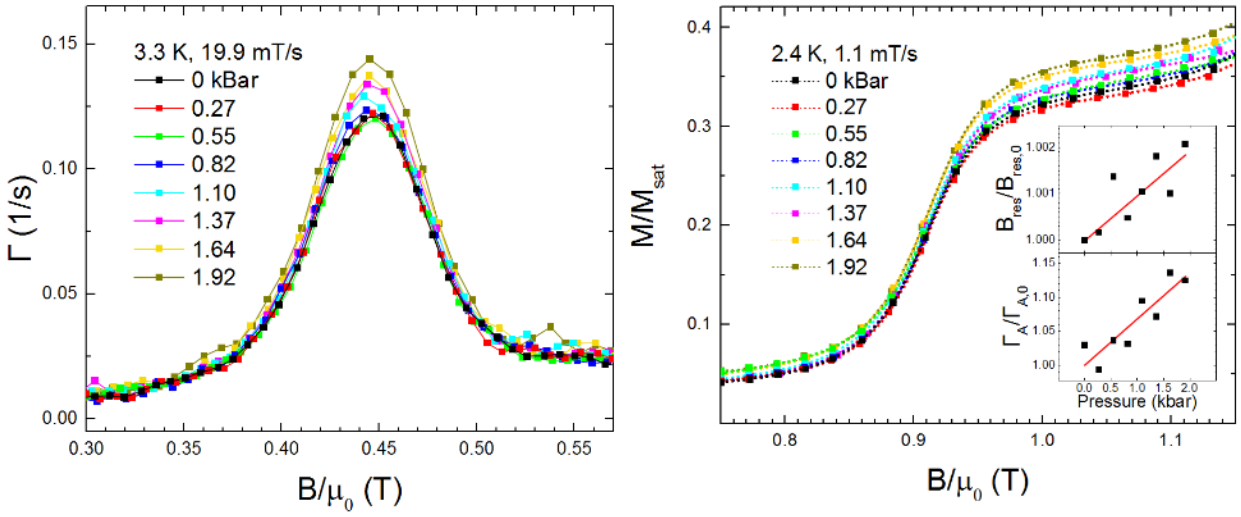

Figure 3.2 - (left) Extracted relaxation rate data about the k = 0 resonance acquired at 3.3 K with a sweep rate of 19.9 mT/s. (right) Sections of normalized magnetization data about the k = 2 resonance acquired at 2.4 K with a sweep rate of 1.1 mT/s. The dotted lines are fits to the data. The square marks represent only 2% of the actual data points, with the remainder hidden here for visual clarity.

3.4 Methods of Analysis

In order to extract meaningful estimates for how the various resonances are changing as a function of pressure, a non-linear regression curve fitting was employed using MATLAB. The objective of the fitting was to interpret the resonant spin relaxation using a Lorentzian/Gaussian linewidth model. Our data is collected as the magnetization of the sample, which, unlike traditional spectroscopic absorption/transmission data, represents a hysteretic property that can reach saturated configurations. But the information we ultimately want to extract from this data, the likelihood that an isolated spin in a metastable state will tunnel, ideally cares nothing about the overall state of the sample. This means that either our raw data had to be recast into some non-hysteretic form for appropriate fitting with the desired linewidth model or we needed a model (a fitting function) which incorporates the state of the system. As outlined below, we find that working in either framework produces similar results, but that different experimental conditions sometimes demand the use of a particular method. It is also worth noting here

that, prior to fitting, a correction $B/\mu_0 = H - DPF*M$ was made to account for the contribution of internal dipole fields to the effective field as seen by the spins [11], with a value of DPF = 22.5 mT used here for a fully magnetized sample.

The "absolute" spin relaxation rate Γ is related to the normalized time derivative of the magnetization dM/dt by

$$\Gamma \equiv \frac{1}{M - M_{eq}} \frac{dM}{dt} \tag{3.1}$$

where M represents the instantaneous magnetization and M_{eq} the magnetization at equilibrium. The relaxation rate Γ can reasonably be expected to follow convoluted lineshapes of the levels involved in tunneling and might then be expected to behave approximately as a Lorentzian or Gaussian function [12]. To wit,

$$\frac{\dot{M}}{M - M_{eq}} = \mathrm{f(B)} \tag{3.2}$$

where f(B) is the lineshape function associated with the tunnel resonance. As mentioned above, equations (3.1) and (3.2) hint at two different algorithms – either to treat the data and fit using a linewidth shape function or to derive a function which can be fit to the "raw" magnetization data while obeying equation (3.2). An approach to the latter case can be made if the equilibrium magnetization M_{eq} is assumed to be equal to the saturation magnetization of the sample M_{sat}, a condition which is approximately true far enough from zero field (at 3.3 K and HZ = 0.5 T, $M_{eq} > 0.96\ M_{sat}$). With this assumption, it is possible to solve equation (3.2) for M if f(B) is either a Lorentzian or Gaussian. Solving with a normalized Lorentzian or Gaussian (assuming that $M_{sat} = 1$ and that $M = 0$ initially) gives the equations for L and G respectively:

$$\mathrm{G}[x] = 1 - e^{-\Gamma_A(\frac{1}{2}+\frac{1}{2}\mathrm{Erf}[\frac{x-x_0}{\sqrt{2}W}])} \tag{3.3}$$

$$\mathrm{L}[x] = 1 - e^{-\Gamma_A(\frac{1}{2}+\frac{1}{\pi}\mathrm{ArcTan}[\frac{2(x-x_0)}{W}])} \tag{3.4}$$

where Γ_A is the amplitude (and technically incorporates a sweep rate, making the variable dimensionless) of the associated Lorentzian/Gaussian, W is the width, and $x_0 = B_{res}$ the center of the resonance. These solutions also provide us with a means to express the probability of a resonance with the equation:

$$P = 1 - e^{-\Gamma_A} \tag{3.5}$$

which is equivalent to the normalized change in magnetization across the step. Ultimately, we found the best fitting from employing the analog of a "pseudo-Voigt profile" style function [13] (a true Voigt profile is too computationally heavy for the number of calculations required in our analysis) consisting of a linear combination (with two coefficients that sum to unity) of the two independent solutions to equation (3.2), although such a combination is generally only an approximate solution to that equation. Applied to normalized magnetization data, this fit can yield estimates for amplitude, resonant field center, and linewidth.

For steps occurring where M_{eq} deviates significantly from the saturation value, the data was transformed point-by-point by dividing the time derivative by the difference between the instantaneous magnetization and the calculated equilibrium magnetization (through a Boltzmann weighted sum of the eigenstates and their magnetization, assuming no mixing), i.e. by transforming the data according to the left hand side of equation (3.2). The data was then fit using a pseudo-Voigt profile constructed as a linear combination of Gaussian and Lorentzian linewidth functions. This method was eschewed when possible in order to avoid the potential for additional uncertainty introduced in transforming the data (due to scaling by $(1 - M_{eq})^{-1}$, a factor dependent upon our normalization process and which grows large as the

magnetization data approaches saturation), although we found that both methods ultimately produced consistent estimates when applied to the same data.

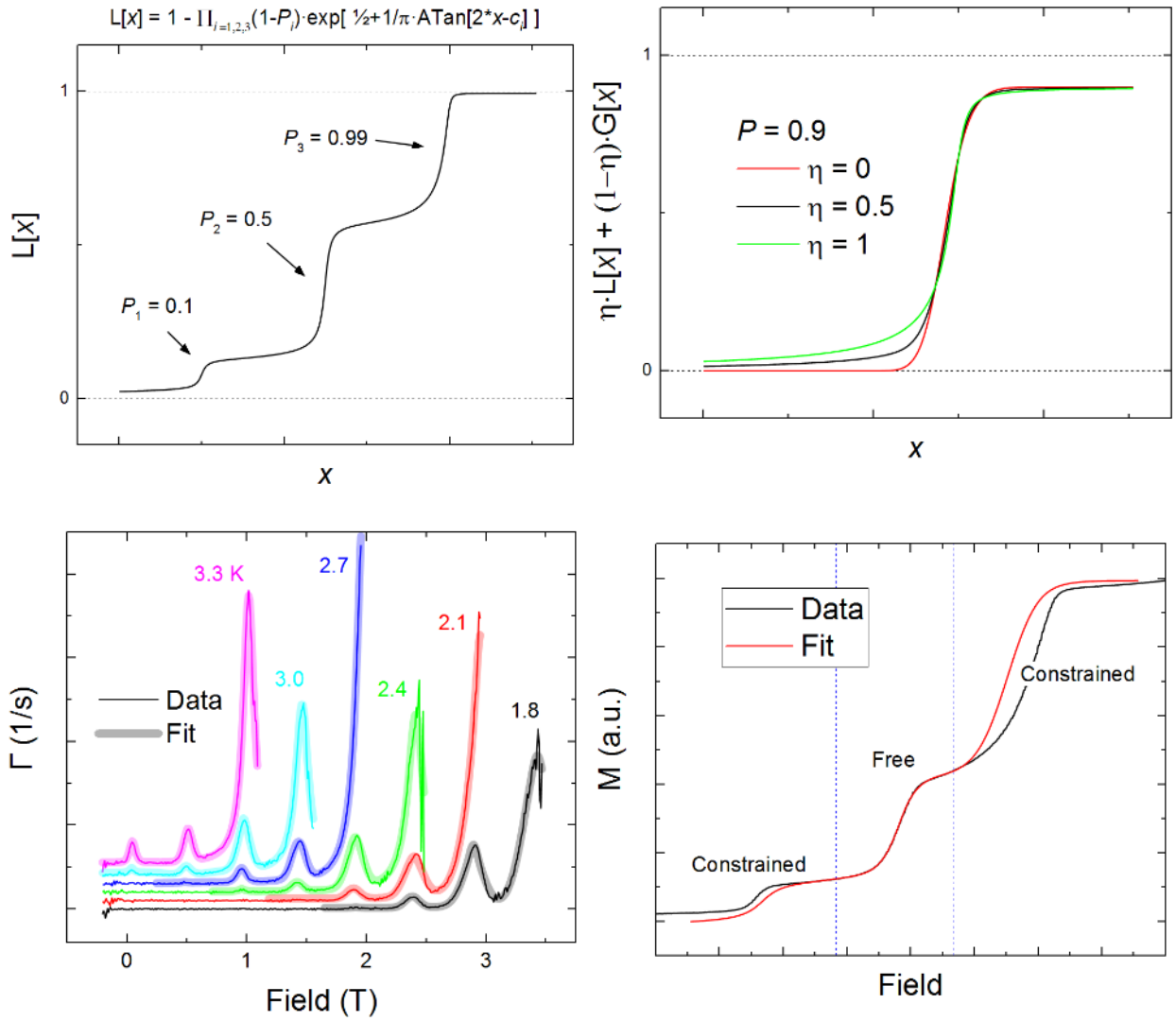

Figure 3.3 – Details of the functions fit to the normalized magnetization and extracted relaxation rate data. (Top left) Plot of several sequential Lorentzian (η = 1) fit functions with different probabilities. Note that in order to model successive resonances in this way, the function involves a product Π over the different components. (Top right) Examples of different fit functions with identical amplitudes, widths, and center positions but different Lorentzian/Gaussian factors η. The black line represents equal contributions from each type. (Bottom left) Experimental data (expressed as the relaxation rate) plotted with pseudo-Voigt fits composed of traditional Lorentzian/Gaussian functions. (Bottom right) Plot of experimental data (black line) and fit (red) outlining the method of fitting data. Here, the resonance step between the two blue dashed lines is the "target" which is fit with free parameters for amplitude, width and center, whereas functions representing steps on either side are fit with constraints in order to maximize the quality of the fit to the target step.

It is important to note that at the temperatures explored here, it is impossible to neatly separate the steps and all of the observed relaxation to one resonance or the other, as relaxation continues in regions between the steepest relaxation, albeit more slowly. The fitting was performed with this in mind by allowing the possibility of overlap between neighboring fit functions. Figure 3.3 outlines the method employed. A range of data (spanning ~4500 Oe) centered about the "target" step was selected to which three functions were fit, two of which represented contributions from resonances on either side of the target step. The function fit to the target step contained free parameters for the resonance amplitude, width, and center, whereas the functions for the neighboring steps were constrained. In order to more accurately represent uncertainties in the qualities of interest (i.e. those of the target step) and reduce the effects of erroneous attractors, fitting with each of the three functions was performed separately and incrementally, such that the parameters of the other two functions were held fixed while regression was performed for a limited number of iterations *n* before one of the other two functions was unlocked and the process repeated with the other two held fixed. This process was repeated many times with the number of regression iterations *n* decreasing over time and until the parameter estimates reached stable values.

Once estimates for the various linewidth parameters were extracted, we focused our attention on the quantity $\delta\Gamma_A/\Gamma_A \equiv (\Gamma_A(P) - \Gamma_A(0)) / \Gamma_A(0)$, i.e. the fractional change in Γ_A as a function of pressure. By looking at this quantity, we can more easily compare data from the same resonance acquired under different conditions such as sweep rate and temperature. Analysis of the resonant field center B_{res} estimates also examined the analogous quantity $\delta B_{res}/B_{res} = (B_{res}(P) - B_{res}(0)) / B_{res}(0)$.

Some of the extracted values for parameters Γ_A and B_{res} are shown in the inset of figure 3.3, plotted as a function of pressure. The equivalent estimates for the resonance widths show no clear trend and/or large error bars, and as such we choose to omit their analysis. Generally, we find that in instances where the pressure was applied parallel to the easy Z axis of the sample, the resonances became noticeably larger and shifted towards higher field as the pressure was increased. In the case of **T**

perpendicular to the easy axis, the magnitudes again increased, but shifted towards lower field with increasing pressure. Linear fits were made to the pressure dependence for each set of data indexed by step k, temperature, sweep rate, and direction of application of pressure. The slopes of the linear fits were extracted and normalized by the zero-pressure intercept to generate $\delta\Gamma_A$ and δB_{res}. Figure 3.4 shows the collected data for these two measures, delineated by the resonance label k.

To summarize, we find small increases ($\lesssim$10%) in the extracted resonance magnitudes for the equivalent of 1 kBar of uniaxial pressure applied along or perpendicular to the sample's easy axis in nearly every case examined. But we find differing trends in the resonance positions, with smaller shifts ($\lesssim$1%) towards higher field for parallel pressure and the opposite in the case of perpendicular.

3.5 Analysis & Interpretation

To understand the observed pressure dependence, we calculated how changes to different anisotropy parameters in the Spin Hamiltonian would affect the magnetization. We considered axial terms up to sixth order (DS_z^2, AS_z^4, FS_z^6) and the rhombic $B_2^2(S_+^2 + S_-^2)/2$ and tetragonal $B_4^4(S_+^4 + S_-^4)/2$ transverse parameters. In general, small changes in the axial parameters will act to shift eigenstates up or down in energy, affecting their Boltzmann population for a given temperature, and changing the resonant tunneling fields at which levels in opposite wells cross. In contrast, tuning the transverse terms can result in pronounced changes in the expected tunneling rate while leaving the resonant fields largely unchanged.

We focus on resonances k = 1, 2, 3, and 4, for which we have data at several temperatures in both the parallel and perpendicular cases. Using the ambient-pressure values for the anisotropy parameters determined previously for a similar high-symmetry Mn_{12} molecule [14], we estimate level crossings consistent with the experimental data.

For initial characterization of the parallel pressure results, we performed regression fitting using a Hamiltonian restricted to axial components:

$$H = DS_Z{}^2 + AS_Z{}^4 + FS_Z{}^6 - g\mu_B\vec{S}\cdot\vec{B}. \quad (3.6)$$

Except for transverse elements in an applied field, this Hamiltonian contains no terms which would permit tunneling. The fitting methodology outlined below uses this equation to calculate the energies of the eigenstates, while fits to experimental data are employed in order to estimate the tunneling rates. Essentially, the Hamiltonian serves to calculate the resonant fields and Boltzmann populations of the levels. We assume that substantial tunneling takes place via no more than two pairs of eigenstates for a given value of *k*, a paradigm we refer to as a "two-state" approximation. We choose levels that match closely with observed resonance positions and describe the total transition rate as a Boltzmann weighted linear sum of contributions from the two levels, i.e. $\Gamma_{Tot} = \Gamma_1 * exp(-E_1/k_BT) + \Gamma_2 * exp(-E_2/k_BT)$. These levels m_1, m_2 were, as labelled by the off-resonant S_Z spin number:

Table 3.1 – List of initial states used in modelling tunneling in the two state approximation.

Resonance *k*	m_1, m_2
1	-6, -5
2	-6, -5
3	-7, -6
4	-8, -7

Then, by taking the amplitudes Γ_1 and Γ_2 that characterize the total relaxation through each of the two resonance conditions to be constant, we could fit changes in the resonance magnitudes to alterations of the Boltzmann populations induced by changes in *D* and *A*. The sixth order constant *F* was held constant in an effort to limit the number of free parameters and because good agreement could be found without letting it vary. Fitting the temperature dependence of the ambient values of the amplitude Γ_A generated initial estimates for Γ_1 and Γ_2. Simultaneously, we fit the temperature dependence of the ambient B_{res} data to an expression that approximates the resonant field as a sum of the two individual resonant fields of the

contributing levels, weighted by their Boltzmann populations and transition rates Γ_1 and Γ_2, *i.e.* $B_{Tot} = B_1{*}\Gamma_1{*}exp(-E_1/k_BT) + B_2{*}\Gamma_2{*}exp(-E_2/k_BT)$. In this way we could produce estimates for changes in the Hamiltonian parameters by fitting to the data as a function of pressure and temperature and letting D and A vary. The results of this fitting give values of $\delta D/D = (D_{1kBar} - D_{Ambient}) / D = 0.58\%$/kbar and $\delta A/A = -5.76\%$/kbar. These changes act to shift all resonances towards higher field while lowering the energy difference between transitions out of excited and ground states, resulting in greater populations in states from which spins are more likely to tunnel (generally increasing the contributions to the overall rate from every energy level except the ground state) while still increasing the magnitude of the potential well/barrier U_{eff}.

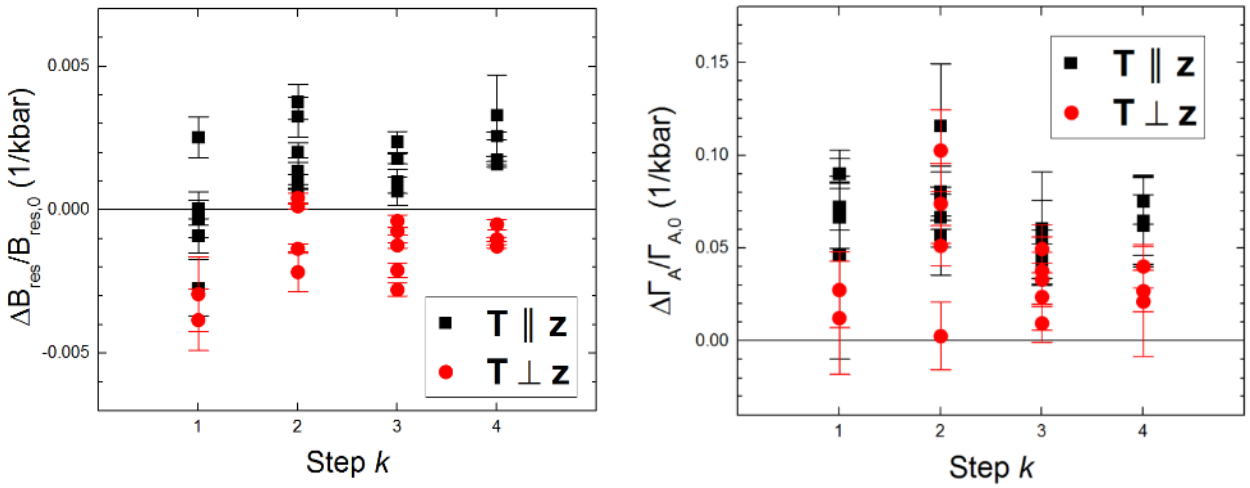

Figure 3.4 - Pressure dependence of the resonance magnitudes extracted from linear fits to the magnitude data, with the plot point style differentiated for the two different pressure configurations. (b) Pressure dependence of the extracted resonance positions.

To analyze the data more fully, we employed a master equation approach which calculates the relaxation rate Γ from terms describing spin-phonon interactions [15-17], which takes the form

$$\frac{dp_i}{dt} = \sum_{\substack{j=1 \\ i \neq j}}^{21} -\left(\gamma_{ij}^{(1)} + \gamma_{ij}^{(2)}\right) p_i + \left(\gamma_{ji}^{(1)} + \gamma_{ji}^{(2)}\right) p_j. \tag{3.7}$$

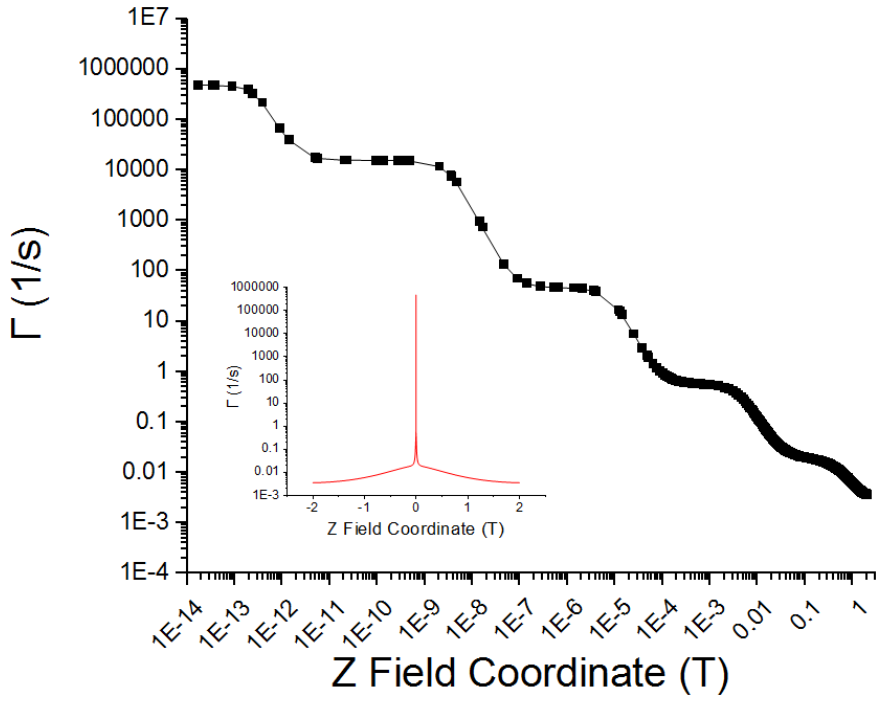

Figure 3.5 – Log/Log plot of simulated relaxation showing the contributions of various transitions about the $k = 0$ resonance in the model outlined below. The solid line is a linear interpolation between points. The inset shows the same data in a Log/Linear representation.

In this so-called secular approximation, eigenstates were calculated in the S_Z basis using a Hamiltonian which included second and fourth order transverse anisotropy terms (see equation (3.11) below), with only diagonal elements in the density matrix being considered; this conserves computational resources but reduces the applicability of the model near the resonance condition where off-diagonal elements might play an important role. Nonetheless, this model allows us to discriminate between different scenarios of variations in the anisotropy parameters. The first and second order spin-phonon transition rates are given by [18,19]

$$\gamma_{ij}^{(1)} = \frac{D^2}{24\,\pi\,\rho\,c_s^5\hbar^4}\left|s_{ij}^{(1)}\right|^2 \Delta_{ij}^3 N(\Delta_{ij}) \tag{3.8}$$

$$\gamma_{ij}^{(2)} = \frac{D^2}{36\,\pi\,\rho\,c_s^5\hbar^4}\left|s_{ij}^{(2)}\right|^2 \Delta_{ij}^3 N(\Delta_{ij}) \tag{3.9}$$

where D is the same parameter represented in Eq. (8), ρ is the mass density of the sample, c_S is the speed of sound in the sample, $s_{ij}^{(1)} = \langle i|\{S_x+S_y\}|j\rangle$, $s_{ij}^{(2)} = \langle i|\{S_x^2+S_y^2\}|j\rangle$, Δ_{ij} is the energy difference between levels i and j, and $N(\Delta_{ij}) = 1/(\exp(-\Delta_{ij}/k_BT)-1)$ is the phonon thermal distribution function. The rate Γ_{sim} is then taken as the slowest non-zero element of the matrix generated from equation (3.7). In our simulation, we assumed a constant field H_x = 22.5 mT in order to represent the effects of internal transverse fields that have been demonstrated to play a significant role in the magnitudes of QTM resonances [20].

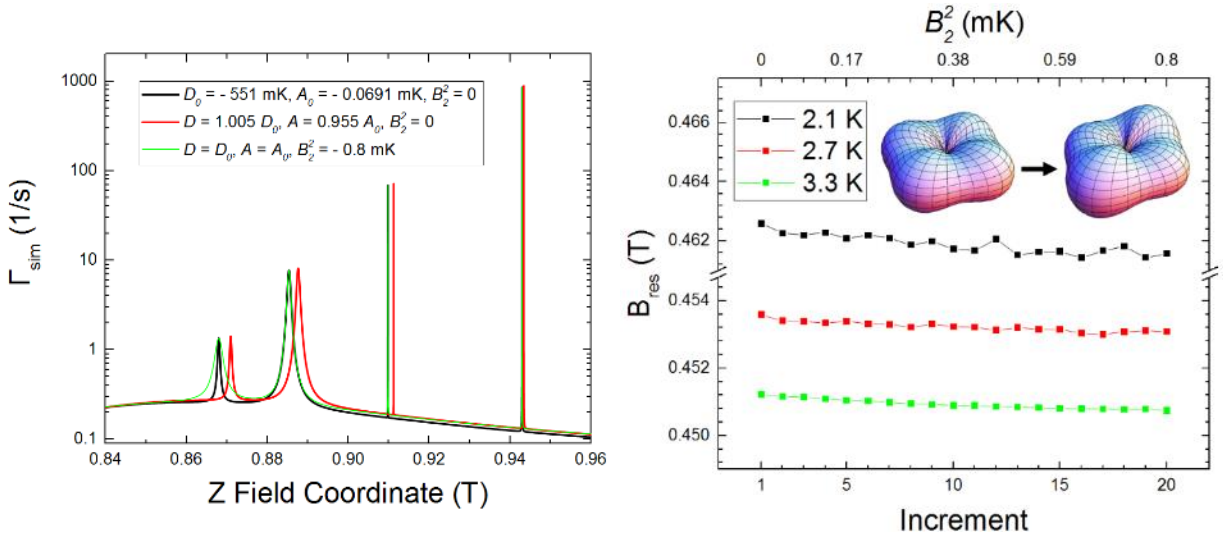

Figure 3.6 - Panel (a) shows the result of numerical simulation of the relaxation rate using the "ambient" anisotropy parameters as well as the altered values for the parallel and perpendicular cases. (b) Shows the estimated resonance position B_{res} extracted from the simulations, with the inset illustrating an exaggerated distortion of a tetragonal symmetry as induced by the introduction of a B_2^2 term.

In order to extract estimates for resonant field from calculations of Γ_{sim} we used a weighted integral over a field range centered around the resonances of interest (such that it included all "peaks" associated with a given resonance number k) as outlined by the equation

$$B_{res,sim} = \frac{\int_{B_i}^{B_f} \Gamma(x)\, x\, dx}{\int_{B_i}^{B_f} x\, dx} \tag{3.10}$$

in which the bounds B_i and B_f about a resonance k are 0.45*k ± 0.15 T. The spin-phonon rate simulation produces data in which Γ_{sim} is small except near a resonance condition, and as such equation (3.10) is essentially an average of the peaks' abscissa weighted by their area. The amplitude $\Gamma_{A,sim}$ of a resonance

was simply taken as the area under the peaks for the same bounds. To conserve computational resources, the contributions from specific resonances were omitted when we could safely assume they were small, i.e. in the case of resonances closest to the ground state which were calculated to occur at fields far from the relaxation observed in the hysteresis steps.

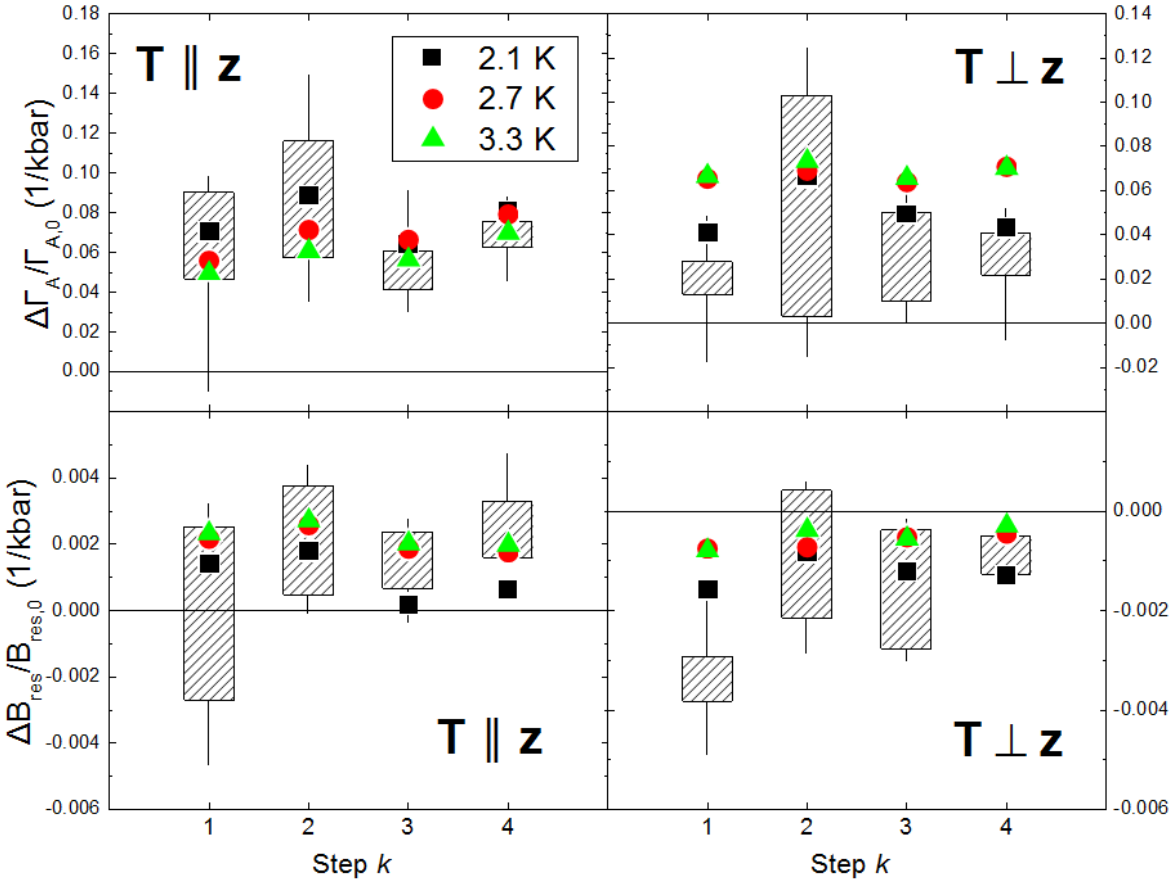

Figure 3.7 - Comparison calculations (black/red/green points) with the results of pressure dependence outlined in Fig. 4 plotted as patterned grey boxes, where the upper and lower extents are defined by the highest and lowest values at that step and the whisker lines are the error bars for those points.

In this calculation, we include terms for transverse rhombic and tetragonal anisotropy into our Hamiltonian, which can be written

$$H = DS_Z^{\,2} + AS_Z^{\,4} + FS_Z^{\,6} + B_2^2O_2^2 + B_4^4O_4^4 + B_6^4O_6^4 - g\mu_B\vec{S}\cdot\vec{B} \qquad (3.11)$$

where $O_2^2 = (S_+^{\,2} + S_-^{\,2})/2$, $O_4^4 = (S_+^{\,4} + S_-^{\,4})/2$, and $O_6^4 = [11S_z^{\,2} - S(S+1) - 38,(S_+^{\,4} + S_-^{\,4})]$ are Stevens operators and the coefficients have the "ambient" values D = -0.557 K, A = -6.36*10^{-4} K, F = -2.31*10^{-6} K, B_2^2 = 0,

$B_4^4 = 2.88*10^{-5}$ K, and $B_6^4 = -1.44*10^{-7}$ K [14]. We include the B_2^2 term here as we use it to model a physical distortion along an axis in the transverse plane. Inserting the values for $\delta D/D$ and $\delta A/A$ extracted from the regression fitting scheme into our spin-phonon model for Γ_{sim} produces changes in the calculated amplitudes and resonant fields similar to those from the two-state approximation outlined above. We take it as a positive sign of the applicability of the two models that they both indicate similar behaviors due to changes in these anisotropy parameters. Unlike the two-state approximation, we are unable to use a regression scheme to fit our master equation approach to the data, in part because of the number of calculations required to generate a set of simulated relaxation data. As can be seen in figure 3.5, a great deal of precision is required to accurately sample the resonance peaks, and reducing the model accuracy (say, be increasing the minimum increment) can lead to drastically different estimates from the weighted averaging as the resonance positions shift. In light of this, the method we followed was to perform the simulation for a limited range of anisotropy parameters, varying D and A linearly and simultaneously or introducing a value for the rhombic anisotropy element. Figure 3.6 shows sections of simulation data centered about the $k = 2$ resonance position generated using these modified values for the anisotropy parameters, as well as simulations using the ambient values and for a set of parameters that includes the introduction of a rhombic term $|B_2^2| < 1$ mK oriented along one of the hard axes of the molecular anisotropy. The parameters were varied from their initial to final values in 20 increments. Contrary to the effects produced using the two-state parallel pressure estimates, the introduction of a rhombic term "opens" certain resonances while leaving the resonance positions largely unchanged. The most dramatic effects appear at positions corresponding to excited states near the top of the barrier, which are always closer to zero field than lower excited states (with the same resonance k) due to opposite signs between D and A. This implies that an "average" over these resonances would shift towards lower field as the rhombic component is increased, a conclusion borne out by the estimates of $B_{res,sim}$ as shown in figure 3.6. In that plot, we have shown the results of three simulations conducted assuming a range of temperature equal to that explored in our measurements. As expected in a system with negative fourth and sixth order

axial anisotropy constants A and F, the increase in temperature lowers the resonant field as a greater portion of the tunneling takes place through excited states.

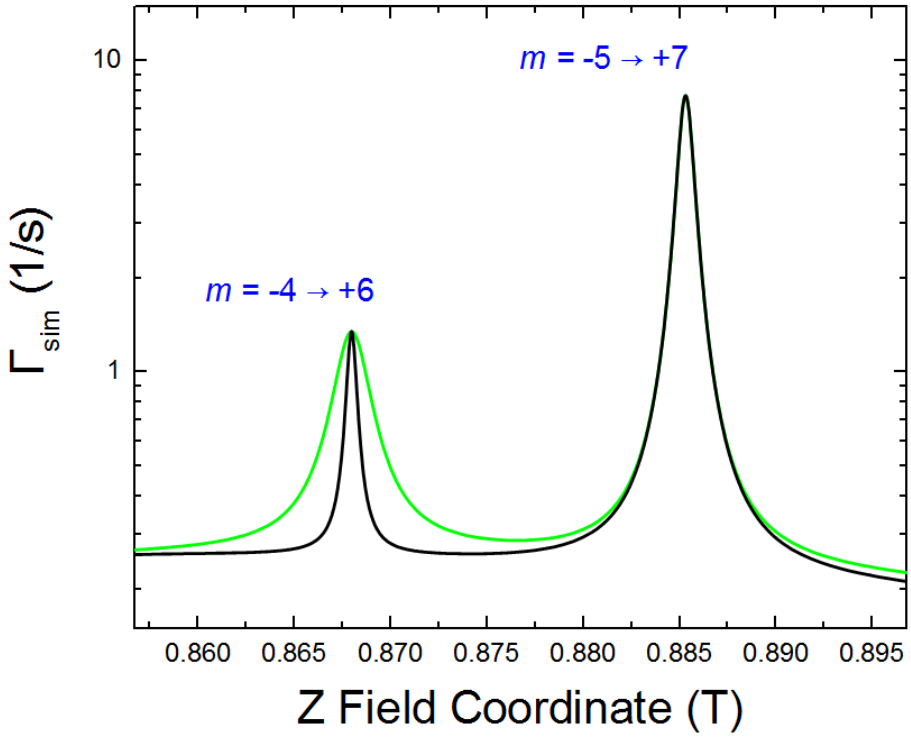

Figure 3.8 – Detail of the calculated relaxation rate for ambient conditions (black) and the perpendicular pressure change per kbar (green) for two resonances at the $k = 2$ step. The data is also shown in figure 3.6. The peak no the left represents a transition where the change in spin is $\Delta S = 10$, whereas the peak on the right is $\Delta S = 10$.

Values for the dependence of $B_{res,sim}$ and $\Gamma_{A,sim}$ were calculated as the parameters δD and δA or B_2^2 were incrementally increased from zero through their estimated values for three temperatures, 2.1 K, 2.7 K, and 3.3 K. This generated data all qualitatively similar to that shown in figure 3.6, with some scatter due to the discrete nature of the calculation. Lines were fit to these calculations and slopes extracted in order to determine the dependence of $B_{res,sim}$ and $\Gamma_{A,sim}$ upon D and A or B_2^2. Fig. 6 shows the estimated changes in the amplitude and center positions for δD = 0.58%/kbar and δA = -5.76%/kbar (in the case of $\mathbf{T} \parallel \mathbf{Z}$) or B_2^2 = 0.63 mK/kbar (for $\mathbf{T} \perp \mathbf{Z}$). In all cases, the simulations show good agreement with the trends observed in the experimental data, matching the directions of the shifts and the relative sizes of the changes in magnitude to resonant field.

3.6 Discussion & Conclusions

The estimates produced by the fitting to the parallel data represent a reduction in the fourth order anisotropy *A* and a slight increase in the second order anisotropy *D.* Even though the net change in the position of the calculated resonances is toward higher field, representing an increase in the overall potential barrier U_{eff}, our simulations show that by collapsing the difference in field between transitions out of the ground and excited states, the net relaxation at a given step *k* should be expected to grow as the Boltzmann population of the higher-lying states (through which tunneling is more likely) is increased. In essence, we see that the "tunnel current" is more sensitive to the greater number of transitions out of higher-lying states than the inhibited rate caused by a larger potential barrier, at least in the modifications to the anisotropy outlined here. We speculate that this alteration in *A* may be due to changes in the inter-ion exchange coupling *J* [20], possibly as a result of shifts in relative positions of ions within the molecular core.

Figure 3.8 details some of the data shown in figure 3.6, illustrating the effect that an introduction of a rhombic term has on the simulated relaxation rate for different resonances at the same step *k.* Resonances which represent a change in spin ΔS that is an integer multiple of the dominant transverse symmetry (in this case four, as the molecule is tetragonally symmetric) are largely unaffected, as can be seen in the right hand peak within the plot, associated with change in spin $\Delta S = 12$. However, transitions which differ from such an integer multiple of the symmetry by $\Delta S = \pm 2$, such as the peak on the left, show large increases in associated relaxation rates as the introduction of rhombic symmetry opens up a new pathway to tunnel. Transitions occurring nearer the top of the potential barrier (i.e. where ΔS is less) appear to show larger increases in the calculated relaxation rate, as they require fewer applications of the rhombic operator in order to mix the states involved.

We have demonstrated that uniaxial pressure applied to a crystalline sample can produce distinct behaviors in the magnetization behavior of a SMM, and that equivalent behaviors can be reproduced in

simulations of the relaxation rate incorporating molecular anisotropy parameters. Given the expected relationship between the strength of the intramolecular exchange coupling J and the fourth order correction to the uniaxial anisotropy [20], we find it noteworthy that our simulations produce a larger change in the magnitude of A than the second order term D. We also find it interesting that a simple rhombic distortion is enough to reproduce the observed behaviors in simulations. Indeed, if these interpretations are accurate representations of the conditions experienced by the molecules, it is tempting to imagine the possibilities in greater applications of uniaxial pressure.

References

[1] G. Redler, C. Lampropoulos, S. Datta, C. Koo, T. C. Stamatatos, N. E. Chakov, G. Christou, and S. Hill, Crystal lattice desolvation effects on the magnetic quantum tunneling of single-molecule magnets, Phys. Rev. B **80**, 094408 (2009)

[2] S. Hill, Magnetization tunneling in high-symmetry Mn12 single-molecule magnets, Polyhedron **64**, 128-135 (2013)

[3] Y. Suzuki, K. Takeda, K. Awaga, Enhancement of Jahn-Teller isomerism in Mn12Ac under high quasi-hydrostatic pressure Phys Rev B, 67, 132402 (2003)

[4] A. Sieber, G. Chaboussant, R. Bircher, C. Boskovic, H. U. Guedel, G. Christou, H. Mutka, Pressure Dependence of the Magnetic Anisotropy in the Single-Molecule Magnet [Mn4O3Br(OAc)3(dbm)3] Phys. Rev. B 70, 172413 (2004)

[5] A. Sieber, D. Foguet-Albiol, O. Waldmann, S. T. Ochsenbein, G. Carver, H. Mutka, F. Fernandez-Alonso, M. Mezouar, H. P. Weber, G. Christou, and H. U. Güdel, Pressure Dependence of the Exchange Interaction in the Dimeric Single-Molecule Magnet [Mn4O3Cl(O2CEt)3(py)3]2 from Inelastic Neutron Scattering Phys. Rev. B 74, 024405 (2006)

[6] R. Bircher, G. Chaboussant, C. Dobe, H. U. Güdel, S. T. Ochsenbein, A. Sieber and O. Waldmann, Single-Molecule Magnets Under Pressure Adv. Funct. Mater. 2006, 16, 209–220 (2006)

[7] A. Prescimone, J. C. Milios, S. Moggach, J. E. Warren, A. R. Lennie, J. Sanchez-Benitez, K. Kamenev, R. Bircher, M. Murrie, S. Parsons, E. K. Brechin, [Mn6] Under Pressure: a Combined Crystallographic and Magnetic Study Angew. Chem. Int. Ed, 47: 2828–2831 (2008)

[8] Campos C. E., Brooks J. S., Vanbentum P. J. M,.Perenboom J., Rook J., Klepper S. J. and Tokumoto M., Rev. Sci. Instrum., 66 (1995) 1061.

[9] J. H. Atkinson, K. Park, C. C. Beedle, D. N. Hendrickson, Y. Myasoedov, E. Zeldov and J. R. Friedman, The effect of uniaxial pressure on the magnetic anisotropy of the Mn12-Ac single molecule-magnet EPL 102, 47008 (2013)

[10] J. R. Friedman, Resonant Magnetization Tunneling in Molecular Magnets, in Exploring the Quantum/Classical Frontier: Recent Advances in Macroscopic and Mesoscopic Quantum Phenomena, J. R. Friedman and S. Han, eds. (Nova Science, Huntington, NY, 2003).

[11] McHugh S., Jaafar R., Sarachik M. P., Myasoedov Y., Shtrikman H., Zeldov E., Bagai R. and Christou G., Phys. Rev. B, 79 (2009) 052404.

[12] Resonant Magnetization Tunneling in Molecular Magnets, J. R. Friedman, in Exploring the Quantum/Classical Frontier: Recent Advances in Macroscopic and Mesoscopic Quantum Phenomena, J. R. Friedman and S. Han, eds. (Nova Science, Huntington, NY, 2003).

[13] Wertheim, G. K. and Butler, M. A. and West, K. W. and Buchanan, D. N. E. (1974). "Determination of the Gaussian and Lorentzian content of experimental line shapes". Review of Scientific Instruments 45 (11): 1369–1371

[14] Anne-Laure Barra, Andrea Caneschi, Andrea Cornia, Dante Gatteschi, Lapo Gorini, Leo-Philipp Heiniger, Roberta Sessoli, and Lorenzo Sorace, The Origin of Transverse Anisotropy in Axially Symmetric Single Molecule Magnets, J. Am. Chem. Soc., 2007, 129 (35), pp 10754–10762

[15] M. Bal, J. R. Friedman, S. Shah, D. N. Hendrickson, N. Avraham, Y. Myasoedov, H. Shtrikman and E. Zeldov, Photon-Induced Magnetization Changes in Single-Molecule Magnets, J. Appl. Phys., 99, 08D103 (2006).

[16] M. Bal, J. R. Friedman, W. Chen, M. T. Tuominen, C. C. Beedle, E. M. Rumberger and D. N. Hendrickson, Radiation- and Phonon-Bottleneck-Induced Tunneling in the Fe8 Single-Molecule Magnet EPL, 82, 17005 (2008).

[17] S. T. Adams, E. H. da Silva Neto, S. Datta, J. F. Ware, C. Lampropoulos, G. Christou, Y. Myaesoedov, E. Zeldov and Jonathan R. Friedman, Geometric-phase interference in a Mn12 single-molecule magnet with four-fold rotational symmetry, Phys. Rev. Lett. 110, 087205 (2013).

[18] D. A. Garanin and E. M. Chudnovsky, Thermally activated resonant magnetization tunneling in molecular magnets: Mn12Ac and others, Phys. Rev. B 56, 11102 (1997).

[19] M. N. Leuenberger and D. Loss, Spin relaxation in Mn12-acetate Europhys. Lett. 46, 692 (1999)

[20] James H. Atkinson, Ross Inglis, Enrique del Barco, and Euan K. Brechin, Three-Leaf Quantum Interference Clovers in a Trigonal Single-Molecule Magnet Phys. Rev. Lett. 113, 087201 (2014)

[21] Stephen Hill, Saiti Datta, Junjie Liu, Ross Inglis, Constantinos J. Milios, Patrick L. Feng, John J. Henderson, Enrique del Barco, Euan K. Brechin and David N. Hendrickson, Magnetic quantum tunneling: insights from simple molecule-based magnets Dalton Trans., 2010,39, 4693-4707

CHAPTER 4: THE SPIN-PHOTON INTERACTION

The discussion in this chapter will focus on the theoretical and experimental framework underpinning two projects designed to investigate the spin-photon interaction in the weak and strong coupling regimes. Briefly, the outlines of these two experiments are:

1. To perform pulsed-microwave measurements on a SMM system at a temperature and magnetic field where several sources of decoherence are expected to be in play and the relevant eigenstates are still predominantly determined by the intrinsic molecular anisotropy.
2. Ensembles of spins within a SMM will be coherently coupled to a low number of photons within a high-finesse cavity, with vacuum fluctuations driving the coupling between the spin/photon system (the "vacuum Rabi splitting").

Our motivation for performing these experiments is to push the boundary of research into spin-photon coupling and manipulation, an important and very active area of study with important consequences for quantum computing and information storage [1-13]. As a spin system, SMMs are particularly interesting for their intrinsic anisotropy and assemblage as lattices of isolated sites. The following sections will look at the sources of decoherence in SMM system, followed by discussion of the Jayne Cumming (JC) model of an interacting spin and photon, then further details of the two experiments and the progress made towards their implementation.

4.1 Decoherence in SMMs and Weak Spin-Photon Coupling

The challenge of overcoming decoherence in SMMs is a good example of a problem that is easy to state but difficult to solve. In order to probe the coherent evolution of a spin within a sample, the rate at which outside systems sites interlope and couple to the spin must be slower than the time it takes to complete a measurement. For SMMs, the primary sources of decoherence have been identified [14] as coupling to nuclei (hyperfine fluctuations), lattice vibrations (phonons), and the oscillations of local

magnetic fields (magnons). If the system also includes coherent photons, the interacting cavity must have a sufficiently high finesse (quality factor Q) to support long excitation lifetimes. These constraints put practical bounds on the performance of external instrumentation – if the spin/photon states only survive for X seconds, your pulse-creating switches had better take less than X seconds to open and close.

In order to maximize the spin coherence time, our experiments are designed to optimize the parameters that can be tuned by the experimental apparatus. Decoherence due to dipolar and phonon couplings tend to decrease with lower temperature, with the former mechanism predicted to show a particularly strong dependence. By working with a dilution refrigerator, we can reach temperatures as low as ~ 50 mK, leading to polarization of the spin bath at small separations (~ 20 GHz) between the ground and first excited state. Generally, we can tune this transition energy (the "splitting" Δ) by changing the applied field and matching microwave stimulus. As a function of the splitting Δ, the dipolar and phonon couplings are expected to have opposing trends in spin coherence lifetimes, with dipolar effects decreasing and phonon effects increasing the decoherence rate with larger transitions energies. Nuclear dephasing is expected to decrease with larger splitting and depend on the sample-specific coupling between the nuclear and electronic wavefunctions.

An objective for our experiment in the weak coupling regime is to find a point (a temperature and transition frequency) where the confluence of these three decoherence mechanisms produces durable coherent spin states and the eigenstates are largely defined by the local ion anisotropies. We estimate that for the SMM samples of interest, for example Mn_3, these conditions might be reachable using X band frequencies at the lowest temperatures attainable by our dilution unit. For a system which lacks large ZFS transitions close to the ground state (which is true of most SMMs), it is necessary to apply transverse fields to split the degenerate zero-field states (which are approximately equal to the eigenstates $|\pm m\rangle$ of the easy-axis spin operator S_z) into heavily mixed symmetric/antisymmetric superpositions which readily couple to photons.

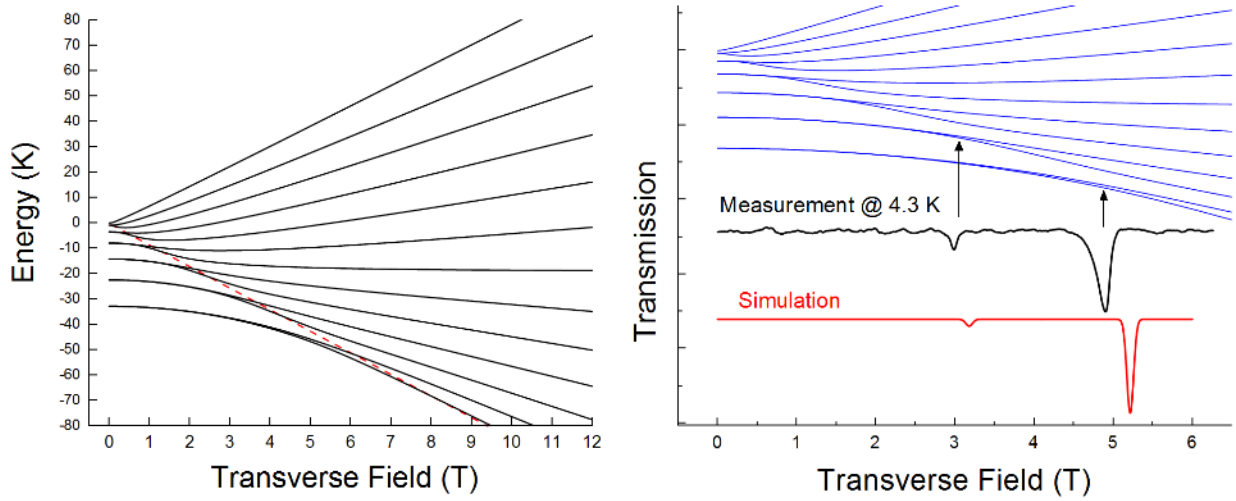

Figure 4.1 – (left) Plot of the Zeeman split energy levels of the Mn3 system discussed in Chapter 2 as a function of transverse field in the GSA approximation. The dashed red line is the approximate boundary between conditions where the ZFS dominates (the left hand side) and where the large transverse field defines a new quantization axis (right hand side). (right) Plot of measured and simulated EPR spectra from a Mn_3 sample at 4.3 K as a function of a transverse field. The arrows indicate the positions of the transitions (= 13.2 GHz) in the associated Zeeman plot above.

Figure 4.1 shows a plot of the calculated energy eigenvalues for the Mn_3 GSA Hamiltonian described in Chapter 2 as a function of transverse field. Note that for large transverse fields, the eigenvalues begin to show linear dependence on applied field (roughly delineated by the dashed red line in the plot), indicating that the easy Z axis is losing sway as the dominant quantization axis. Figure 4.1 also shows EPR data acquired at 13.2 GHz from a Mn_3 system at 4.3 K, with an applied field oriented in the hard plane. Simulation with the MATLAB *EasySpin* toolbox shows good agreement with the observed positions and amplitudes of the resonance peaks. Pulsed microwave measurements (spin-echo) have been performed on a similar Mn_3 system [15] at a frequency 230 GHz and field ≈ 9 T which leads to suppression of dipolar decoherence, resulting in T_2 times of ≈ 170 ns at 1.69 K. Under these conditions, where the temperature places an effective lower bound on the size of the splitting, the system is predominantly quantized along the applied field axis and not the intrinsic molecular easy axis. By working at lower temperatures and frequencies, we hope to sample the effect of coherent spin evolution of states heavily influenced by internal mechanisms present in SMMs.

In addition to lowering temperature, another method for reducing dipolar decoherence is to increase the distance between magnetic sites within the sample's crystalline lattice, either by physically separating the constituent molecules (say, in a solution [16-18]) or by chemically altering the makeup of sites such that some fraction are non-magnetic, creating a "buffer" of dormant molecules in between unaltered magnetic sites [19,20]. This latter approach works particularly well with compounds in which the molecular spin is sourced in a single ion (a mononuclear or "single ion" magnet) where substitution of that ion means complete removal of its magnetic properties.

It is also possible to locate transitions which are intrinsically insulated against the dipolar fields that would otherwise perturb the coherent state. These so called "sweet spots" or "atomic clock" transitions occur where the first and second order derivatives of the state energies with respect to magnetic field $\partial E/\partial B$ and $\partial^2 E/\partial B^2$ are close to zero across a span of field large enough such that a small change in the local field does not significantly alter the system, insulating the eigenstates from nearby spin flip-flop events.

4.2 Experimental techniques and apparatus for probing weak spin-photon coupling

Assuming the requisite environmental parameters (temperature, sample concentration, etc.) can be reached, the instrumentation responsible for the delivery of the microwave stimulus and acquisition of the output signal must be capable of properly initializing the spin system and reading its output signal. To this end, we have prepared a precise and sensitive apparatus for delivering microwave pulses to the sample at the necessary intensities while still resolving what may be a minute yield. The structure of our microwave pulse sequence follows standard spin echo methods in which an initial pulse (a "π-half pulse") torques the spins within the sample into the transverse plane. A second pulse (the "π pulse") inverts the orientations of the precessing spins, ideally leading to a refocusing after an equal interval of time. This method samples the spin-spin relaxation time T_2, and, under the right conditions, can exhibit Rabi oscillations.

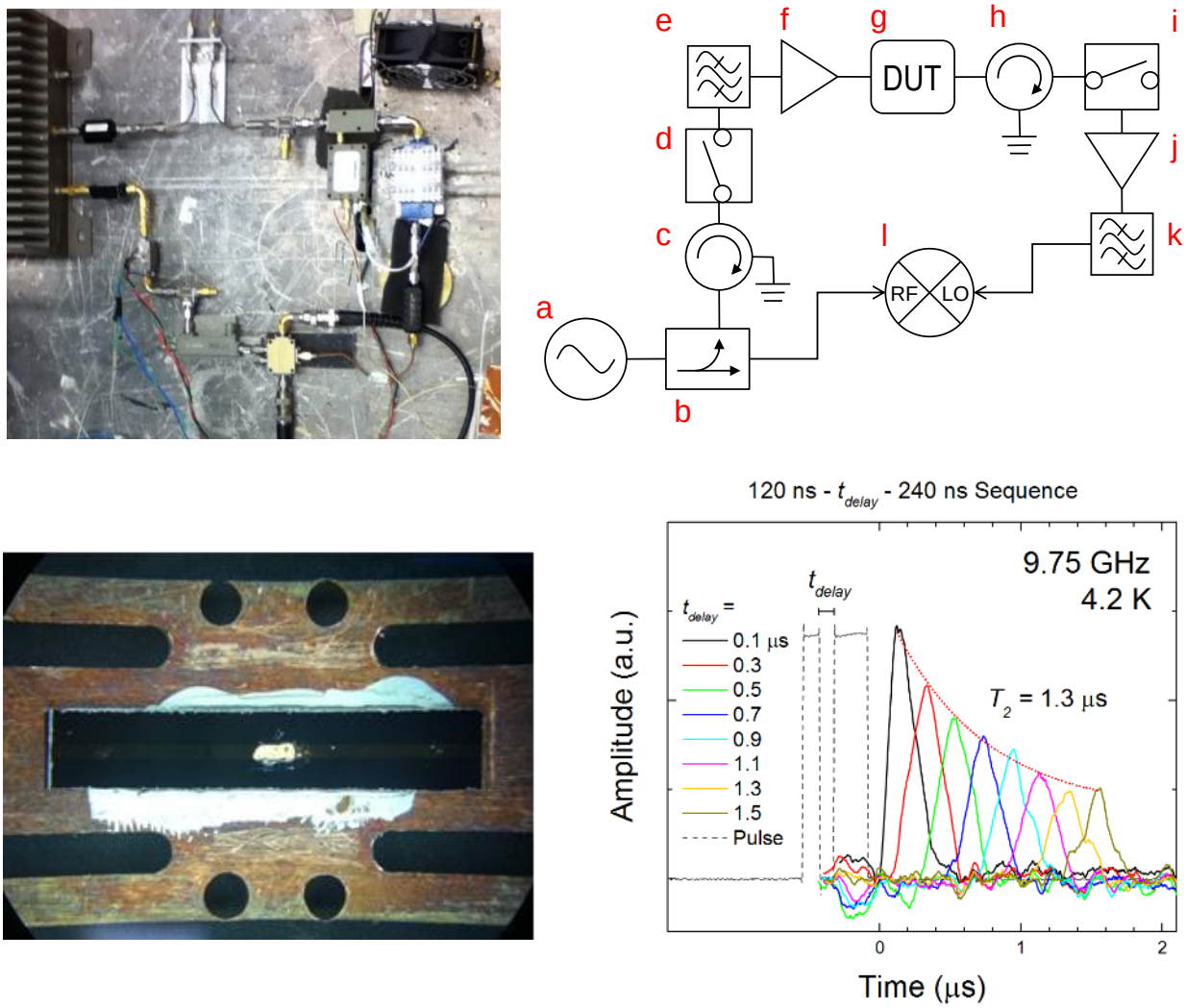

Figure 4.2 – (top left) Photograph of the pulse circuitry used to perform pulsed microwave measurements. (top right) Circuit diagram of the pulse delivery and homodyne detection instrumentation. Table 1 contains a description of the items indexed by their alphabetical labels. (bottom left) Photograph of a sample mounted on a 10 GHz Au resonator, which is in turn mounted on the bottom plate of our Cu housing box. The housing box can be mounted into our cryostat/dilution refrigerator with contacts between coaxial microwave lines and the feed lines of the device. (bottom right) Spin echo signal from a "Bruker Coal" sample at 4.3 K. The solid lines are the signal after subtraction of a background, with different colors representing a different time delay between π-half = 120 ns and π = 240 ns pulses. The dotted red line is an exponential fit to the echo peaks, extracting a spin-spin relaxation time of 1.3 µs.

Table 4.1 - Table of microwave components included in the circuit shown in Fig. 4.2

Component index	Description
a	HP 8350B Microwave Source
b	Agilent 87301D Directional Coupler, Opt 240
c	Pasternack PE8404 Circulator in Isolator Configuration
d	Miteq SPST Pin 4 – 12 GHz Switch
e	KL Microwave 2 – 18 GHz Bandpass Filter
f	Agilent 83020A RF Amplifier
g	Device Under Test (Resonator with Coal sample in Cryostat)
h	Pasternack PE8404 Circulator in Isolator Configuration
i	HP SPST 33144A Switch with HP 33190B Driver
j	CTT APM/180-2741-22 RF Amplifier
k	KL Microwave 2 – 18 GHz Bandpass Filter
l	Stellex M38UC Quadrature Mixer

The design of our pulse instrumentation is based on standard homodyne detection techniques in which a source signal is split between two paths, with one leading to the sample (the stimulus) and the other directed to the reference port on a quadrature mixer, which outputs a constant voltage when a matching frequency signal from the sample is detected. Figure 4.2 details the design of our circuit and shows a photograph of a resonant cavity with results from a spin echo measurement on a spin ½ coal sample. In the configuration shown, an HP 8350 B was used a microwave source, with its output fed into a directional coupler which splits the signal between the stimulus/reference paths. A microwave switch is used to form the stimulus pulse, with its output fed into a bandpass filter and then an amplifier. The bandpass filter reduces noise from the switch opening/closing process, a necessary step for ensuring that the sample evolves under the sole influence of the microwave pulses of the desired frequency. Circulators

are used (in isolating configurations) to limit stray noise or otherwise spurious signals from different stages of the circuit. It is critical that switching noise from the input port of the second switch (which prevents the high-amplitude pulses from damaging the amplifier which gains the signal from the sample) does not leak back into the resonant cavity.

In a spin echo measure, the pulse sequence is dictated by the transition energy of the sample and the coupling between the sample and the device. In the two-state rotating wave approximation [21], the drive frequency of the pulse must match the Larmor precessional frequency, which is equivalent to the Zeeman splitting. For a spin ½ system this frequency is given by the equation

$$f_{Larmor} = gB\mu_0/h \tag{4.1}$$

where g is the electron g-factor, B is the DC magnetic field which creates the splitting, μ_B is the Bohr magneton and h is Planck's constant. For the resonator device shown in figure 4.2 (Au on Silicon, $Q \approx 50$) we can estimate the magnetic field at the sample position with the equation [22]

$$h_{field} = \frac{\mu_0}{w}\sqrt{\frac{P\,Q}{2\,Z}} \tag{4.2}$$

where μ_0 is the magnetic permeability of the vacuum, w = 0.6 mm is the width of the device, P is the microwave power into the cavity, Q is the quality factor and Z = 50 ohms is the device impedance. The estimated power at the device used to generate the data shown in figure 4.2 was ≈ 10 mW, giving an estimate for the field at the sample of $h \approx 0.7$ mT. With this information we can estimate the duration of a "π-half" pulse with the formula

$$t_{\pi/2} = \frac{\pi}{\gamma_e\, h_{field}} \tag{4.3}$$

where γ_e is the gyromagnetic ratio of a free electron. Inserting our estimate for the device field into equation 4.3 gives a pulse time of 120 ns, a duration which produced the clear echo features shown in figure 4.2.

At this stage, we only require adequate temperature control in order to examine the coherent evolution of spins in SMM samples. With functional and optimized microwave pulse instrumentation, we expect to attain coherence times significantly longer than the stimulus/measurement cycle, allowing an investigation into the mechanisms which regulate the weak-coupling regime in SMMs. In the following section, we begin our discussion of our work towards study of the strong spin-photon coupling regime. After a brief outline of the relevant theory, we will present the results of efforts to design and fabricate high finesse superconducting cavities as well as refinements of our equipment for measurements involving low numbers of photons.

4.3 Modelling the Spin Photon Interaction: The Jayne-Cummings Hamiltonian

To model the interaction between a spin and a photon we, at minimum, have to consider three things: (1) the energy of the spin, (2) the energy of the photon, and (3) the energy of their interaction. The Jayne-Cummings (JC) model includes contributions from each of these:

$$H = \frac{\hbar}{2}\omega_s\sigma_z + \hbar\omega_p a^\dagger a + \hbar g\left(a^\dagger\sigma^- + a\sigma^+\right) \tag{4.4}$$

where the first term combines the transition energy of the spin ω_s with the Pauli operator σ_z which accounts for the spin's orientation along an axis *z*. The second term includes the energy of a photon ω_s and the operator $a^\dagger a$ which counts the number of photon excitations present in the spin/cavity system. The final term describes exchange between the spin and photon as characterized by the rate g with terms denoting emission $a^\dagger\sigma^-$ by the spin into the cavity or absorption $a\sigma^+$ from the cavity to the spin.

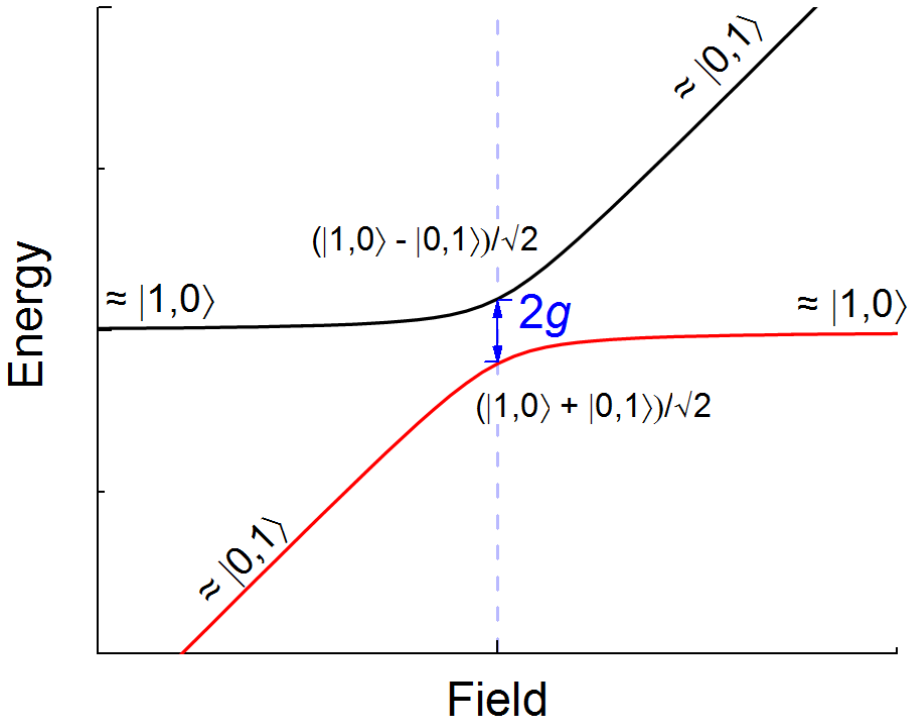

Figure 4.3 – Energy level diagram in the JC model at the anticrossing between coupled spin and cavity eigenstates. The magnitude of the splitting exactly on resonance is given by $2g$, which separates eigenstates comprised of symmetric/antisymmetric superpositions of the bare states.

This interaction term comes from a rotating wave approximation [21] which neglects high frequency counter-rotating terms in moving from the Schrodinger to the Interaction picture. For a single excitation shared between the spin/cavity, this Hamiltonian has the matrix form

$$H = \hbar \begin{bmatrix} \omega_p & g \\ g & \omega_s \end{bmatrix}. \tag{4.5}$$

In the absence of any coupling g, the eigenvectors of the system reduce to |1,0> and |0,1>, representing the excitation in the cavity and spin, respectively. Assuming a non-zero g, the two eigenvalues $E_{1,2}$ of the system are given by

$$\frac{E_{1,2}}{\hbar} = \frac{\omega_p}{2} + \frac{\omega_s}{2} \pm \sqrt{g^2 + \frac{1}{4}\left(\omega_p - \omega_s\right)^2}. \tag{4.6}$$

If we imagine a spin ½ in a magnetic field B, we can replace the spin transition energy ω_s by the Zeeman coupling $\mu_s B$ and calculate the system's dependence on a magnetic field about the resonance between the spin transition and photon energies. Figure 4.3 shows the branches formed by the eigenvalues $E_{1,2}$ of the two states. As the transition energy of the spin approachies that of the cavity, the states hybridize with an avoided crossing of magnitude $2g$ separating symmetric/anstisymmetric states exactly on resonance (as expected when the energy difference between the spin/photon vanishes in equation 4.6). As we will see in the next section, we can treat this interaction in a similar fashion to a system driven with applied microwaves as discussed above, with an interpretation that the driving stimulus is due to fluctuations of the vacuum itself, i.e. zero-energy virtual particle creation/annihilation.

4.3.1 Vacuum Rabi oscillations

In the JC model we outlined above, the only elements present in our system are spin, cavity, and an excitation shared between them. When we outlined our experiments investigating weak spin-photon coupling above, we described Rabi oscillations as coherent periodic exchange between a spin and a cavity as a function of the power of applied microwaves. Here, we apply no such driving field, and an intial state of an spin in its excited state and no photons in the cavity is an acceptable assumption.

The coupling factor g is an essential metric in understanding the evolution of the JC model, with fundamental units of energy (or frequency). It characterizes the rate of coherent vacuum Rabi oscillations, a phenomenon understood as an analog of the standard Rabi oscillations where the driving field comes from the cavity vacuum fluctuations B_0 instead of an applied microwave pulse. In the vacuum Rabi framework, the relationship between the spin/cavity exchange rate g and the spin parameters and vacuum field is given by

$$g = f_{Rabi} = \frac{2\, g_L \mu_B S B_0}{\hbar} \tag{4.7}$$

where g_L is the Lande factor. In order to observe coherent vacuum Rabi oscillations, the frequency f_{Rabi} must be greater than the decoherence rates of the system (i.e., there must be enough time for the system to complete at least one oscillation before it decays). If the cavity is characterized by a quality factor Q, the photon decay rate is given by

$$k_p = \omega_p / Q. \tag{4.8}$$

As discussed in section 4.1, there are a number of significant sources of decoherence for spins (SMMs in particular), all contributing towards the total decay rate k_S. In order to reach the strong-coupling regime where many coherent vacuum Rabi oscillations can be observed, the system must satisfy the bound

$$\frac{2\,g}{k_S + k_p} \gg 1. \tag{4.9}$$

The challenge then is to maximize the coupling g while minimizing the decoherence of the spin and photon. We have already outlined methods for reducing the decoherence of a spin within a SMM, and in the next section we will detail superconducting cavity devices which produce long photon lifetimes and concentrated magnetic field at the sample position, as well as additional techniques required for obtaining the necessary sensitivity when involving a small number of photons.

4.4 Techniques for probing strong coupling between spins and a low number of photons

The vehicle we have chosen is a refinement of the resonant cavity devices we have previously employed in studying SMM systems. Co-planar waveguide resonant cavities fabricated from superconducting films on substrates with high-dielectric constants have shown that quality factors above $Q = 10^6$ are possible [23-26] in planar geometries. A device with a quality factor near this range would lead to decoherence rates below that expected for a SMM under the optimal conditions attainable in our apparatus, with excitation lifetimes approaching than 100 μs.

4.4.1 Design Parameters of Nb/Sapphire Superconducting Resonators

Our plan was to fabricate devices from a 150 nm-thick Nb layer deposited on Al_2O_3 (Sapphire) of thickness h = 600 μm. In our blueprint for the devicce, the width of the center line is w = 16 μm and the separation between the center line and the ground plates is s = 7 μm. These parameters are calculated to obtain a device impedance of 50 Ohms, chosen to minimize microwave transmission losses due to impedance mismatch. Six different resonator lengths are included in our UV mask: l = 4, 8, 12, 20, 25 and 30 mm. The equation for the resonant frequency of the device is

$$f_0 = \frac{c}{2l\sqrt{\varepsilon_{eff}}} \tag{4.10}$$

where c is the speed of light and ε_{eff} = 5.70 (see below) is the geometry-dependent effective dielectric constant. The corresponding frequencies, in order of the longest resonator length to shortest, are f_0 = 15.7, 7.85, 5.23, 3.14, 2.51 and 2.1 GHz. In order to estimate other properties of the resonator, such as the impedance and quality factor, we need to first calculate the inductance L and capacitance C. We can derive these two qualities from their per-unit-length factors L_l and C_l with the equations

$$L_l = \frac{\mu_0}{4}\frac{K(k_0')}{K(k_0)} \tag{4.11}$$

$$C_l = 4\varepsilon_0\varepsilon_{eff}\frac{K(k_0)}{K(k_0')} \tag{4.12}$$

where K denotes the complete elliptic integral of the first kind with the arguments given by

$$k_0 = \frac{w}{w+2s} \tag{4.13}$$

$$k_0' = \sqrt{1-k_0^2} \tag{4.14}$$

with *w* and *s* being the width and ground separation gap of the central transmission line. The effective permittivity of the device can be calculated by using

$$\varepsilon_{eff} = \frac{1 + \varepsilon_{Saph} K^*}{K^*} \tag{4.15}$$

where ε_{Saph} = 10.4 (the average of the directional dielectric constants $\varepsilon_{\|c}$ = 11.5 and $\varepsilon_{\perp c}$ = 9.3 for this substrate), and K^* is given by

$$K^* = \frac{K(k_0)K(k_1')}{K(k_0')K(k_1)} \tag{4.16}$$

with the new arguments

$$k_1 = \frac{\tanh\left(\frac{\pi w}{4h}\right)}{\tanh\left(\frac{\pi(w+2s)}{4h}\right)} \tag{4.17}$$

$$k_1' = \sqrt{1 - k_1^2} \tag{4.18}$$

For our devices, we obtain ε_{eff} = 5.7, L_l = 3.96×10^{-7} H/m and C_l = 1.60×10^{-10} F/m. Note that in superconductors the total inductance results from a combination of the geometric (magnetic) inductance L_l^m and the kinetic inductance L_l^k associated with the motion of the Cooper pairs, i.e. $L_l = L_l^m + L_l^k$. For Nb below the transition temperature, the kinetic contribution is about two orders of magnitude lower than the geometrical, and therefore the total inductance calculated in equation (4.11) is a good approximation (see detailed calculation below). Schematically, the transmission line can be described as an infinite series of inductances and capacitances as shown in the figure below (distributed element representation):

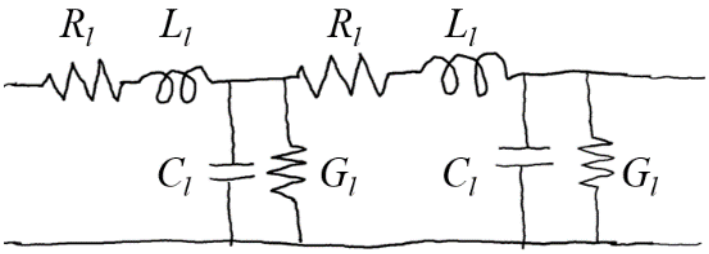

Figure 4.4 – Section of an infinite series representation of a CPW transmission line circuit.

When the losses are small, as in the case of superconducting lines ($R_l \approx 0$) with low dielectric loss ($G_l \approx 0$), the line impedance can be calculated according to:

$$Z = \sqrt{\frac{R_l + j\omega L_l}{G_l + j\omega C_l}} \approx \sqrt{\frac{L_l}{C_l}} \tag{4.19}$$

which in our case gives Z = 49.78 Ω, close to the 50 Ω impedance that we calculated with the freeware TX-LINE.

In a resonator, the transmission line is coupled through gaps to the feed lines of the device. In the distributed element representation (with assumed symmetrical couplings) the corresponding circuit is shown in the figure below, where the resonator is capacitively connected to the each of the feed lines with coupling capacitance C_k and load resistance R_L.

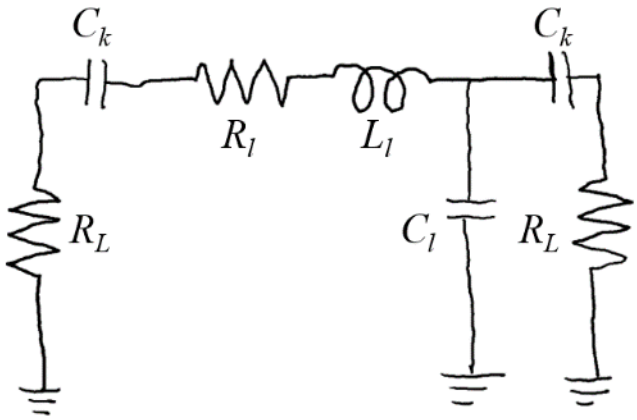

Figure 4.5 – Circuit diagram of the distributed element representation for a capacitively coupled resonator.

The impedance of this circuit is given by:

$$Z_{TL} = Z\frac{1 + j\tan(\beta l)\tanh(\alpha l)}{\tanh(\alpha l) + j\tan(\beta l)} \tag{4.20}$$

$$\approx \frac{Z}{\alpha l + j\pi(\omega - \omega_0)/\omega_n} \tag{4.21}$$

where α and β are attenuation and phase of the propagating wave, respectively. These can be calculated as the real and imaginary parts of the complex wave propagation coefficient, γ, respectively, which is given by

$$\gamma = \sqrt{(R_l + j\omega L_l)(G_l + j\omega C_l)} \tag{4.22}$$

For a given frequency, β describes the phase velocity, $v_{ph} = \omega/\beta$, which for a nearly lossless line reduces to $v_{ph} = 1/(L_l C_l)^{1/2}$. Correspondingly, the attenuation is described by the real part and approximates as

$$\alpha = \mathrm{Re}[\gamma] \approx R_l/Z + G_l Z \tag{4.23}$$

The approximation in equation (4.21) works well for small losses ($\alpha l << 1$) and when ω is close to $\omega_n = n\,\omega_0$ (n^{th}-harmonic frequency). Close to resonance, this circuit can be approximated by the lumped element parallel LRC oscillator shown in the figure below:

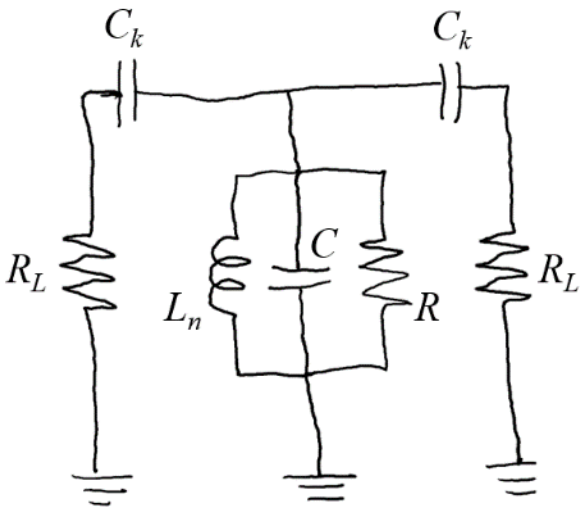

Figure 4.6 – Circuit diagram of the near-resonant lumped element LRC circuit.

which can be described with the following impedance

$$Z_{LRC} = \left(\frac{1}{j\omega L_n} + j\omega C + \frac{1}{R}\right)^{-1} \tag{4.24}$$

$$\approx \frac{R}{1 + 2jRC(\omega - \omega_n)} \tag{4.25}$$

where

$$L_n = \frac{2L_l l}{n^2\pi^2} \tag{4.26}$$

$$C = \frac{C_l l}{2} \tag{4.27}$$

$$R = \frac{Z}{\alpha l} \tag{4.28}$$

The approximation in equation (4.25) is valid if $\omega \approx \omega_n$. Using the values found before for $L_\ell = 3.96\times10^{-7}$ H/m and $C_\ell = 1.60\times10^{-10}$ F/m, we obtain $L = 6.43\times10^{-10}$ H/m and $C = 6.40\times10^{-13}$ F/m for the ground resonance ($n = 1$) of our 7.85 GHz ($l = 8$ mm) resonator.

To find the value of R that characterizes the equivalent parallel LRC resonance circuit, one needs to find α, and consequently both R_l and G_l. Note that at temperatures well below T_c, R_l and the resistive losses of the circuit will be negligible. In these conditions, the primary source of loss will be irradiative due to the finite conductance of the dielectric, G_l. The conductivity of our Sapphire substrates is $G_l < \sim 10^{-16}\ \Omega^{-1}\text{m}^{-1}$ (below 25 C). The resistance per unit length of the superconducting line results from the kinetic inertia of the Cooper pairs (kinetic inductance) and can be calculated according to the following expression

$$R_l = \frac{n_n}{n_s} L_K \omega^2 \tau_n g(w,s,t) \tag{4.29}$$

where $n_n/n_s = \exp(-1.76\ T_c/T)$ is the ratio between density of normal and superconducting quasiparticles according to BCS theory, L_K is the kinetic inductance, $\tau_n = 10^{-12}$ s is the scattering time of normal carriers and $g(w,s,t)$ is the geometrical factor associated with the CPW transmission line, which can be calculated according to [27]

$$g(w,s,t) = \frac{1}{2k_0^2 K(k_0)^2}\left[-\ln\left(\frac{t}{4w}\right) - \frac{w}{w+2s}\ln\left(\frac{t}{4(w+2s)}\right) + \frac{2(w+s)}{w+2s}\ln\left(\frac{s}{w+s}\right)\right] \tag{4.30}$$

For our resonators, $g(a,s,t) = 3.864$. The kinetic inductance can be found from the following expression:

$$L_K = \mu_0 \frac{\lambda_L^2}{wt} g(w,s,t) \tag{4.31}$$

where λ_L is the London penetration depth, which depends on the temperature according to $\lambda_L(T) = \lambda_L(0)\Theta(T)$ [27]. The temperature dependence is characteristic of each material, but in the BCS

limit, can be approximated by $\Theta(T) = (1-T/T_c)^2$ [26]. At $T = 0$, the London penetration depth (in nm) can be found by

$$\lambda(0) = 1.05 \times 10^7 \sqrt{\frac{\rho(T_c)}{T_c}} \tag{4.32}$$

Where $\rho(T_c)$ is the resistivity at T_c (ρ_{Nb} ~1.25×10^{-8} Ω m). For Nb, this gives $\lambda_L(0) = 38$ nm.

The quality factor associated to the attenuation of the line (resistive loss) is:

$$Q_{int} = \frac{\pi Z_0}{2\, R_l\, l} \tag{4.33}$$

which for $T < 1$ K will be $Q_{int} >> 10^9$. Consequently, the intrinsic quality factor associated to resistive /dielectric losses is then going to be limited by dielectric losses and can be calculated according to

$$Q_{int} = \omega_0 RC \tag{4.34}$$

which in our case is $Q_{int} \sim 8.2 \times 10^{15}$. Note the resulting resistance ($R \sim 2.5\times10^{17}$ Ω, from equation (4.28) of the equivalent parallel circuit (see figure above) is very large, making the current to oscillate lossless between L and C.

Electromagnetic irradiation may become a major source of energy loss in low-attenuation CPW resonators. A simple formula to obtain the limiting quality factor associated to irradiation losses is given by [28,29]:

$$Q_{irrad} = 3.5\left(\frac{l}{w+2s}\right)^2 \tag{4.35}$$

For our 8 mm long resonator, the resulting quality factor is $Q_{irrad} \sim 2.5 \times 10^5$. Irradiation losses can be drastically eliminated by placing the CPW resonator inside a cavity (e.g. metallic housing box) with no resonance modes in the vicinity of the resonance frequency of the resonator.

The load quality factor of the resonator is determined by the intrinsic resonator losses and the coupling losses:

$$\frac{1}{Q_L} = \frac{1}{Q_{int}} + \frac{1}{Q_{ext}} \tag{4.36}$$

The resonator line is capacitively coupled (C_k) to the reflection (input) and transmission (output) lines by symmetric coupling gaps (Asymmetric gaps can be used to work in transmission mode while keeping high *Q*s). In our design, two different kinds of coupling gaps have been designed: a) direct gaps, shown in the figure below on the left, and b) interdigital gaps (right).

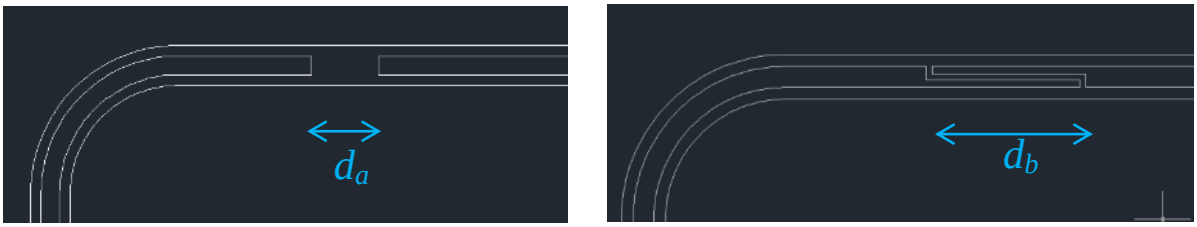

Figure 4.7 – Detail of the schematics showing the different styles of coupling gaps employed, with direct gaps shown in the left and interdigitated gaps on the right.

The separations between the lines for the direct gaps are d_a = 100, 50, 25, 14, 8 and 4 μm, while interdigital coupling gaps are formed by two 5μm-wide fingers, separated by 4 μm over a distance d_a = 100 and 50 μm. The gaps' dimensions are blindly chosen to obtain both under- and over-coupled resonators, attending to results by other authors in similar designs [23].

To understand the effect of the coupling on the quality factor of the resonator, it is better to replace the series connection of the coupling capacitance (C_k) and the load resistance (line impedance, R_L = 50Ω) by a Norton equivalent parallel connection of a resistor R^* and a capacitor C^*, as shown in the following figure:

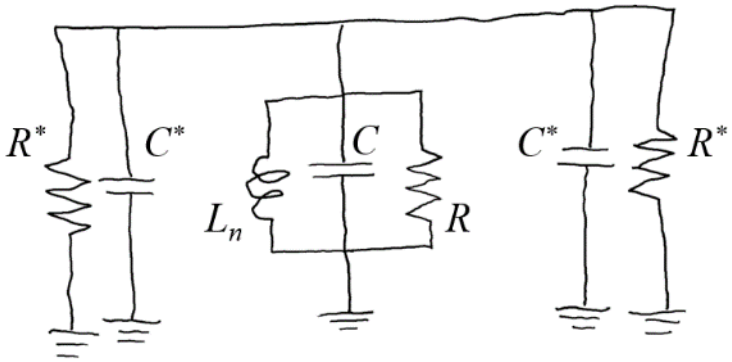

Figure 4.8 – Circuit diagram of a resonant cavity with Norton representation of a parallel capacitance and resistance in place of the load resistance and coupling capacitance shown in figure 4.6.

The equivalent parameters are given by

$$R^* = \frac{1 - \omega_n^2 C_k^2 R_L^2}{\omega_n^2 C_k^2 R_L^2} \tag{4.37}$$

$$C^* = \frac{C_k}{1 + \omega_n^2 C_k^2 R_L^2} \tag{4.38}$$

The small coupling capacitance transforms the line impedance into a large impedance $R^* = R_L/k$, with $k = \omega C_k R_L$ (<<1). The load quality factor for a symmetric resonator (combining R with $R^*/2$) is given by:

$$Q_L = \omega_n^* \frac{C + 2C^*}{1/R + 2/R^*} \approx \omega_n^* \frac{C}{1/R + 2/R^*} \tag{4.39}$$

with the resonance frequency shifted due to the parallel combination of C and C^*. (4.40)

$$\omega_n^* = \frac{1}{\sqrt{L_n(C + 2C^*)}} \tag{4.41}$$

For small coupling capacitances ($C>>C^*$) $\omega_n^* \approx \omega_n$, the internal and external contributions to the load quality factor can be separated as in equation (4.36). In this case, the external quality factor becomes:

$$Q_{ext} = \frac{\omega_n R^* C}{2} \tag{4.42}$$

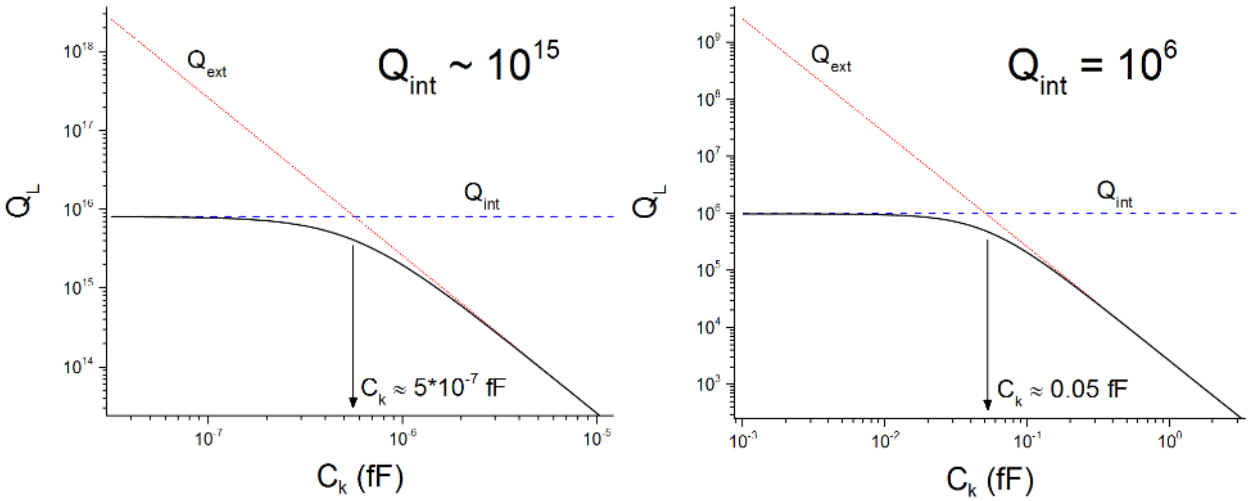

Figure 4.9 – Plots of the quality factor Q_L as a function of the coupling capacitance for a cavity with an internal quality factor $Q_{int} \sim 10^{15}$ (left) and $Q_{int} = 10^6$ (right) as generated from equation (4.42).

Figure 4.9 shows the behavior of Q_L, Q_{int}, and Q_{ext} as a function of C_k where the internal quality factor ($Q_{int} \sim 10^{15}$) is limited by dielectric losses (left plot), and for a lower internal quality factor ($Q_{int} \sim 10^6$, right plot) which may be more similar to what we find in real devices (including irradiative losses and higher resistive losses). The graphics above illustrate how difficult it can be to design the coupling gaps. Even if the gaps were straightforward to design and implement, the gap to critically couple the resonator to the input-output lines strongly depends on the internal quality factor of the resonator. Measuring Q_L for devices with the different designed gaps will allow us to determine which coupling gap places us in the proper regime, whether we want to be under-coupled, critically-coupled or over-coupled.

4.4.2 Device Fabrication and Characterization

As previously outlined, our devices were fabricated from 600 μm-thick sapphire wafers with a 150 nm layer of sputtered Nb on top. UV photolithography was used to create the device pattern in a polymer layer which then acted as an etching mask in a reactive ion etcher (RIE). The device dimensions were calculated to maximize the quality factor of the device in a 50 Ohm impedance configuration. Patterns

with different coupling gap sizes between the feed lines were included in the mask design in order to find an optimal gap separation. Appendix B contains a detailed recipe for SC resonator device fabrication.

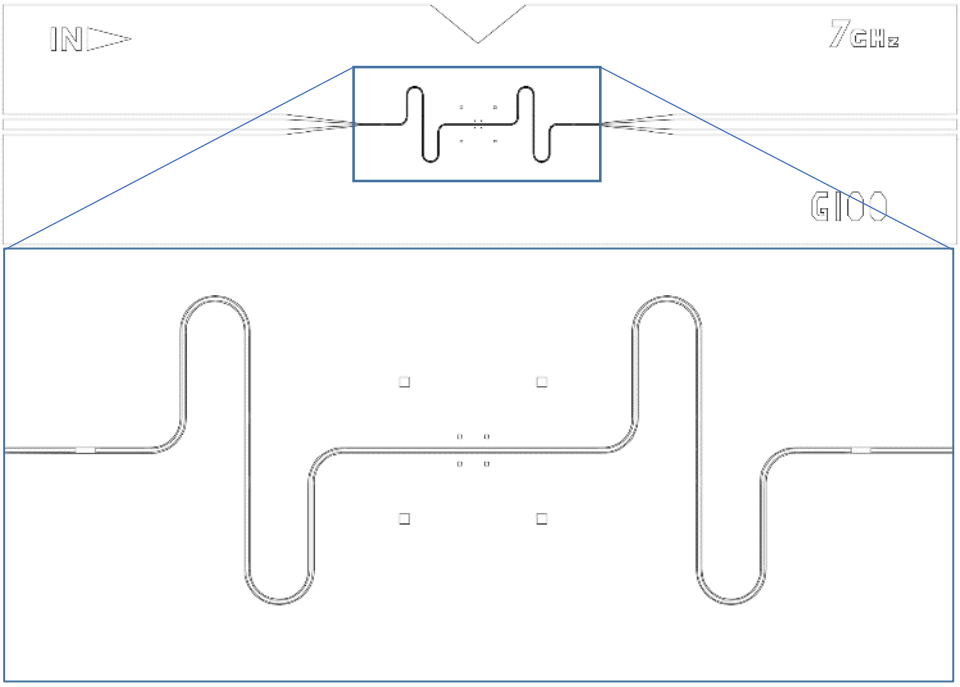

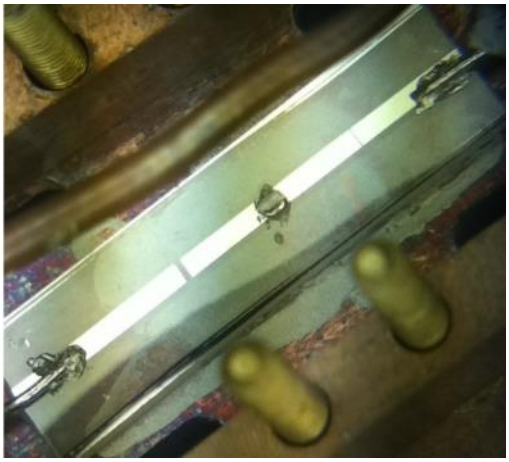

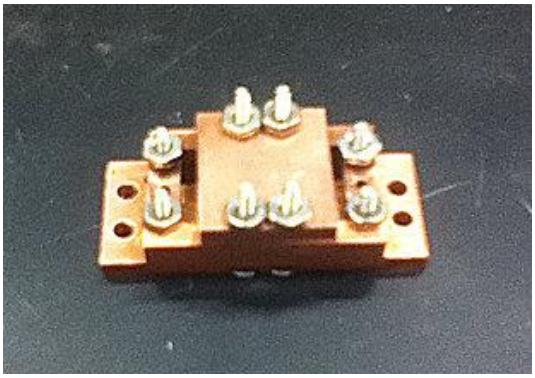

Figure 4.10 – (top) Autocad design of a 7 GHz Nb-on-Sapphire superconducting resonator. The meandering path allows for low frequency devices which fit within a smaller footprint. The long dimension of the entire pattern is 2 cm. (Bottom left) Photograph of a microstrip style Nb resonator with a sample. (Botttom right) The housing box used for mounting samples and measurements in our cryostat/dilution refrigerator. By an exclusively copper construction, the device/sample space within is free of any superconducting material that might lead to parasitic resonances.

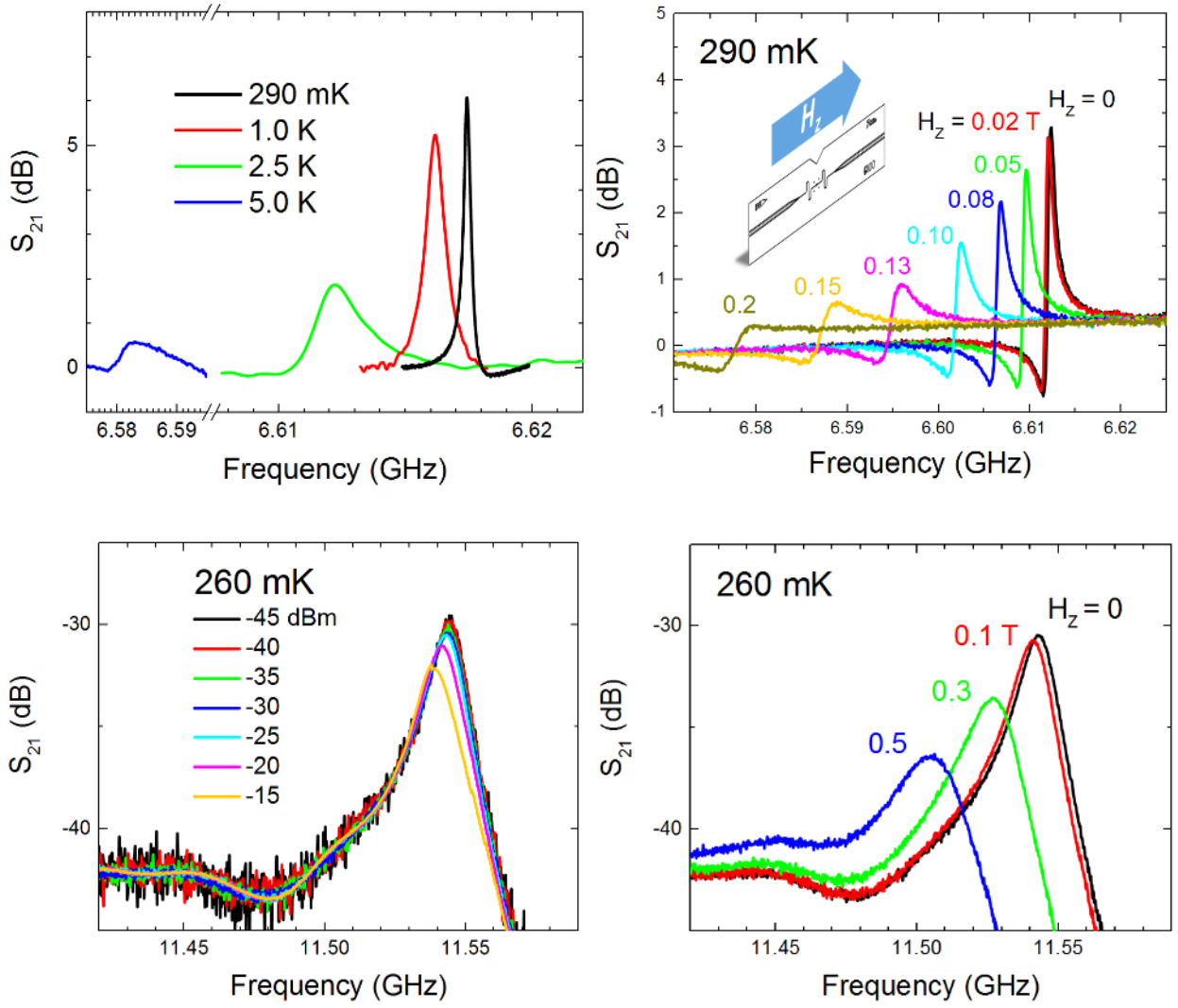

Figure 4.11 – Plots of various parameters of the superconducting resonators. The top-left panel shows the temperature dependence of a SC resonance feature from $Q \approx 25{,}000$ CPW resonator. The top-right panel shows the resonance of an identical device as a function of an in-plane magnetic field. The bottom-left panel shows the power dependence of a $Q \approx 800$ SC resonance feature from a microstrip style device. The bottom right panel shows the same resonance feature as a function of an in-plane applied magnetic field.

Figure 4.4 shows an AutoCAD design for one of our 7 GHZ CPW resonator designs. The symmetric design allows for transmission in either direction and suppresses standing wave resonances which may develop within the instrumentation. The same figure also includes photographs of a microstrip style resonator device and the Cu housing box used for our measurements. By fabricating the housing box from a non-superconducting material, we eliminate possible parasitic resonances which may appear in other commonly used materials, such as brass, which may contain concentrated Pb impurities.

Figure 4.5 shows the results of characterization performed on CPW (top two panels) and microstrip (bottom two panels) devices. At temperatures well below the superconducting transition for a thin Nb film (~ 7 K), we observed a sharp resonance peak with a quality factor $Q \approx 25{,}000$, which is equivalent to an estimated photon lifetime $\tau = Q / \pi f_0 \approx 1\ \mu$s, where f_0 is the resonance frequency. The microstrip resonator was found to have a quality factor Q of approximately 800.

If we intend to use these devices with low photon occupation numbers, we will need significant amplification in order to bring the signal amplitude within range of a measurement sensitivity. Moreover, the estimated power of a signal photon is (in dBm) given by

$$P_{dBm} = 10 * \text{Log}[1000 * 2\pi h f_0 / Q] \tag{4.43}$$

which is equal to nearly -140 dBm for our highest quality factor device. Such a small signal requires amplification at the low temperature stage in order to prevent it being drown out by thermal noise in the coaxial lines that run from low to ambient temperatures. A cryogenic amplifier placed immediately at the output from the cavity would serve such a function, and is our proposed solution to this challenge. Ideally, this would provide sufficient gain that room temperature amplifiers could bring the signal within range of our measurement apparatus. Cryogenic circulators will also be employed on either side of the cavity in order to provide further isolation to the cavity.

In order to further increase the coupling of the photon to the spins within the sample, which for a single spin and photon driven by the vacuum fluctuations is on the order off 100 Hz, we look to exploit collective coupling effects by which an excitation with wavelength longer than the dimensions of the spin ensemble can coupling to all the spins simultaneously and increase the coupling factor by the square root of the number of spins N [30,31]. For a typical SMM sample, $N \sim 10^{12} - 10^{16}$, meaning enhanced couplings into the GHz range. Such a coupling strength is easily observed as a frequency splitting and is much faster than the coherence times of our proposed systems, meaning vacuum Rabi oscillations should be observable.

In summary, both of these projects present significant challenges. Successful measurement in the weak coupling regime depends on the coherence time and coupling to a SMM sample at temperatures and signal amplitudes near the limit of our current instrumentation. Measurement of the effects of the strong coupling regime will require implementation of delicate equipment to drastically increase the sensitivity of our measurement apparatus. But a positive result in either case would represent study of the kind of interaction that is essential to progress for a broad range of new physics.

References

[1] W. Wernsdorfer, N. Aliaga-Alcalde, D. N. Hendrickson, G. Christou, Exchange-Biased Quantum Tunnelling in a Supramolecular Dimer of Single-Molecule Magnets, Nature 416, 406 (2002)

[2] S. Hill, R. S. Edwards, N. Aliaga-Alcalde, and G. Christou, Quantum Coherence in an Exchange-Coupled Dimer of Single-Molecule Magnets, Science 302, 1015 (2003).

[3] E. del Barco, A. D. Kent, E. C. Yang, and D. N. Hendrickson, Quantum Superposition of High-Spin States in Single Molecule Magnet Ni_4, Phys. Rev. Lett. 93, 157202 (2004).

[4] G. de Loubens, D. A. Garanin, C. C. Beedle, D. N. Hendrickson and A. D. Kent, Magnetization relaxation in the single-molecule magnet Ni4 under continuous microwave irradiation, Europhys. Lett. 83, 37006 (2008).

[5] H. M. Quddusi, J. Liu, S. Singh, K. J. Heroux, E. del Barco, S. Hill, and D. N. Hendrickson, Asymmetric Berry-Phase Interference Patterns in a Single-Molecule Magnet, Phys. Rev. Lett. 106, 227201 (2011).

[6] M. N. Leuenberger and D. Loss, Quantum Computing in Molecular Magnets, Nature 410, 789 (2001);

[7] J. Tejada, E. M. Chudnovsky, E. del Barco, and J. M. Hernandez, Magnetic Qubits as Hardware for Quantum Computers, Nanotechnology 12, 181 (2001);

[8] P. C. E. Stamp and A. Gaita-Ariño, Spin-based quantum computers made by chemistry: hows and whys, J. Mater. Chem. 19, 1718 (2009);

[9] M. Affronte, Molecular nanomagnets for information technologies, J. Mater. Chem. 19, 1731 (2009).

[10] J. Lehmann, A. Gaita-Ariño, E. Coronado, and D. Loss, Quantum computing with molecular spin systems, J. Mater. Chem. 19, 1672 (2009).

[11] M Affronte, F Troiani, A Ghirri, A Candini, M Evangelisti, V Corradini, S Carretta, P Santini, G Amoretti, F Tuna, G Timco and R E P Winpenny, J. Phys. D; Appl. Phys. 40, 2999 (2007).

[12] N. V. Prokof'ev and P. C. E. Stamp, Macroscopic quantum coherence in molecular magnets, Phys. Rev. Lett. 80, 5794-5797 (1998).

[13] M. Bal, J. R. Friedman, Y. Suzuki, E. M. Rumberger, D. N. Hendrickson, N. Avraham, Y. Myasoedov, H. Shtrikman, E. Zeldov, Non-equilibrium magnetization dynamics in the Fe_8 single-molecule magnet induced by high-intensity microwave radiation, Europhys. Lett. 71, 110 (2005).

[14] S. Takahashi, I. S. Tupitsyn, J. van Tol, C. C. Beedle, D. N. Hendrickson, and P. C. E. Stamp, Decoherence in crystals of quantum molecular magnets, Nature 476, 76–79 (2011)

[15] Spin coherence in a Mn3 single-molecule magnet C. Abeywardana, A. M. Mowson, G. Christou, and S. Takahashi Appl. Phys. Lett. 108, 042401 (2016)

[16] A. Ardavan, O. Rival, J. J. L. Morton, S. J. Blundell, A. M. Tyryshkin, G. A. Timco and R. E. P. Winpenny, Will spin-relaxation times in molecular magnets permit quantum information processing? Phys. Rev. Lett. 98, 057201 (2007).

[17] S. Bertaina, S. Gambarelli, T. Mitra, B. Tsukerblat, A. Muller and B. Barbara, Quantum Oscillations in a Molecular Magnet, Nature 453, 203-206 (2008).

[18] C. Schlegel, J. van Slageren, M. Manoli, E.K. Brechin and M. Dressel, Direct Observation of Quantum Coherence in Single-Molecule Magnets, Phys. Rev. Lett. 101, 147203 (2008).

[19] J.J. Henderson, C. M. Ramsey, E. del Barco, S. Datta, S. Hill, T. C. Stamatatos and G. Christou. Control of the inhomogeneity degree by magnetic dilution in crystals of antiferromagnetic molecular rings. Phys. Rev. B 78, 214413 (2008).

[20] F. Luis, E. Coronado, M. J. Martínez-Pérez, S. Cardona-Serra, O. Montero, C. Martí-Gastaldo, J. M. Clemente-Juan, J. Sesé, D. Drung, and T. Schurig. Spin-lattice relaxation via quantum tunneling in an Er3+- polyoxometalate molecular magnet. Phys. Rev. B 82, R 060403 (2010).

[21] Wu, Ying; Yang, Xiaoxue (2007). "Strong-Coupling Theory of Periodically Driven Two-Level Systems". Physical Review Letters 98

[22] H. Quddusi, Role of internal degrees of freedom in the quantum tunneling of the magnetization in single-molecule magnets, PhD Thesis, University of Central Florida (2012)

[23] M. Goppl, A. Fragner, M. Baur, R. Bieanchetti, S. Filipp, J. M. Fink, P. J. Leek, G. Puebla, L. Steffen and A. Wallraff. Coplanar waveguide resonators for circuit quantum electrodynamics. J. Appl. Phys. 104, 113904 (2008).

[24] L. Frunzio, A. Wallraff, D. Schuster, J. Majer and R. Schoelkopf. Fabrication and Characterization of Superconducting Circuit QED Devices for Quantum Computation. IEEE Trans. Appl. Supercond. 15, 860 (2005).

[25] A. Wallraff, D. I. Schuster, A. Blais, L. Frunzio, R.- S. Huang, J. Majer, S. Kumar, S. M. Girvin and R. J. Schoelkopf. Strong coupling of a single photon to a superconducting qubit using circuit quantum electrodynamics, Nature 431, 162 (2004)

[26] D. I. Schuster. PhD Thesis, Yale University (2007).

[27] K. Yoshida et al., IEEE Trans. Appl. Supercond. 5, 1979 (1995).

[28] B. Mazin, et al. In Proc. SPIE Vol. 4849, (2002).

[29] B. Mazin, PhD thesis, California Institute of Technology, (2004).

[30] M. Tavis and F. W. Cummings, Exact Solution for an N-Molecule—Radiation-Field Hamiltonian. Phys. Rev. 170, 379-384 (1968).

[31] A.W. Eddins, C. C. Beedle, D. N. Hendrickson, and Jonathan R. Friedman, Collective Coupling of a Macroscopic Number of Single-Molecule Magnets with a Microwave Cavity Mode, Phys. Rev. Lett. 112, 120501 (2014)

CHAPTER 5: CONCLUSIONS

This thesis has attempted to outline the theory, implementation, and interpretation behind the study of complex yet fundamental spins systems. This chapter serves as a recap of our work, aiming to tie together the inferences that can be drawn within a common theme spin interaction. Specifically, we are interested in what may bear on spin anisotropy and coherent time evolution, aspects which lie at the heart of further advances across a range of disciplines. Tracing the history of research into single molecule magnets winds through initial rapid advances of the underlying theories (which still serve a large part of the work being done on these systems today, as illustrated by the success of spin Hamiltonian modelling) and continues through progress detailing the specifics of the quantum tunneling process and of the increasing capability of chemical synthesis. Both the Mn_3 and Mn_{12}-MeOH compounds we studied represent refined systems, designed with the challenges of studying SMMs in mind, and the results we have extracted rest firmly on many layered iterations of prior research stretching back to the first hysteresis showing QTM steps.

Our analysis of the resonant tunnel splitting shows the strong sensitivity of tunneling phenomenon to even small changes of the anisotropy parameters in the corresponding spin Hamiltonian. The inferred correspondence between the chemical arrangement and the structure of the anisotropy speaks to the broader campaign within the field that continues to enumerate a range of different SMM systems, with recent work by Shiddiq et al. [1] showing the potential to produce systems insulated from decoherence. The results of research into such “atomic clock” or “sweet spot” transitions imply that an engineered zero-field splitting could extend coherent behavior to higher temperatures and longer timescales. Conceivably, an SMM system could exhibit dependence on an applied transverse field which could produce an insensitivity to an applied field. Indeed, as shown in Fig. 1.8, the Mn_3 system we studied is expected to produce an extremum in the ground state splitting of the $k = 0$ resonance for an applied transverse field of

$\approx$ 2.7 T, although the small transition energy $\approx$ 1 mK and sensitivity to an infinitesimal rotation of the transverse field (i.e. stemming from a local dipolar fluctuation) likely precludes the usefulness of this particular configuration.

Work by Foss-Feig and Friedman [2] also directly points to the impact that small distortions to the molecular anisotropy can have in tuning the conditions for tunnel splitting minima due to Berry Phase interference effects. Although the QTM features we examined in Mn_{12}-MeOH show a small dependence on pressure ($\lesssim$ 10% change in the cumulative tunneling transition rate for 1 kBar of pressure), our simulations imply that significant differences can be expected between the responses of individual transitions (within the same resonance k) due to the change in a given parameter. Presumably, the effect on the tunneling rate will be strongest when the distortion represents either a) the introduction of a term which enables an otherwise suppressed transition or b) a change to the coefficient of an operator that is dominant mechanism for mixing two states with only one application of that operator (i.e. a change to B^x_x when $\Delta S = x$, in a system where O^x_x is the sole transverse anisotropy operator). Also, applying such a distortion at a transition in conditions nearby a BPI minimum may cast the effects on the tunneling rates in more stark relief.

The pulsed stimulus experiments we have proposed and developed look probe the inner workings of intrinsic anisotropy by exploring transitions influenced both by internal bias and an applied field. The Zeeman splittings generated by a transverse field applied to our Mn_3 system (see Fig. 4.1) illustrate a system transitions from a quantization axis dominated by the native molecular energy landscape (the ZFS) to one defined by an external field. Our measurements have confirmed strong EPR absorption from the system near X band frequencies, with the peak positions spanning the range of field in which both the intrinsic anisotropy and applied field are significant actors. Classically, the spin echo phenomenon is interpreted as the re-convergence of spins precessing about an applied field axis, which begs the question as to what time dependence a spin will display when acting under two different but significant potentials.

By exploring coherent phenomenon in a system in which we can tune the balance between these potentials as a function of frequency, we aim to thoroughly determine the extent to which conditions in the "neighborhood" about the resonance condition affect coherent evolution of these systems. Our goal to couple low numbers of photons to spins and coherent ensembles would add further dimension to this understanding, with the inclusion of a cavity into the coherent system.

The research we have outlined above shows the continued promise that spins systems (SMMs in particular) hold in the development of accessible two-level systems. As realizations of intrinsic anisotropy with macroscopic quantum phenomenon, these compounds continue to provide a window into the progress of many intersecting sciences, while the rapidly approaching horizon of atomic scale devices drives the continual need for further advancement into the potential building blocks of the future of technology. Regardless of the obvious connection to the future development of computers, I believe that the fundamental behaviors responsible for the data described here coincides with basic human fascination, providing its own reason for study, and exists within a chain of learning that begins with essential intuition and extends throughout time and the universe.

References

[1] M. Shiddiq, D. Komijani, Y. Duan, A. Gaita-Ariño, E. Coronado and S. Hill, Nature **531**, 348 – 351(2016)

[2] M. S. Foss-Feig and J. R. Friedman, EPL, **86**, 27002 (2009)

APPENDIX A: PROCEDURES USED IN EMPLOYING THE "REMAINDER METHOD"

Due to the peculiarities of every resonance, different implementations of the "remainder method" (detailed in Chapter 2) for indirect measurement of resonance probabilities in the presence of a large transverse field had to be used for different resonances. Below we provide a list with the details.

1. Measurement of $P_{k=0}$ vs. ϕ at resonance $k = 0$

   Here the longitudinal field was swept to negative saturation, then to a small negative field just before the resonance, at which point a transverse field of magnitude 1.05 T was applied and the longitudinal field swept through the resonance at a rate of 0.04 T/m. The sweep was then reversed such that the resonance was traversed again, which was performed in order to amplify the relatively small measured probability of the resonance. Once this second pass was completed, the transverse field was turned off, and the field swept back to negative saturation while the remainder was recorded. This was repeated for different angular orientations of the transverse field vector, forming a complete rotation in 5 degree increments.

2. Measurement of the compensating field at resonance $k = 0$

   To measure the shift in the longitudinal field position of the k=0 resonance (i.e. the compensating field), a variation of the method described above had to be employed. As mentioned in the main text, these measurements were performed at 1.57 K in order to obtain QTM relaxation through the third excited tunnel splitting in this resonance. For initializing the measurement, a large negative longitudinal field was applied in the absence of a transverse field and then swept back to a value close to but far enough from the resonance to avoid relaxation, Then both the transverse and the longitudinal fields were swept at rates of 0.05 and 0.5 T/min, respectively, to the following values: 1.2 T (transverse field) and ~1000 G before the center of the resonance (longitudinal field). The resonance width is ~2000 G for HT = 1.2 T, and so QTM relaxation occurs during the process. Immediately after reaching those conditions, both fields were swept back (at the same rates as before) to the original point, after which the longitudinal field was swept in the absence of a

transverse field to measure the remainder. The process was repeated at different angles of application of the transverse field within the xy-plane from $\phi = 0$ to $\phi = 360^{o}$. Note that during the time that both fields are swept into the resonance, the tunneling conditions vary since the transverse field (a strong modulator of the tunnel splitting) varies continuously from zero to 1.2 T. However, given the fast relaxation at this temperature, a constant transverse field of 1.2 T could not be employed for this measurement. As we show below, the exponential dependence of the tunnel splitting on the transverse field implies the average tunneling rate is dominated by the largest values of the transverse field.

From these measurements we obtained a three-fold angular modulation of the tunnel probability due to the shift of the resonance caused by the alternating compensating field, as explained in the main text. In other words, the probability is higher when the final longitudinal field is closer to the resonance, and vice versa. Measurements following the same protocol but sweeping the longitudinal field to different points relative to the resonance allowed the conversion of the probability into a longitudinal field value (i.e. the compensating field data depicted in Fig. 2c).

For the fitting of the observed modulation of the compensating field (continuous line in Fig. 2c), values were extracted for different transverse fields (0.7-1.2 T) from diagonalization of Eqn. (2) with the parameters given in the main text. Note that the value of the compensating field grows with the transverse field. The different values were correspondingly weighted according to the probability calculated from the Landau-Zener formula in order to take into account the varying transverse field during the measuring process. As mentioned above, the MQT in this process is dominated by the largest transverse field values, with negligible effects for values below 0.7 T. The results are in excellent agreement with the observations.

3. Measurement of $P_{k=0}$ vs. ϕ at resonance $k = 1$

Here the longitudinal field was swept to (negative for k = +1, positive for k = -1) saturation, then to a value a small distance before the resonance, at which point a transverse field of magnitude 0.65 T was applied and the longitudinal field swept through the resonance at a rate of 0.1 T/m. Once this was completed, the transverse field was turned off and the field swept to (positive for k = +1, negative for k = -1) saturation while the remainder was recorded. This was repeated for different angular orientations of the transverse field vector, forming a complete rotation in 5 degree increments.

4. Measurement of $P_{k=0}$ vs. ϕ at resonance k = 2

   The same exact procedure that for k=1, using a transverse field of 0.5 T and sweeping the longitudinal field through the resonance at 0.1 T/min.

5. Measurement of $P_{k=0}$ vs. ϕ at resonance k = 3

   Here the longitudinal field was swept to (negative for k = +3, positive for k = -3) saturation, then to a value a small distance before the $k = \pm 2$ resonance, at which point a transverse field of magnitude 0.4 T was applied at an angle of 35 degrees and the longitudinal field swept through that resonance at a rate of 0.075 T/m. This relaxed roughly 50% of the spins, preventing avalanching of the k = 3 resonance that would otherwise occur. Once this was completed, the transverse field was turned off and the field swept to a value a small distance before the k = 3 resonance, at which point a transverse field of magnitude 0.35 T was applied and the longitudinal field swept through the resonance at a rate of 0.05 T/m. Once this was completed, the transverse field was turned off and the field swept to (positive for k = +3, negative for k = -3) saturation while the remainder was recorded. This was repeated for different angular orientations of the transverse field vector, forming a complete rotation in 5 degree increments.

6. Measurement of $P_{k=0}$ vs. H_T at resonance k = 0

This measurement was identical to that described in *Step 1*, except that the angle was held fixed at 32.6 degrees (direction of one of the minima in Fig. 2a) and the magnitude of the transverse vector applied was increased in 0.05 T increments from -1.19 to 1.19 T.

7. Measurement of $P_{k=0}$ vs. H_T at resonance $k = 1$

   This measurement was identical to that described in *Step 3*, except that the angle was held fixed at 107 degrees (direction of one of the minima in Fig. 3a) and the magnitude of the transverse vector applied was increased in 0.05 T increments from -1.15 to 1.15 T.

8. Measurement of $P_{k=0}$ vs. H_T at resonance $k = 2$

   This measurement was identical to that described in *Step 4*, except that the angle was held fixed at 107 degrees and the magnitude of the transverse vector applied was increased in 0.05 T increments from -1.15 to 1.15 T.

9. Measurement of $P_{k=0}$ vs. H_T at resonance $k = 3$

   This measurement was identical to that described in *Step 5*, except that the angle was held fixed at 107 degrees and the magnitude of the transverse vector applied was increased in 0.05 T increments from -1 to 1 T.

APPENDIX B: RECIPE FOR FABRICATION OF NIOBIUM/SAPPHIRE RESONATORS

Resonators were made according to the following recipe

To prepare the wafer for UV mask aligning:

1. Clean the Nb-coated wafer with IPA and DI water, being careful to blow/wipe dry such that there are no solvent/water residues
2. Position the wafer on the spin coater and use a Teflon dropper to place a small amount of Shipley S1813 polymer onto the wafer such that the liquid forms a regular, distributed meniscus free of bubbles.
3. Close the spin-coater cover and use the spin coating program detailed below.
4. Once the program is complete, carefully remove the wafer and place it onto a 90° C heating stage for 3 minutes.
5. Remove the wafer from the heating stage and allow to cool for a few seconds.

At this point the wafer is ready to be set in the mask aligner for pattern exposure. The mask aligner model is a OAI Series 200. The steps for exposure are as follows:

1. Place the wafer on the vacuum stage and turn on the vacuum so that the wafer is held fixed.
2. Set and align the mask so that the desired pattern(s) overlay the wafer area.
3. Clamp the mask holder in place and raise the wafer stage until it contacts the bottom of the mask.
4. For an intensity of 8 mW/cm^2, 8 seconds of exposure time is sufficient to expose the polymer.
5. Once the exposure process is complete, carefully remove the wafer from the mask aligner

At this point the wafer is ready for liftoff development

1. Place the exposed wafer into CD-26 Developer for 45 seconds.
2. Once the time has elapsed, carefully move the wafer to a dish of DI water and gently rinse the wafer

3. Remove the wafer from the DI water and dry, being careful not to leave any residue.

The wafer is now ready for etching. The model of the etcher was a SAMCO RIE-1C. The steps for etching the pattern are as follows:

1. The flow rates for the gases should be 5.0 SCCM of CF4 and 0.8-1.0 SCCM of O2. The power of the etching plasma is 50 W. The pressure in the RIE chamber should be 53.0 mTorr.
2. Etch the wafer for 4 minutes.
3. Once the etching is complete, examine the pattern. It is likely that some polymer still remains, so the sample may need to be placed in CD-26 for enough time to remove it.